Alma Mater Studiorum – Università di Bologna

School of Science
Department of Physics and Astronomy
Master Degree Programme in Astrophysics and Cosmology

Using JWST to Investigate Dust Energy Balance in Galaxies at Cosmic Noon

Graduation Thesis

Presented by:
Benjamin P. Collins

Supervisor:
Chiar.mo Prof. Sirio Belli

Co-supervisor:
Amir H. Khoram

Academic year 2024-2025
Graduation date III

Abstract

The launch of the James Webb Space Telescope (JWST) has opened a new window onto the high-redshift Universe, enabling detailed studies of ionised gas and dust emission in galaxies. In this thesis, I perform photometry with the Mid-Infrared Instrument (MIRI) for galaxies in the COSMOS field, focusing on the Blue Jay survey ($1.7 < z < 3.5$) to investigate the dust energy balance assumption when fitting spectroscopic and photometric data to infer the physical properties of galaxies.

I present a self-consistent photometric workflow developed for this thesis, producing astrometrically aligned cutouts and RGB composite images, performing aperture photometry across multiple filters (F770W, F1000W, F1800W, and F2100W), resulting in a comprehensive photometric catalogue. For my analysis, I use publicly available JWST imaging products from the PRIMER, COSMOS-Web, and COSMOS-3D surveys. Special care was given to mitigate spurious noise gradients, detector artefacts, and bad pixels by implementing a robust background subtraction and source masking routine. I validate my measurements by comparing the F770W photometry to the COSMOS2025 catalogue, which does not include measurements in the other MIRI bands used in this work. Furthermore, the entire photometric pipeline is implemented in a custom-made Python package called `miri_utils` and made publicly available.

To test dust energy balance, we compare the measured MIRI photometry to the values predicted by existing best-fit model spectra, which were obtained with the Prospector code using HST and NIRCam photometry and NIRSpec spectroscopy from the Blue Jay survey, and do not include MIRI data. Energy balance assumes that all energy absorbed by dust in the UV–optical regime is re-emitted in the infrared, and is widely adopted in modern stellar population inference codes. While the fits broadly reproduce infrared fluxes, they systematically overpredict dust emission, particularly at longer wavelengths. Fluxes in F770W and F1000W are typically overestimated by $\lesssim 15\%$, whereas those in F1800W and F2100W exceed observations by factors of two to three. The same trend is observed with increasing dust attenuation A_V, suggesting that the systematic offset between the model and observations most likely originates from the assumption of dust energy balance, instead of incorrect template spectra.

This work establishes a reproducible framework for JWST/MIRI studies, demonstrating the opportunities and challenges of modelling panchromatic SEDs of galaxies at cosmic noon. It provides a critical evaluation of dust energy balance and its capability of extrapolating dust emission when infrared observations or strong priors are unavailable, highlighting the need for further studies to constrain the infrared SEDs of high-redshift galaxies.

Acknowledgements

First and foremost, I would like to express my sincere gratitude to my supervisor, Prof. Sirio Belli, for the opportunity to work on such a challenging and exciting project. His constant availability for discussion and his insightful guidance encouraged me to find my own solutions to complex problems, while he placed each aspect of my work within a broader scientific context that helped me connect ideas that at first seemed distant. I am deeply grateful to him and my co-supervisor, Amir H. Khoram, for their encouragement and mentorship throughout the course of this project, offering guidance and support that extended beyond the scope of this thesis. Lastly, I would like to thank everyone in the Red Cardinal team. Working on this project has been an immensely rewarding experience and has provided me with the tools and confidence to take the next steps towards a professional career in astrophysics research.

I want to dedicate a part of this work to my secondary school teacher, Mag. Wilfried Hartmann, for years of invaluable preparation in mathematics and physics, and perhaps most importantly, for fostering my early passion for astronomy. Not everyone is fortunate enough to have someone who sparks their fascination for science at such a formative stage - I am glad to count myself among the lucky ones.

I also want to thank my mother for her constant support and encouragement throughout my academic journey. She has been a true source of inspiration and a role model for me, and I would not be where I am right now without her. I am also grateful to my brothers, whose stimulating conversations, companionship, and frequent visits always brought a comforting touch of home to Bologna when it was needed.

I am equally grateful to my colleagues and friends whom I have had the pleasure of meeting during my time as a student at the University of Bologna. Whether in the classroom or outside, they always provided support, inspiration, and laughter along the way. Their companionship made the challenges faced in both my academic and personal life far more manageable and successes all the more rewarding, and my experience of studying abroad would not have been the same without them.

Finally, I would like to acknowledge everyone who, in ways big or small, contributed to the completion of this thesis.

In writing this dissertation, generative artificial intelligence tools were employed for writing support, debugging tasks, and data visualisation. The models used were ChatGPT (version 4.5 released in February 2025 and subsequent updates) and Claude (version 4 released in May 2025 and subsequent updates). The use of these tools has deepened my understanding for both their potential and their limitations, highlighting the importance of maintaining critical thinking when using AI in scientific research. More details about their use are provided in Appendix C.

Contents

Chapter 1

Introduction

1.1 Properties of Galaxies at Cosmic Noon

Galaxies are complex systems composed of tens of billions of stars, which undergo significant evolution throughout their lifetime. In particular, as astronomers began tracing the assembly of galaxies into the past, it was found that galaxies undergo a phase of rapid evolution between $1 < z < 3$, during a period now commonly referred to as *cosmic noon*, with about half of all stellar mass formed by $z = 1$ (e.g., Bundy et al., 2005; Mortlock et al., 2011). This turbulent phase of the universe is marked not only by the rapid build-up of stellar mass, but also by the peak of the cosmic star-formation rate density at $z \sim 2.5$, accompanied by a remarkable diversity in the morphology and star-formation histories of individual galaxies (Madau & Dickinson, 2014; Shapley, 2011). Figure 1.1 shows the evolution of the integrated star-formation rate density of the universe with respect to cosmic time, which is discussed in great detail in Madau and Dickinson (2014).

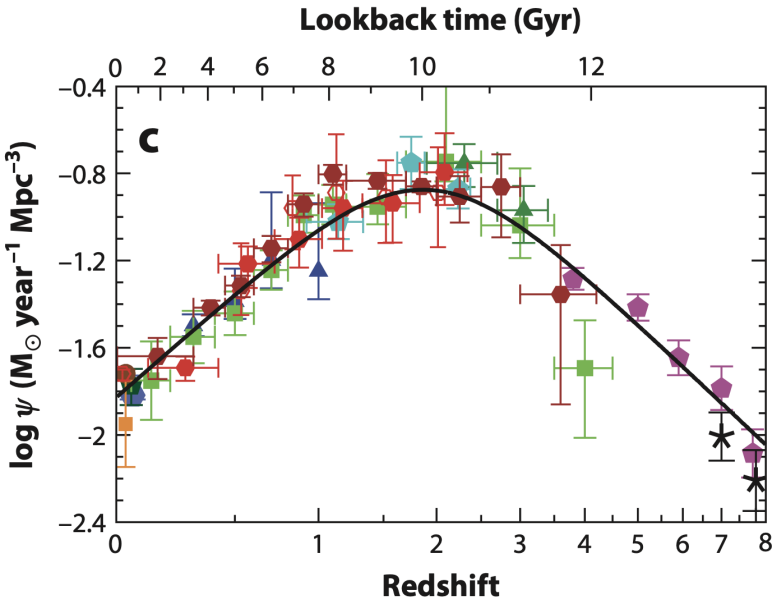

Figure 1.1: The star formation rate density of the universe across cosmic time. Image taken from Madau and Dickinson (2014).

Historically, galaxies were classified by Hubble in 1926 based on their optical appearance on photometric plates, a classification known as the Hubble sequence (Hubble, 1927). This classification divides galaxies into two main categories: Early-type galaxies (ETGs) - including ellipticals (E), lenticulars (S0) - and late-type galaxies (LTGs) - containing spirals and irregulars. Along the sequence, galaxies are arranged from bulge-dominated ellipticals to systems with progressively larger disc components (De Vaucouleurs, 1959). A later refinement introduced a bifurcation that distinguishes barred (SB) from unbarred spirals and gave the sequence its alternative name "tuning fork diagram". A small fraction of massive galaxies in the local universe - fewer than 10% - display irregular or peculiar morphologies that do not fit neatly within this framework (Delgado-Serrano et al., 2010). Hubble's galaxy classification scheme is shown in Figure 1.2.

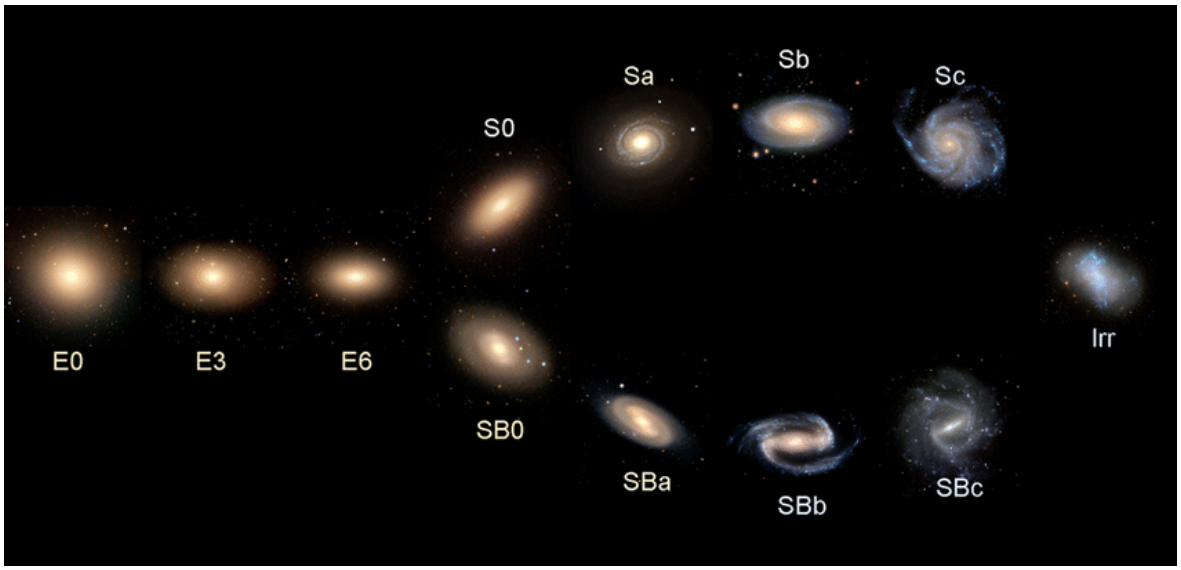

Figure 1.2: The Hubble sequence, often referred to as the Hubble tuning fork diagram. Image taken from Cui et al. (2014).

The turbulent environment of galaxies in the early universe also manifests itself in terms of galaxy morphology: While present-day massive galaxies typically appear as regular, dynamically relaxed structures, the high-redshift universe appears to be increasingly dominated by galaxies with peculiar morphologies, reflecting the active assembly of galaxies during this epoch. This was first investigated by Van Den Bergh et al. (1996) using data from the Hubble Space Telescope (HST), showing that the Hubble sequence was certainly not fully established at $z > 1$. Subsequent studies found almost no trace of the Hubble sequence at $z > 2$, reporting that the number density of spirals and ellipticals surpasses that of peculiar galaxies only at $z \sim 1.5$ (Conselice et al., 2005; Ravindranath et al., 2004). Indeed, when observed with HST, many of these early systems exhibit irregular, clumpy morphologies, with massive star-forming regions dispersed throughout their discs. Figure 1.3 provides a comparison between typical galaxy morphologies in the local (left) and distant (right) universe as seen by HST. However, with the advent of the James Webb Space Telescope (JWST), observations at longer wavelengths have revealed that many galaxies appearing clumpy in HST images actually exhibit well-defined spiral structures even at beyond $z > 1.5$

(Ferreira et al., 2022). This finding highlights the importance of rest-frame infrared studies with MIRI to investigate galaxy morphologies and quantify dust-obscured star formation in the early Universe.

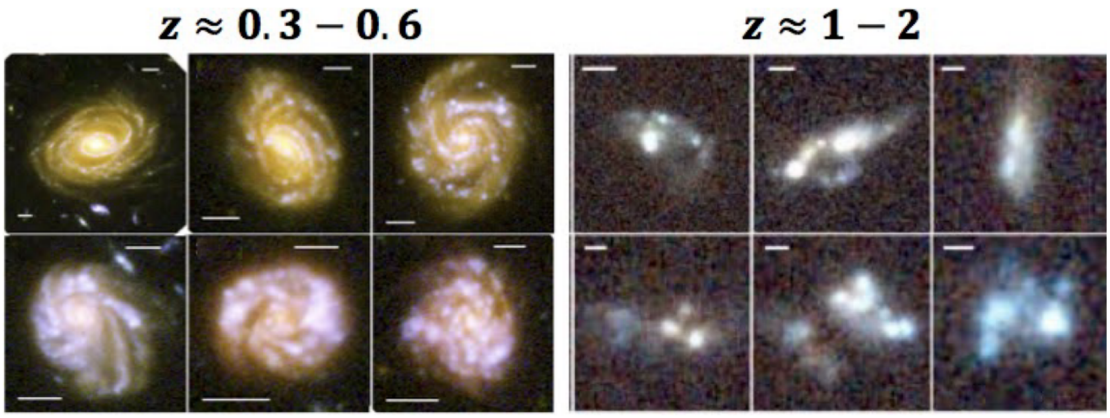

Figure 1.3: HST images of galaxies in the local (left) and distant (right) universe, showing the clumpiness of galaxies at high redshifts. Image adapted from Mcdermid et al. (2020).

The formation history of the Hubble sequence also appears to correlate with the stellar mass of the galaxies, with more massive systems settling into Hubble-type morphologies earlier, whereas lower-mass systems remain disturbed for longer (Mortlock et al., 2013). These studies highlight that although the present-day Hubble sequence was not yet fully established at cosmic noon, its foundations were already being laid, linking the structural transformation of galaxies to their star-formation activity and mass growth.

As the morphologies of galaxies became better understood, it also became clear that structural classification in the optical band alone could not fully capture the diversity of galaxy populations. Building on Hubble's work, Holmberg (1958) was among the first to recognise that morphology correlates with other key physical properties of galaxies. This connection was later confirmed and quantified using large statistical samples from the Sloan Digital Sky Survey (SDSS; York et al. (2000)), which revealed a striking bimodality in galaxy colours that broadly mirrors morphological type (Saftly et al., 2015). In general, elliptical galaxies tend to be massive and red, with little or no ongoing star formation, whereas spiral and irregular galaxies are typically less massive, actively forming stars, and bluer in colour. Figure 1.4 shows an example of this bimodality reported in Weigel et al. (2016).

However, inferring properties such as the star formation history of a galaxy only became possible thanks to the significant advances made in modern spectroscopy. It is important to distinguish, therefore, between morphological classifications, which are heavily dependent on wavelength, and the classifications based on star formation rate, which require spectroscopic measurements and thus rely on the intrinsic properties of galaxies. While the discussed classification schemes coincide in many cases, they do not always yield consistent results. A detailed analysis of the influence of different selection criteria (morphological, photometric, and spectroscopic) on the classification of galaxies within the same sample is provided in Moresco et al. (2013).

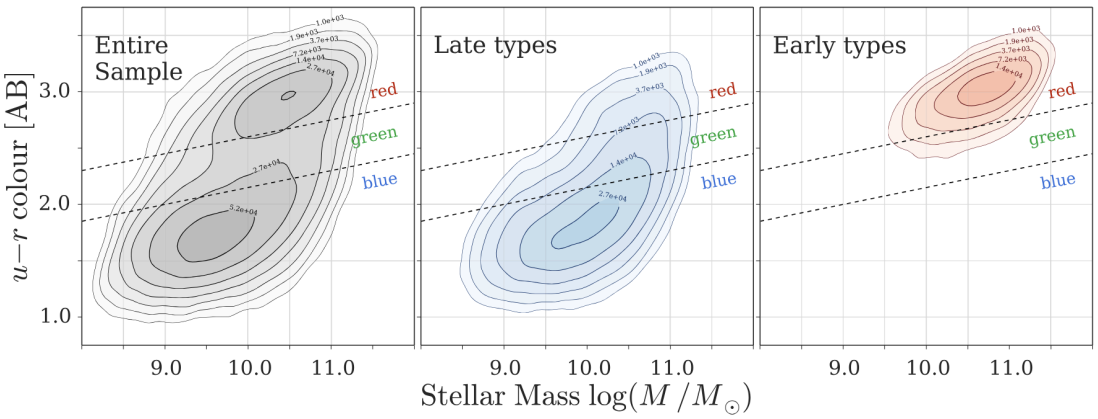

Figure 1.4: The bimodal distribution of ∼110.000 present-day galaxies in the rest-frame $u^* - r^*$ colour-mass diagram, as reported in Weigel et al. (2016).

In a broader sense, the strong correlation between galaxy morphology and star formation activity allows for the alternative classification of early-type galaxies as *quiescent* or *passive*, whereas late-type galaxies are typically classified as star-forming. Across the redshift range $0 < z < 2$ — and likely even earlier — the majority of star-forming galaxies are found to follow a relatively tight correlation between their star formation rates (SFRs) and stellar masses, commonly referred to as the "star-forming main sequence" (Brinchmann et al., 2004; Daddi et al., 2007; Noeske et al., 2007). A smaller population of starburst galaxies lies above this relation, exhibiting increased SFRs, while an increasingly prominent population of quiescent galaxies occupies the region below it.

With the wealth of new observational data collected over the past decades, galaxy taxonomy was expanded to include a range of populations identified through their emission properties — Lyman Break Galaxies (LBGs), Lyman-α Emitters (LAEs), Extremely Red Objects (EROs), BzKs, Distant Red Galaxies (DRGs), Dust-Obscured Galaxies (DOGs), Luminous and Ultraluminous Infrared Galaxies (LIRGs and ULIRGs), and Submillimetre Galaxies (SMGs), among others. Making sense of this diversity and fitting it into a coherent framework remains one of astronomy's enduring challenges, owing both to the observational difficulty of tracing continuously evolving subpopulations across cosmic time and to the incomplete theoretical understanding of the processes that drive this evolution (Madau & Dickinson, 2014).

Ideally, a comprehensive picture of galaxy evolution would encompass the full sequence of events leading from the formation of the first stars after the cosmic dark ages to the present-day variety of galactic morphologies, masses, and colours. To understand the origins of the complex and diverse evolutionary histories of individual galaxies, as well as the interplay between star formation, stellar populations, and interstellar medium properties at high redshift, it is therefore essential to study the full spectral energy distributions (SEDs) of individual systems. In particular, reconstructing their emission from the ultraviolet (UV) to the far-infrared (FIR) allows us to disentangle the contributions from young and old stars, gas, and dust, providing a more complete view of galaxy evolution during cosmic noon.

1.2 The Importance of Dust in the ISM

As mentioned in the previous section, the luminosities and colours of galaxies provide crucial information about their star formation activity, stellar content, and evolutionary history. Particularly, rest-frame ultraviolet (UV) light traces young, massive stars and, together with the assumption of an IMF, it is widely used as a star formation rate indicator at high redshift. However, UV measurements alone systematically underestimate the intrinsic star formation rate, as dust grains in the interstellar medium absorb a significant fraction of stellar light, especially at shorter wavelengths, and re-emit this energy in the infrared (IR). This energy balance between attenuated starlight and dust emission underpins much of our understanding of galaxy evolution, since the far-IR luminosity serves as a powerful tracer of ongoing star formation (Kennicutt Jr, 1998).

The presence of dust in galaxies was first inferred by Trumpler (1930) due to the obscuration, or 'extinction', of stellar light along the line of sight. Since then, dust has been recognised as a key component of the interstellar medium (ISM), affecting its chemical composition and influencing the dynamics of star formation (B. T. Draine, 2011). Dust grains absorb and scatter radiation coming from stars and active galactic nuclei (AGN), particularly at shorter wavelengths, and re-emit this energy through a modified blackbody in the infrared, making it the dominant source of emission in the far-IR and sub-millimetre regimes (Viaene et al., 2016).

A large number of studies have been conducted to investigate the wavelength-dependence of dust attenuation, often referred to as *reddening*, since shorter wavelengths are more prominently affected than longer wavelengths. This wavelength-dependence can be used to constrain the grain size distribution, while prominent spectral features provide insight into the chemical composition of dust (B. Draine, 2003). It has been estimated that up to $\sim$30% of the stellar energy output in local galaxies is reprocessed by dust, with even higher fractions observed in starburst systems (Popescu & Tuffs, 2002; Soifer & Neugebauer, 1991). On a global scale, the fraction of stellar energy re-emitted by dust provides a means of estimating the extragalactic background light (Skibba et al., 2011). Indeed, Hauser and Dwek (2001) suggested that nearly half of the Universe's bolometric luminosity is channelled through the mid- and far-infrared output of galaxies.

Understanding the physics of dust emission is therefore crucial not only for deriving robust star formation rates and stellar masses but also for interpreting galaxy scaling relations, constructing luminosity functions, and comparing observations to theoretical models. In this thesis, I focus on the dust emission of galaxies at cosmic noon, where the interplay between vigorous star formation and dust obscuration peaks, making infrared observations indispensable for building a complete picture of galaxy evolution at this epoch.

1.3 Modelling the SEDs of Galaxies

The spectral energy distribution (SED) of a galaxy encodes a wealth of physical information about its evolutionary history, ranging from the age and metallicities of stellar populations over tracers of past merging events to the presence of active galactic nuclei

(AGNs). With the advance of Bayesian forward-modelling techniques, fitting spectral energy distributions of galaxies has become the primary method for inferring their physical properties, which can then be compared to models of galaxy evolution (see reviews by Conroy (2013) and Walcher et al. (2011)).

SED fitting codes consist of three components: a physical model, a set of observations such as photometry or spectroscopy, and a statistical inference framework that connects the model to the data. The physical models are typically based on stellar population synthesis (SPS) codes, which combine inputs such as isochrones, stellar spectra, an initial mass function (IMF), and assumptions about star formation and chemical enrichment histories to construct the SEDs of complex stellar populations (Johnson et al., 2021).

Numerous SPS codes are publicly available, each treating these ingredients with varying degrees of sophistication. Examples include Galaxev (Bruzual & Charlot, 2003), Fsps (Conroy et al., 2009), and Bpass (Eldridge et al., 2017).

SED fitting can be performed using either broadband photometry, spectroscopy, or a combination of both. Broadband photometry comes with the advantage of providing flux measurements over a wide wavelength range and allows for the efficient analysis of large galaxy samples, albeit at the cost of losing detailed spectral information. Spectroscopic fitting, on the other hand, captures fine spectral features such as absorption and emission lines, providing tighter constraints on important parameters such as redshifts, stellar ages, and metallicities. However, spectroscopy is more observationally demanding and typically cannot cover wide wavelength ranges at high resolution. As a result, high-resolution spectra are usually limited to relatively narrow spectral windows.

Recently, joint photometric and spectroscopic fitting has become increasingly popular, as it combines the broad wavelength coverage of photometry with high-resolution spectroscopy showing individual absorption and emission lines, thus allowing for tighter constraints on star formation histories and chemical abundance. Figure 1.5 shows an example of a spectral energy distribution inferred using HST and JWST/NIRCam photometry together with NIRSpec spectroscopy.

As mentioned above, one of the most fundamental quantities inferred from SED fitting is the star formation history (SFH) of a galaxy, which describes the evolution of the star formation rate over time. Since the pioneering efforts of Tinsley (1980), it has long been common to limit star formation histories of galaxies to a relatively simple functional form described by a few parameters, $\mathrm{SFR}(t) = f(t, \theta)$. The characterisation of the potentially complex SFH of a galaxy by a few parameters is especially effective at limiting the SED grid size and makes any Bayesian inference more tractable, while keeping the model simple. A variety of different parametrisations have been proposed (Simha et al., 2014), with the most prominent being the "τ-model", with $\dot{M}_* \propto t\, e^{-(t-t_i)/\tau}$ (e.g., Bruzual, 1983; Papovich et al., 2001). However, assuming a functional form for the SFH is effectively equivalent to imposing a strong prior on its shape, and it remains unclear how well these simple models reproduce the diverse and complex SFHs of real galaxies (e.g., Gallagher III et al., 1984).

A natural way to model more complex SFHs is to increase the flexibility of parametric models by introducing additional components (e.g., A. Carnall et al., 2018; Salim et al., 2007) or to rely on libraries of SFHs based on semianalytical or hydrodynamical

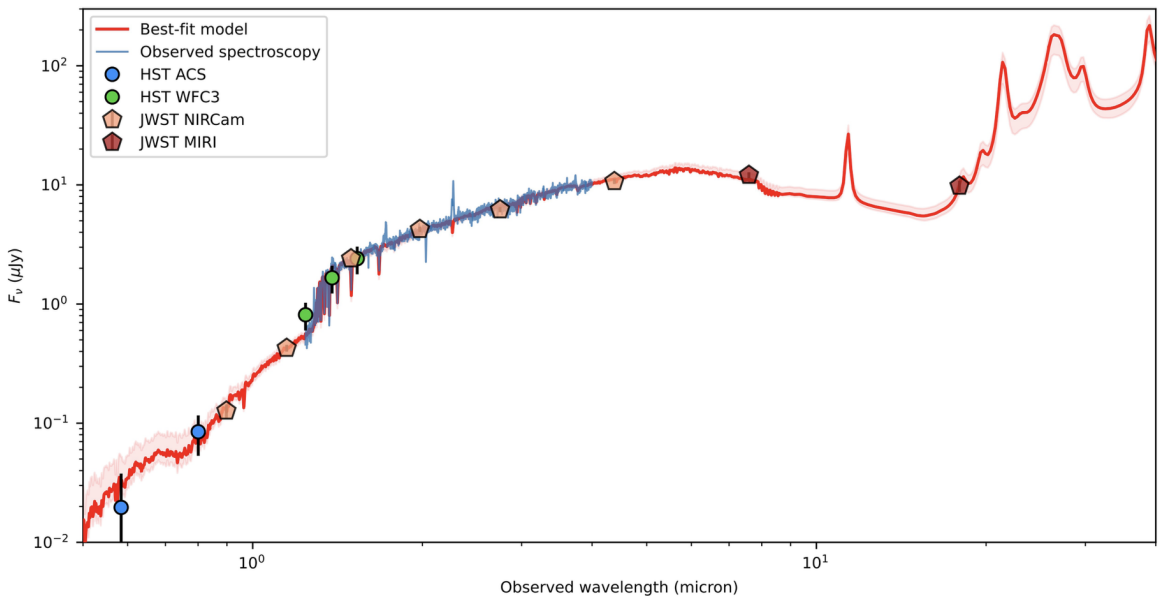

Figure 1.5: Spectral energy distribution of the post-starburst galaxy analysed in Belli et al. (2024). Points indicate the observed photometric data obtained with the ACS and WFC3 instruments aboard HST (circles), and with the NIRCam and MIRI instruments aboard JWST (pentagons). The blue and red lines show the observed NIRSpec spectrum and the best-fit model spectrum, respectively.

simulations (e.g., Da Cunha et al., 2008; Pacifici et al., 2012).

Moving to the extreme, one can drop the functional dependence entirely and instead use a piecewise constant or δ-function SFH, where the stellar mass formed within each bin becomes a parameter of the model (Johnson et al., 2021; Leja et al., 2019). Despite being called "non-parametric", these models actually include a large number of parameters and have become a popular tool for star formation history inference. Figure 1.6 shows a comparison of the SFH inferred by a parametric and a nonparametric model for two *Illustris* mock galaxies discussed in Johnson et al. (2021). In these examples, the parametric model tends to reproduce the shape of the recent SFH, which is dominated by the young stars that contribute most to the optical light. It does so even if this comes at the expense of accuracy at earlier epochs, when the prior limits flexibility. In contrast, the nonparametric model, with its greater freedom, more reliably recovers both recent and older star formation episodes.

1.3.1 The Prospector Framework

In this work, I focus on Prospector[1] (Johnson et al., 2021), a modern stellar population inference code built upon the Fsps library. It introduces a fully Bayesian framework that allows for flexible modelling of dust and nebular emission, while also providing robust uncertainty estimates. Besides supporting all parametric star formation histories available in Fsps, Prospector is also capable of inferring more complex nonparametric SFHs, as discussed above.

[1] https://github.com/bd-j/prospector

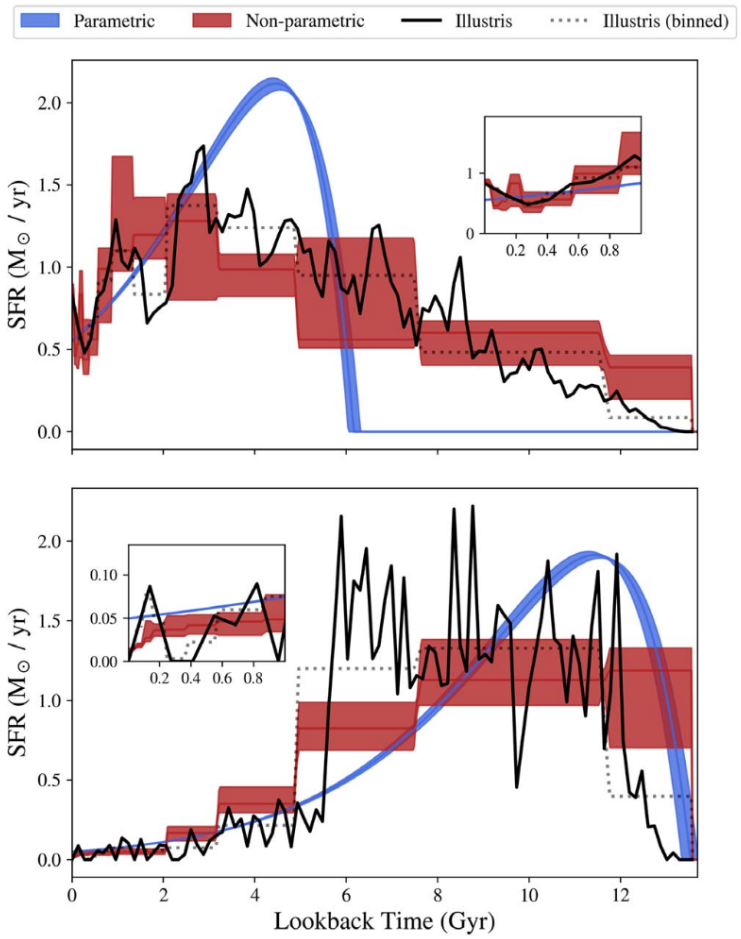

Figure 1.6: Posterior star formation histories (SFHs) inferred from mock optical spectra (S/N∼100) without nebular emission and with perfect spectrophotometric calibration. Mock data are generated from an Illustris SFH (black). Shaded regions indicate the 16th–84th percentile credible intervals for parametric (blue) and nonparametric (maroon) fits. The nonparametric SFH uses 14 time bins with a continuity prior; dotted grey lines show the true average SFR in each bin. Insets highlight the recent SFH (<1 Gyr). Image taken from Johnson et al. (2021).

The code operates by forward-modelling a galaxy's observed spectrum and photometry using parameters that describe its stellar populations, dust, and gas, alongside relevant instrumental quantities. In principle, every parameter in the FSPS code can be a potential parameter of the fit, and it is up to the user to decide whether it is fixed or free to vary. Such parameters include the IMF slope, AGB star properties, or the blue-straggler fraction, as well as more conventional population parameters like stellar metallicity and dust attenuation (including attenuation curve shape and age dependence; see Section 1.3.2). Nebular emission parameters may also be varied. Parameters that alter the SSPs require regenerating them, which is computationally expensive. By contrast, certain quantities, such as redshift and spectral smoothing, are managed directly within PROSPECTOR rather than FSPS.

To connect the models to data, PROSPECTOR applies prior distributions and a noise model to compute the likelihood and posterior probability. Priors can be of particular importance as they can strongly influence the shape of posterior distributions in the often highly degenerate parameter space of SED fitting, especially if high-quality data

is lacking or incomplete (A. C. Carnall et al., 2019; Leja et al., 2017).

The primary inference method employed by Prospector is nested sampling (Skilling, 2004). This algorithm iteratively draws samples from the prior distribution while progressively restricting them to regions of higher likelihood. By tracking the shrinking prior volume enclosed within iso-likelihood contours, nested sampling provides an estimate of the Bayesian evidence. At the same time, the weighted sequence of samples can be used to reconstruct the posterior distribution of the various model parameters.

In Prospector, this is implemented using the `dynesty` pure Python code package (Speagle, 2020), though users may alternatively choose the ensemble MCMC algorithm of Goodman and Weare (2010) via the `emcee` Python package (Foreman-Mackey et al., 2013). By propagating prior knowledge into the posterior PDFs, Prospector is able to deliver statistically robust constraints on a large number of physical parameters, including dust properties and star formation histories of individual galaxies (Johnson et al., 2021).

1.3.2 The Concept of Dust Energy Balance

Dust grains in galaxies absorb stellar light, predominantly in the ultraviolet and optical, and re-emit this energy at infrared wavelengths. The assumption of dust energy balance formalises this process by requiring that the total energy absorbed by dust equals the total energy re-radiated in the infrared. This provides a physically motivated way of linking the UV–NIR and IR parts of a galaxy's SED, allowing the total infrared luminosity to be inferred even when direct far-IR observations are sparse or incomplete (Da Cunha et al., 2008).

Early efforts to model this process relied on solving the radiative transfer equation for idealised distributions of stars and dust (Gordon et al., 2001; Rowan-Robinson, 1980). Later developments incorporated the evolutionary histories of stellar populations alongside dust, providing more realistic predictions of galaxy SEDs (Silva et al., 1998). While such radiative transfer models are highly effective at interpreting the detailed emission of individual galaxies, their computational complexity makes them poorly suited for deriving statistical constraints from large galaxy samples (Da Cunha et al., 2008).

Modern SED fitting codes instead adopt simplified but physically motivated approaches to dust emission, which can be more broadly applied to large surveys. Within Prospector, dust energy balance is imposed by construction: all energy attenuated in the UV–NIR is re-emitted in the IR (Johnson et al., 2021). Dust absorption is implemented via the Fsps library, which allows the user to choose among a variety of dust absorption models, including the Milky Way extinction curve of Cardelli et al. (1989), empirical absorption curves from Calzetti et al. (2000) and Kriek and Conroy (2013), and the radiative transfer models of Witt and Gordon (2000). In the Bayesian framework, the imposed relation between dust absorption and emission not only improves inference when IR data are lacking, but is also linked to the choice of priors, which can strongly influence the shape of posterior distributions in the often highly degenerate parameter space of SED fitting (A. C. Carnall et al., 2019; Leja et al., 2017).

The limitations of this approach have been outlined in Appendix C of Leja et al. (2017), where it was found that - given strong priors on FIR emission - Prospector was able to fit the UV–MIR spectral energy distributions of galaxies surprisingly well, independently of whether or not *Herschel* photometry in the FIR was included. However, the absence of direct FIR constraints led to systematic biases in the predicted infrared luminosities, star formation rates, and dust attenuations, as well as large uncertainties in the implied mid- to far-infrared fluxes. As a possible explanation, Leja et al. (2017) suggest a link to the dust energy problem, where FIR fluxes tend to be underpredicted by factors of 3–4 when using radiative transfer models to fit the UV-NIR emission (Baes et al., 2010; Bianchi et al., 2000; Saftly et al., 2015). Possible explanations include the complex geometry of spiral galaxies with respect to the line of sight or additional dust components present in the host galaxies.

1.4 Scope of this Work

Building on previous studies highlighting both the power and the limitations of existing dust modelling techniques, the primary aim of this work is to further test the validity of dust energy balance within the Prospector stellar population synthesis framework and to quantify its capability of recovering infrared fluxes in a sample of massive galaxies with redshifts between $1.7 < z < 3.5$.

The structure of this thesis is as follows. Chapter 2 provides an overview of JWST and its instruments, with a particular emphasis on MIRI. Chapter 3 provides an overview of the observational data used in this work. The photometric workflow is described in great detail in Chapter 4, together with an introduction to the `miri_utils` custom Python library. In Chapter 5, I present the final photometric catalogue, compare it to the COSMOS2025 catalogue for measurement validation, and discuss detection statistics with MIRI. Chapter 6 focuses on investigating dust energy balance in Prospector using existing spectra and photometry in the rest-frame optical/UV. Finally, in Chapter 7, I provide an overarching summary of my work and discuss the major findings. I conclude this thesis with a brief outlook on how future projects can build upon this work to improve our understanding of the role of dust in early galaxy evolution.

Chapter 2

The James Webb Space Telescope

Observational data are strongly tied to the capabilities and limitations of the instruments used to obtain them. Every telescope imposes constraints on wavelength coverage, sensitivity, and resolution, which influence the types of scientific questions that can be addressed. In this thesis, the primary observing facility employed is the James Webb Space Telescope, whose unprecedented infrared sensitivity and large collecting area have opened a new window onto the high-redshift universe (Figure 2.1). This chapter provides an overview of JWST, its instruments, with a special emphasis on the Mid-Infrared Instrument (MIRI).

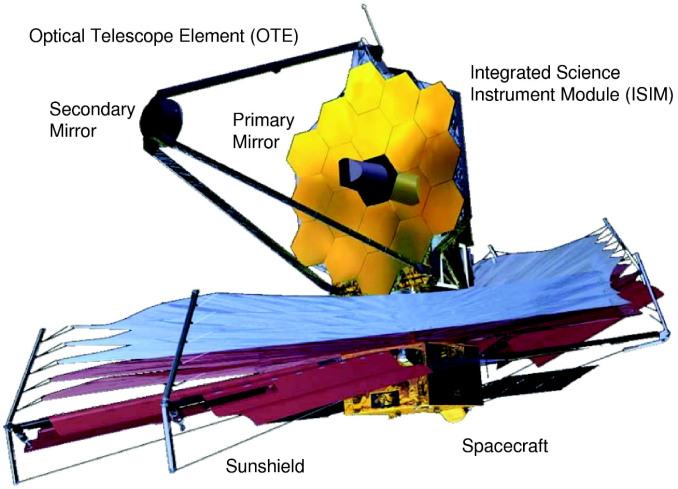

Figure 2.1: Overview of the JWST observatory, including the Optical Telescope Element (OTE) and the Integrated Science Instrument Module (ISIM), together with the sunshield and the spacecraft. Image taken from Gardner et al. (2006).

The James Webb Telescope (JWST; Gardner et al., 2006, 2023) was launched at 12:20 UTC on 25 December 2021 aboard an ESA-provided Ariane 5 rocket from French Guiana. It is a 6.5-metre class cryogenically cooled space observatory designed as the scientific successor to Hubble and Spitzer. From the outset, JWST was conceived as an international collaboration led by NASA with ESA and the Canadian Space Agency, and its observing time is open to astronomers worldwide. Thanks to a highly efficient launch and insertion into the Sun-Earth Lagrange point (L2), the observatory

is expected to operate for up to 20 years. Commissioning was completed on 12 July 2022, with all 17 observing modes across its four scientific instruments declared fully operational.

JWST provides imaging and spectroscopy across 0.6–28 μm, enabling observations that are not possible with ground-based facilities due to atmospheric opacity and thermal background. Its infrared sensitivity allows astronomers to probe galaxies beyond redshifts of $z15$, corresponding to within $\leq$300 Myr of the Big Bang, and to study dust-obscured active galactic nuclei (AGN), star-forming regions, planetary system formation, and exoplanet atmospheres. By combining a large collecting area with cryogenic cooling, JWST is capable of reaching sensitivities far exceeding those of previous space observatories in the near- to mid-infrared, such as Hubble, IRAS, and Spitzer.

Because of JWST's unprecedented collecting area and the need for a large sunshield to shield its infrared instruments from Solar radiation, launching the observatory presented one of the programme's greatest engineering challenges. To fit within the Ariane 5 launch vehicle, both the sunshield and the mirror segments had to be folded into the rocket's payload fairing and subsequently deployed in space. During the first weeks after launch, JWST underwent a carefully staged deployment sequence, beginning with the gradual release of the sunshield, which required 140 individual release mechanisms, followed by the unfolding of the mirrors. Both procedures were completed successfully before the telescope reached its operational orbit around L2, 29 days after launch.

This chapter is structured as follows: Section 2.1 outlines the broad scientific goals of JWST, Section 2.2 describes the telescope and spacecraft architecture, and Sections 2.3 and 2.4 provide an overview of the scientific instruments, including a detailed description of the Mid-Infrared Instrument (MIRI), which is central to this work.

2.1 The Science Scope

The main scientific objectives of the JWST can be grouped into four primary themes, which will be summarised below. For a more detailed discussion, see Gardner (2005) and Gardner et al. (2006).

The End of the Dark Ages: First Light and Reionisation

Current cosmological models predict that the very first generation of stars emerged approximately 180 million years after the Big Bang, when the universe was composed primarily of dark energy, dark matter, and primordial baryons, including hydrogen, helium, and traces of Lithium. These so-called Population III stars are believed to have reached masses between 30 and 300 times that of our Sun, thus making them short-lived but highly luminous. Their lifecycle ended in core-collapse supernovae or direct collapse into black holes, which initiated both chemical enrichment of the interstellar medium and the growth of early black holes, which are precursors to the supermassive black holes observed at the centres of most massive galaxies today.

JWST is uniquely equipped to observe these early stages of the universe thanks to its sensitivity in the near- and mid-infrared, which enables the detection of high-redshift galaxies, individual supernovae, and accreting black holes (mini-quasars). A

key JWST science goal is to study the epoch of reionisation, when ultraviolet radiation from early stars and galaxies ionised neutral hydrogen in the intergalactic medium. By conducting ultra-deep surveys and spectroscopy, JWST aims to characterise the timing, mechanisms, and sources driving this cosmic phase transition.

The Assembly of Galaxies

In the prevailing cosmological framework, galaxy formation follows a hierarchical process, whereby smaller dark matter halos merge to form larger structures. This assembly process is accompanied by the progressive chemical enrichment of the interstellar medium through successive generations of stars, shaping the structural and dynamical properties of present-day galaxies. Despite prior detections of high-redshift galaxies, many aspects of their formation and evolution remain unresolved.

JWST plays a pivotal role in addressing these open questions. Its capabilities enable the detection and characterisation of galaxies in the early universe, providing insight into the formation of the Hubble Sequence, the origins of chemical elements, and the physical processes shaping galaxy properties. Through deep- and wide-field imaging and spectroscopy, JWST will survey thousands of galaxies across a range of environments and redshifts. It will also conduct focused studies of extreme sources such as ultra-luminous infrared galaxies (ULIRGs) and active galactic nuclei (AGN), shedding light on the mechanisms driving starbursts and black hole activity in the context of galaxy evolution.

The Birth of Stars and Protoplanetary Systems

Although stars have been a central focus of astronomy for millennia, advances in observational techniques and computational modelling have only relatively recently allowed for a deeper understanding of their formation and evolution. Despite these breakthroughs, many aspects remain poorly constrained, including the collapse of gas clouds, cluster formation, and the interplay of chemical and radiative processes.

Recent discoveries of gas giants orbiting unexpectedly close to stars similar to the Sun have challenged existing theories. Developing a comprehensive model of planet formation requires further observational evidence, particularly from studies of young circumstellar discs and older debris discs where planetary signatures can be detected. The James Webb Space Telescope will observe stars across all stages of their evolution, ranging from the collapse of dust-enshrouded protostellar clouds to the formation of mature planetary systems. By penetrating the dust that obscures early stellar development, JWST will characterise the physical processes driving star and planet formation, determine the sub-stellar initial mass function, and provide critical insights into the role of environment in shaping the properties of stellar and planetary systems.

Planetary Systems and the Origins of Life

Unravelling the origin of the Earth and its capacity to support life is a fundamental goal of modern astronomy. Critical to this endeavour is understanding the formation and evolution of planetesimals and their assembly into larger planetary bodies. Many

open questions have yet to be answered, such as the mechanisms by which planets acquire their current orbits and the influence of giant planets on the dynamical evolution of smaller bodies within planetary systems. Understanding the chemical and physical history of early Solar System objects is crucial for identifying the processes that provided the raw materials necessary for life on Earth. Using coronagraphy, JWST will investigate the formation and architecture of planetary systems through observations of circumstellar discs and exoplanets, offering insight into habitable zone conditions and the potential for life-supporting environments beyond our Solar System. These observations will be compared with Solar System analogues, providing a broader picture for the emergence of life-supporting planets.

2.2 Spacecraft and Telescope Design

The JWST observatory is primarily composed of the Optical Telescope Element (OTE), the Integrated Science Instrument Module (ISIM) containing the scientific instruments, a spacecraft, and a sunshield. All components are described in great detail in Gardner et al. (2006, 2023) and will be briefly discussed below.

2.2.1 Optical Telescope Element

Technologically, JWST represents a series of pioneering advances. Its Optical Telescope Element (OTE) consists of an 18-segment beryllium primary mirror, a convex 0.8 m secondary mirror mounted on a deployable tripod, and an aft assembly housing the tertiary and fine-steering mirrors. All mirrors are gold-coated, providing high reflectivity across JWST's broad operating wavelength range. With a total collecting area of 25.4 m^2, the OTE is the first segmented, deployable space telescope of its kind. The primary mirror segments and secondary mirror were aligned in orbit using actuators offering 132 degrees of freedom, enabling precise figure control and disturbance attenuation.

The OTE follows a three-mirror anastigmat design, resulting in an effective f/number of 20 and an effective focal length of 131.4 m. This configuration delivers high image quality across a wide field of view, with residual optical aberrations contributing only a small fraction to the total wavefront error (WFE). Light exiting the OTE is focused on the ISIM focal surface, where several pickoff mirrors funnel the light towards the science instruments. The telescope was designed to be diffraction-limited at 2 µm, corresponding to a Strehl ratio of $\gtrsim$0.8 and a root mean squared (rms) WFE requirement of 150 nm. In practice, commissioning demonstrated significantly better performance, with a measured WFE of ∼80 nm rms, allowing diffraction-limited imaging at 1.1 µm. Figure 2.2 provides an overview of the JWST OTE and the locations of the tertiary and fine steering mirrors.

A fine-steering mirror (FSM) is located at a pupil plane downstream of the tertiary mirror and provides image stabilisation in tandem with JWST's highly stable spacecraft architecture. This system suppresses line-of-sight jitter and ensures that diffraction-limited performance at ∼2 µm is maintained. The careful optical design and allocation of WFE across the field of view allowed each science instrument to be placed in a

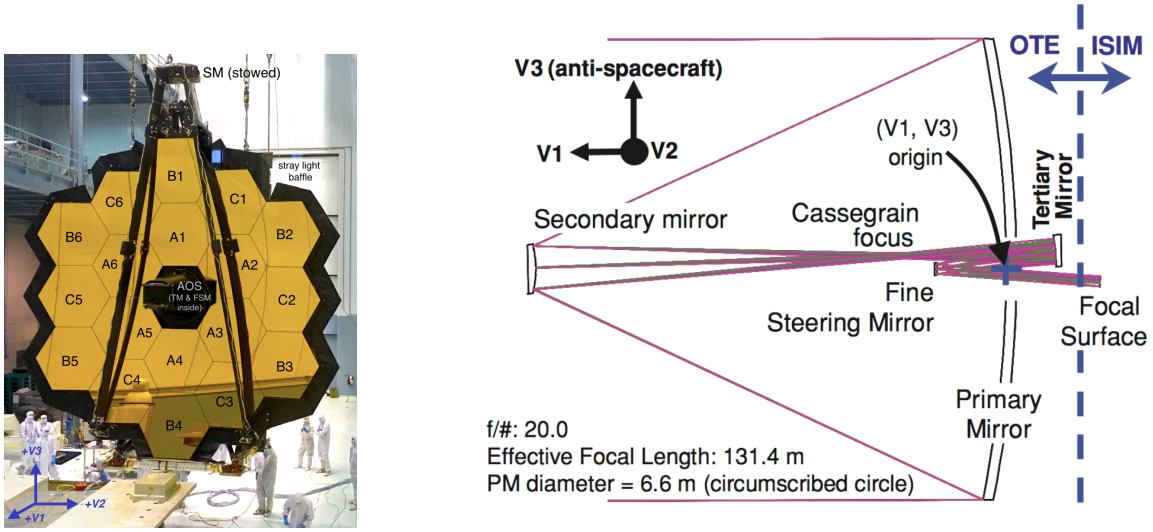

Figure 2.2: The primary mirror of JWST with labels for each mirror segment (left) and a schematic overview of the OTE showing the position of the tertiary and fine steering mirrors within the aft optics systems. The telescope (V1,V2,V3) coordinate system is also shown, where +V1 represents the telescope boresight. Images taken from the JWST User Documentation and Gardner et al. (2006), respectively.

region optimised for its needs: NIRCam occupies the lowest-WFE region, while MIRI, NIRSpec, and the fine guidance sensor are positioned in slightly higher-WFE areas that nonetheless meet their performance requirements (Gardner et al., 2006).

2.2.2 Spacecraft

The JWST spacecraft provides the power to the observatory and is responsible for pointing adjustments, orbit maintenance, data storage, and communications. At the end of commissioning, the solar array supplied an average of 1.5 kW to the telescope, with a peak capability of 3 kW. The pointing system consists of star trackers, inertial reference units (IRUs) with gyros, reaction wheels, and a fine-steering mirror. Three star trackers are installed (one redundant), while two IRUs, each with four gyros (one redundant per IRU), support attitude control. Six reaction wheels (two redundant) maintain coarse pointing along with the star trackers and gyros. Fine guidance is achieved using the fine guidance sensor (FGS; Rowlands et al., 2003), which provides 16 Hz positional updates to the FSM upon guide star acquisition. With a resulting pointing stability of ∼1.5 mas (1σ per axis), JWST greatly exceeded the prelaunch requirement of 4 mas. Currently, JWST uses its onboard thrusters approximately every six weeks to maintain its orbit and to dissipate angular momentum by de-spinning the reaction wheels.

The JWST sunshield is made of five layers of Kapton, each about 14m × 22m, which separate the warm spacecraft from the cold telescope and reduce the intense Solar radiation from ∼200 kW to mW levels. Its design allows the telescope to observe about 40% of the sky at any one time, and every point on the sky can be observed at least once every six months. The telescope can tilt slightly toward or away from the Sun and rotate around the Sun–anti-Sun axis.

The observatory began passively cooling immediately after launch, a process that took 120 days to complete. During this period, heaters were employed to control the cool-down and prevent contamination of the instruments by outgassing water or other volatiles. The exception is MIRI: With its cryocooler being the only active cooling system onboard JWST, it started cooling after deployment and reached its operating temperature on day 104 after launch. At the end of the cooling period, the secondary mirror reached a temperature of 29.2K, whereas temperatures on the primary mirror ranged from 34.7 to 54.5K, with parts closer to the sunshield being warmer. These very low temperatures ensure that JWST's infrared observations are limited mainly by zodiacal light up to 12.5µm, and by the telescope's thermal self-emission at longer wavelengths. The temperature of the near-infrared instruments, such as NIRCam and NIRISS, is actively maintained using heaters to remain at 38.5K, while NIRSpec is kept at 42.8K. MIRI is actively cooled down to about 6 to 20K to ensure sensitivity to faint mid-infrared signals, as discussed in Section 2.4.4.

2.3 Near-Infrared Instruments

JWST is equipped with four science instruments, which are hosted in the Integrated Science Instrument Module (ISIM) and provided with thermal, electrical, structural, and data handling support (Gardner et al., 2006, 2023). The ISIM consists of NIRCam, NIRSpec, NIRiss, and MIRI, resulting in a total of 17 science instrument modes. The first three of these modules will be discussed in more detail in this section, while the Mid-Infrared Instrument (MIRI) will be treated in a separate section.

2.3.1 NIRCam

The Near-Infrared Camera (NIRCam; Horner and Rieke, 2004; M. J. Rieke et al., 2003, 2023) is JWST's primary near-infrared imager, covering wavelengths from 0.6 to 5.0 µm. It consists of two identical modules, each split into short- and long-wavelength channels by a dichroic at 2.4 µm, enabling simultaneous imaging in two filters with a total field of view of 2.2 × 4.4 arcmin^2. NIRCam's filter set includes two extra-wide, eight broad-band, twelve medium-band, and seven narrow-band filters. The broad-band filters span the full wavelength coverage of the instrument, while the extra-wide and medium-band filters cover ranges of 1.0–4.0 µm and 1.4–5.0 µm, respectively. The narrow-band filters are selected to isolate specific spectral lines. Figure 2.3 shows the filter profiles in short- and long-wavelength modules, including the dichroic deadband. Almost all of NIRCam's filters exceeded pre-launch sensitivity expectations, making NIRCam imaging one of the most-used modes in Cycle 1 programmes.

Besides its imaging capabilities, NIRCam includes additional observing modes: wide-field slitless spectroscopy for 2.5–5.0 µm, which enables simultaneous low- to medium-resolution spectra of all sources in its field of view; coronagraphy, which uses specialised masks to suppress bright starlight and reveal faint companions; and Bright Object Time Series (BOTS) observations, designed for high-cadence monitoring of relatively bright sources such as transiting exoplanets. These capabilities expand NIR-Cam's scientific applications from high-redshift galaxy surveys to detailed studies of nearby stellar and planetary systems.

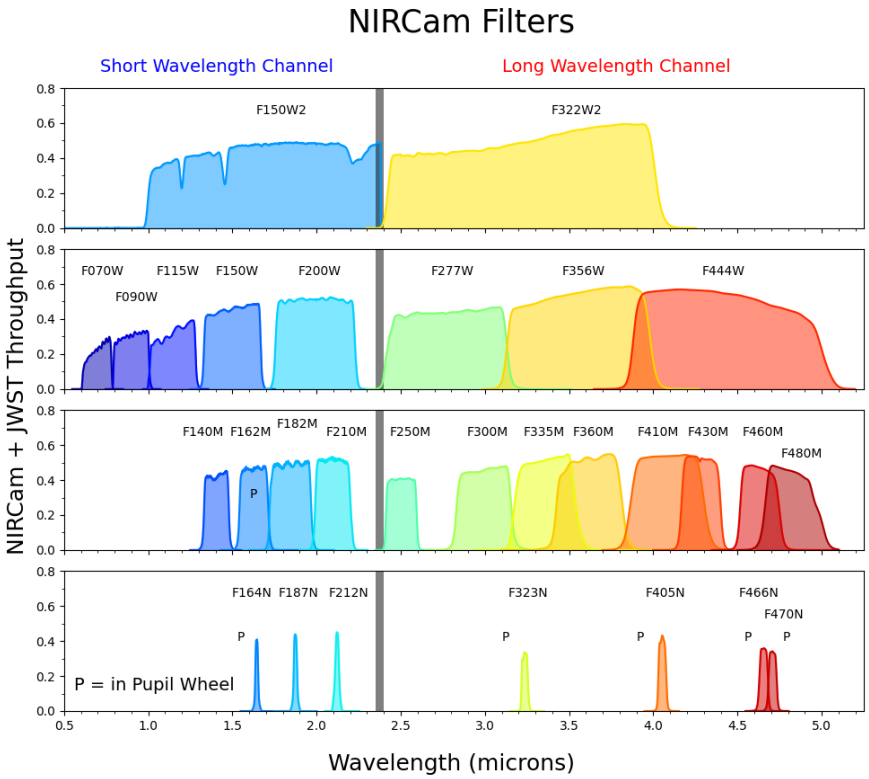

Figure 2.3: Throughputs of NIRCam filters, including all contributions from the telescope optics, instrument optics, and detector quantum efficiency. The letter "P" indicates filters mounted on the pupil wheels, and the shaded region denotes the dichroic deadband. Image taken from M. J. Rieke et al. (2023).

2.3.2 NIRSpec

The Near-Infrared Spectrograph (NIRSpec; Böker et al., 2023; Jakobsen et al., 2022) provides spectroscopy between 0.6 and 5.3 μm, enabling a broad range of science applications from exploratory redshift measurements to detailed kinematic studies of galaxies. Dispersion is achieved using either a prism (R=30-300) or one of its gratings, one at medium (R=500–1343) and one at high resolution (R=1321–3690).

NIRSpec offers four main observing modes: Multi-Object Spectroscopy (MOS; Ferruit et al., 2022) uses the Micro Shutter Assembly (MSA), a micro-electromechanical system comprising four quadrants of individually addressable shutters (0.20×0.46 arcsec each), allowing simultaneous observation of up to 100 targets over a field of view of 3.6×3.4 arcmin. Fixed slit spectroscopy provides the highest contrast and throughput for individual targets using one of five fixed slits. Integral Field Unit (IFU; Böker et al., 2022) spectroscopy covers a contiguous area of 3.1"×3.2", sliced into 900 spaxels of 0.103" × 0.105" each. This mode produces full spectral data cubes and hence provides the most complete information on a single object in the near-infrared. Finally, the Bright Object Time Series (BOTS) mode (Birkmann et al., 2022) enables high-cadence monitoring of bright, time-variable sources, such as exoplanet transits, reaching readout times as short as 0.28 seconds.

2.3.3 NIRISS

The Near-Infrared Imager and Slitless Spectrograph (NIRISS; Doyon et al., 2012, 2023) was established as its own instrument module during a replan project in the early 2000s, reducing JWST's 8m telescope aperture to 6.5m. Originally, its filter wheels and the tunable filter modules were intended to be a part of NIRCam and specifically designed to detect Lyα emitters. Upon reconfiguration, the tunable filters were displaced out of NIRCam into a new instrument, the Tunable Filter Imager (TFI; Rowlands et al., 2004), which was further developed into NIRISS. Despite the attempt to add new observing modes, several modes were chosen to provide additional redundancy for broadband imaging to NIRCam, multi-object spectroscopy to NIRSpec, and white light guiding to FGS.

NIRISS includes four observing modes. Its single-object slitless spectroscopy (SOSS; Albert et al., 2023) mode provides medium-resolution spectroscopy (R$\sim$700) between 0.6 and 2.8 µm and is specifically designed to observe transits and eclipses of exoplanets orbiting relatively bright (J $>$ 6.3) host stars. The wide field slitless spectroscopy (WFSS; Willott et al., 2022) mode enables low-resolution (R$\sim$150) slitless spectroscopy between 0.8 and 2.2 µm. Due to its large field of view, this mode is ideal for detecting faint high-redshift galaxies. The Aperture Masking Interferometry (AMI; Sivaramakrishnan et al., 2012, 2023) mode combines a non-redundant mask with the imager to achieve high-contrast imaging optimised to detect point sources such as circumstellar environments or AGNs. Finally, NIRISS includes standard imaging capabilities with broadband and narrowband filters primarily used to complement NIRCam imaging and provide redundancy.

2.4 The Mid-Infrared Instrument (MIRI)

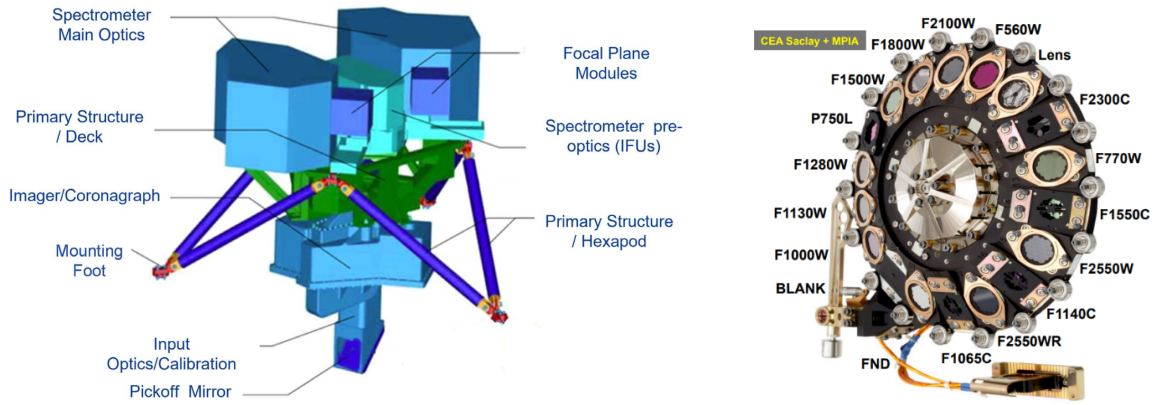

Figure 2.4: MIRI instrument setup (left) and MIRI filter wheel showing its 18 filters and mask elements that can be rotated into the science path (right). Images taken from G. S. Wright et al. (2023) and G. S. Wright et al. (2015), respectively.

2.4.1 Motivation

Since the 1960s, infrared astronomy has seen remarkable progress, particularly in the near-infrared, where detector sensitivity has improved by a factor of ∼10,000 and instruments now employ arrays approaching 100 million pixels. By contrast, advances in the mid-infrared have been much more modest, with sensitivity improving only by about a factor of 30, which was largely due to larger telescope apertures. Furthermore, detector arrays have rarely exceeded 100,000 pixels and are thus far smaller than their near-infrared counterparts. This disparity arises because the intense thermal background from the atmosphere and from ground-based telescopes themselves severely limits mid-infrared observations, effectively blinding instruments and constraining detector development. As a result, major facilities have often lacked general-purpose mid-infrared instruments, making progress in this wavelength regime heavily dependent on cooled space telescopes such as IRAS, ISO, Spitzer, Akari, and WISE, which have demonstrated the transformative gains achievable when thermal emission is eliminated, but suffered from poor resolution due to their small aperture sizes. MIRI is the culmination of decades of development (G. H. Rieke et al., 2015), and achieves unprecedented sensitivity and resolution in the mid-infrared. These gains are primarily attributable to the combination of JWST's large ∼25 m^2 collecting area and its cold 40 K operating environment. Compared to ground-based facilities, the absence of atmospheric absorption and thermal emission makes MIRI more than competitive even with the next generation of 30–40 m class telescopes, opening new windows for the study of dust, star formation, and galaxy evolution across cosmic time (Glasse et al., 2015).

2.4.2 Imaging and Coronography

The Mid-Infrared Instrument (MIRI; G. H. Rieke et al., 2015; G. S. Wright et al., 2015, 2023) is the only JWST instrument capable of operating at wavelengths longer than 5 microns and includes a broad range of science functions. Its standard imaging mode consists of nine broadband filters in the 5-27 μm range and covers a field of view of approximately 1.4×1.9 $arcmin^2$. Besides the standard imager, MIRI's imaging channel also includes four coronographs (Boccaletti et al., 2015), which are designed for observations at 10.65 μm, 11.40 μm, 15.50 μm, and ∼23 μm. The MIRI imager field of view is shown on the left-hand side of Figure 2.5, while the right-hand side illustrates the locations of the three 4-quadrant phase mask (4QPM) coronagraphs. The coronographs (including the Lyot coronagraphic mask region labelled `"MASKLYOT"` at the top) are positioned to the left of the imager's rectangular field of view and are marked as `"MASK1***"`. The Lyot coronagraph region is important for MIRI imaging because it shares the same optical path as the main imager (aside from the Lyot stop), allowing it to be calibrated and analysed like the standard imaging area. In contrast, the 4QPM coronagraphs include additional optics that require separate calibrations. Consequently, official JWST pipeline mosaics (level 3 "`*i2d.fits`" files) include both the imager and Lyot regions, while the 4QPM regions are masked. While providing additional data, these extra exposures can lead to complications in the analysis of large mosaics due to uneven background noise levels (see Section 2.4.5). The resulting MIRI images are diffraction-limited at all wavelengths, with a full width at half maximum of

$0.035 \times \lambda(\mu m)$ arcseconds (G. H. Rieke et al., 2015).

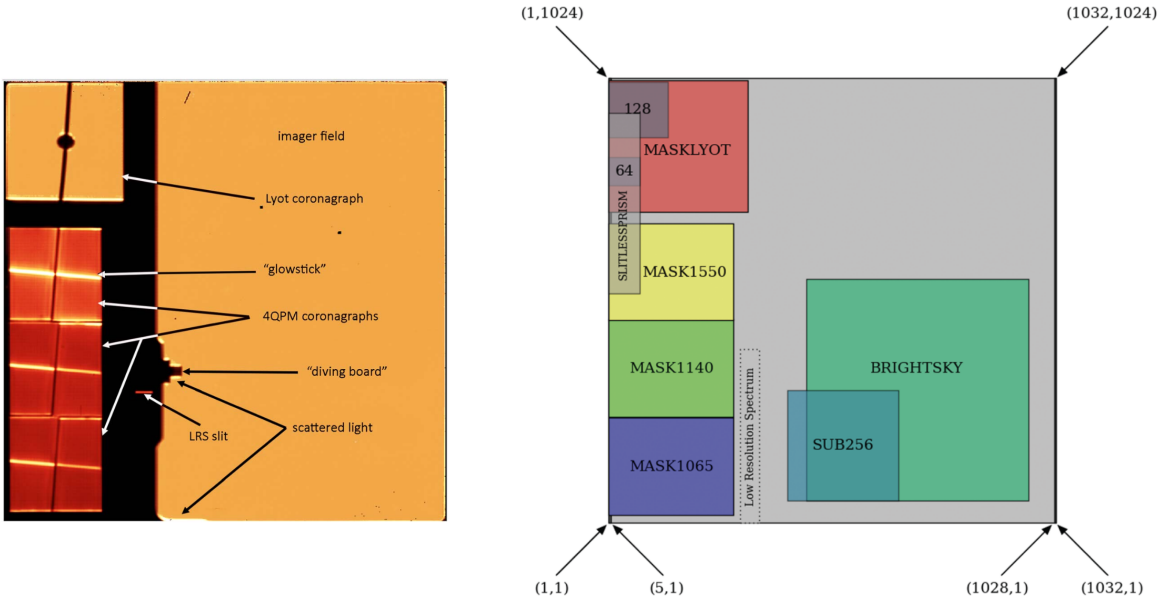

Figure 2.5: Layout of the MIRI imager field of view (left) and the relative positioning of the sub-arrays (right). Highlighted regions on the left mark areas affected by observatory scattered light in the F2550W filter, including the "diving board," the bottom detector rows, and the coronagraph locations. Images are taken from G. S. Wright et al. (2023) and Ressler et al. (2015), respectively.

2.4.3 Spectroscopy

MIRI's low-resolution spectroscopy (LRS) mode (Kendrew et al., 2015) can be operated either in a long-slit configuration, using a fixed slit mask in the field of view, or in a slitless configuration anywhere within the imager's field by selecting the double-prism assembly in the filter wheel. Note that the location of the LRS sub-array on MIRI's field of view is shown on the right panel in Figure 2.5. It covers a wavelength range of 5-12 μm and provides a spectral resolution of R∼100. Lastly, Medium resolution spectroscopy (MRS; M. Wells et al., 2015 employs an integral field spectrograph and covers the full range of 5 to 28 μm, while achieving a spectral resolution of R∼3300 and R∼1300 at the shortest and longest wavelengths, respectively.

2.4.4 Sensitivity and Background Noise

Throughout the entirety of its operating wavelength range, the sensitivity of MIRI imaging is fundamentally limited by background emission from both astronomical and instrumental sources. At wavelengths shorter than ∼12.5 μm, the dominant contributions come from zodiacal light and Galactic dust. At longer wavelengths, the background is increasingly dominated by thermal emission from the observatory itself, due to its unbaffled design and finite operating temperature, which is why MIRI needs to be actively cooled to very low temperatures. Figure 2.6 provides a graphical representation of the different contributions to the background detected at the focal plane of JWST, depending on wavelength. Commissioning observations confirmed that the

overall background level behaves as expected, with minor variation between different telescope orientations. An exception is the F770W filter, which showed larger background variation (∼7%) independent of the telescope's orientation. However, these fluctuations were found to be linked to the emission from PAH features at 7.7 microns, rather than instrumental effects (Dicken et al., 2024). Figure 2.7 highlights the dramatic improvement in sensitivity and angular resolution achieved by MIRI compared to IRAC on Spitzer, whilst Figure 2.8 provides a quantitative comparison between the limiting flux densities of the imaging modes of JWST, Hubble, Gemini, and Spitzer.

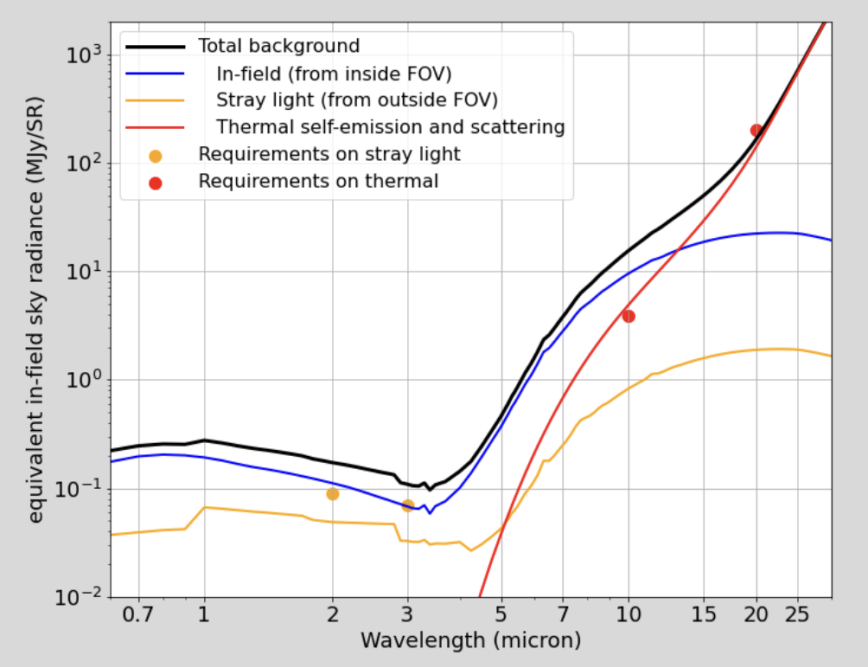

Figure 2.6: Contribution to the overall background noise for JWST (black curve), given in equivalent units of uniform sky radiance (MJy/sr) at its focal plane. Curves are adjusted to match commissioning measurements of the benchmark field J2000. The field was selected due to its zodiacal emission that lies 20% above the celestial minimum, while also being strongly affected by stray light. Figure taken from the JWST User Documentation.

2.4.5 Known Issues with MIRI

While MIRI provides unprecedented sensitivity, several known issues affect its data: Background variations, residual flat-fielding errors, and instrumental artefacts can introduce spatial gradients and bad pixels into its images. Fortunately, there are several best practices available to mitigate this effect, the most prominent being *dithering* and additional background observations (see Dicken et al. (2024) and also below). Nonetheless, careful data reduction and calibration remain a necessity when working with MIRI images, especially in the reddest filters where the thermal background emission is most pronounced.

In the following, I will briefly describe the most prominent issues with MIRI and recommended mitigation strategies. A detailed discussion can be found in Dicken et al. (2024) and Rigby et al. (2023), as well as the JWST User Documentation[1].

[1] https://jwst-docs.stsci.edu

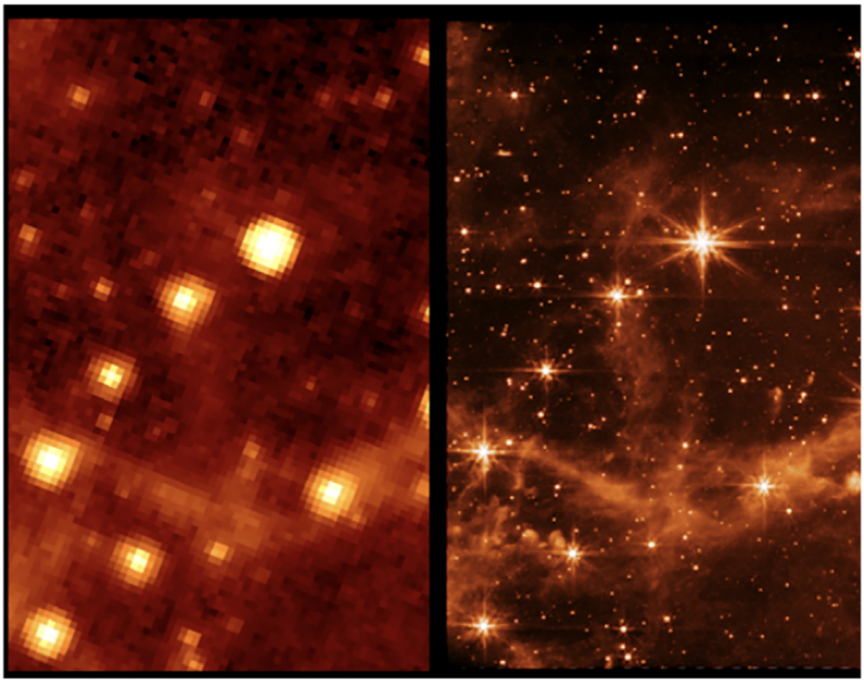

Figure 2.7: Comparison of the same field of view imaged by IRAC on Spitzer at 7.8 µm (left) and MIRI at 7.7 µm (right). The field of view is approximately 70"×111" in size. Image taken from G. S. Wright et al. (2023), courtesy of András Gáspár.

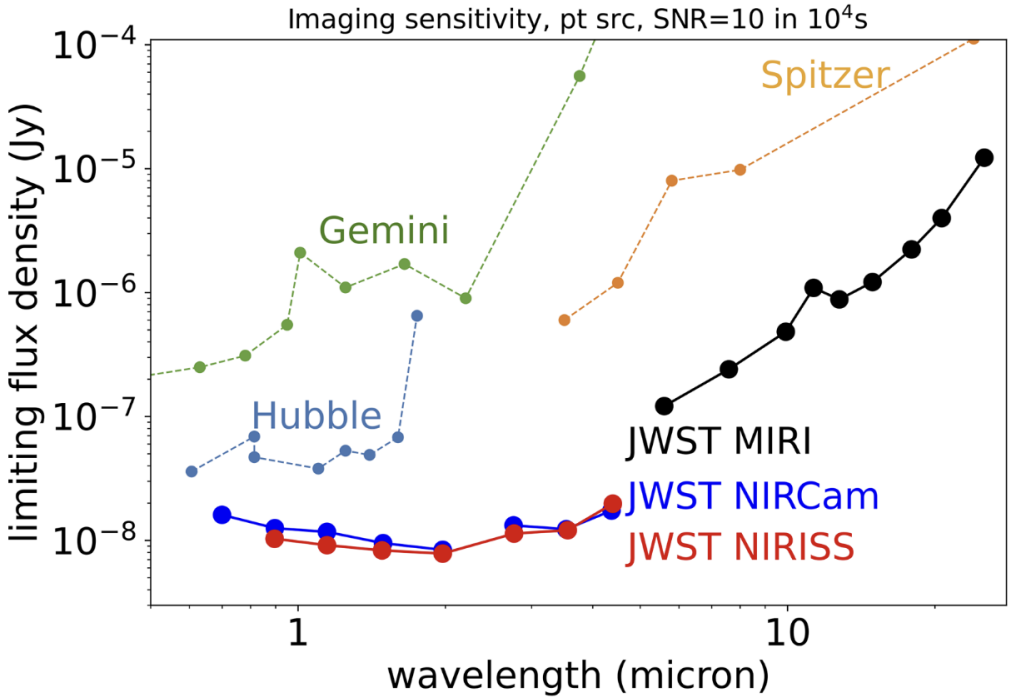

Figure 2.8: Imaging sensitivity of JWST compared to other observatories. The Y-axis shows the faintest point source detectable at S/N = 10 in 10 ks, in Janskies, while the X-axis shows wavelength in microns. JWST instruments (NIRISS, NIRCam, MIRI) are shown with solid lines, whilst Hubble, Gemini, and Spitzer are represented by dashed lines. Sensitivities are calculated using `Pandeia v2.0` and reflect on-orbit performance. Figure taken from Rigby et al. (2023).

Scars, Bad Pixels and Edge Brightening

A common feature in MIRI images is the so-called *imager scar*, a diagonal mark on the top-left portion of the detector (centred at pixel 428, 987, extending over 16 pixels), resulting from a scratch on the detector surface. While these pixels remain responsive, light falling on them can scatter perpendicular to the scratch. Under uniform illumination, this produces faint diagonal stripes parallel to the scar, whose brightness, position, and width vary with wavelength. Bright sources imaged on these pixels show a distorted profile, with scattered light extending perpendicular to the scar, differing from the typical point-source profile elsewhere on the imager.

The detector also contains bad pixels identified during ground testing and in-flight observations. These are flagged as "`DO_NOT_USE`" in the flight bad pixel mask and are automatically ignored by the JWST pipeline. Two columns (385 and 386) are shorted and similarly flagged. Another feature is the *knife edge* structure, which represents a protrusion on the left side of the detector that is used for optical testing and blocks a small portion of the field of view. Although this effect primarily affects mosaics, its impact can be mitigated by adhering to the standard 10% overlap in imaging mosaics. Lastly, *edge brightening* is observed on the left and bottom edges of the imaging FOV, caused by stray light within the instrument. While present in individual exposures, these effects are generally mitigated in combined dithered or mosaicked images. Ongoing analyses continue to characterise these features and refine calibration strategies.

Persistence

Persistence refers to a "memory effect" in which a residual signal from a previous exposure remains on the detector and appears in subsequent images. Persistent images are a well-known artefact of cooled infrared detectors and were already encountered in earlier infrared space missions, such as Spitzer and WISE, which used detector technology similar to MIRI (Hora et al., 2004; E. L. Wright et al., 2010). In these missions, persistence was mitigated using annealing, a procedure in which the detectors are briefly heated by approximately 15 K to release trapped charge in the focal plane. Ground testing indicated that MIRI detectors could also show persistence under certain conditions, so an annealing system was incorporated to remove residual artefacts if needed. During commissioning, MIRI's persistence behaviour was specifically investigated to confirm that any memory effects were consistent with ground test expectations. Figure 2.9 shows an example of a persistence artefact consisting of black vertical and horizontal lines, which originated from the dispersed spectrum of a bright star.

Bonus Lyot Imaging

As mentioned in Section 2.4.2, the Lyot imaging field of view provides valid, calibrated data except for the area of the support structure, which blocks the light from reaching the detector. Since many observations image adjacent areas on the sky plane, this can result in additional exposures of the mosaic where there is overlap with the Lyot mask.

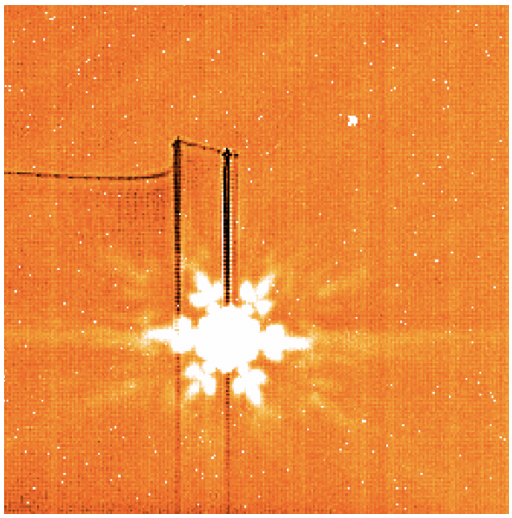

Figure 2.9: Image of observation 4 in programme 6122 showing a persistence artefact (vertical dark lines and horizontal trail off the left-hand side) from a previous observation using the slitless prism to obtain a spectrum of a bright star.

As a consequence, several past observations showed differences in flux levels in the Lyot compared to the rest of the imager. While these offsets are usually modest, in those cases where there is overlap, they are typically visible by eye and require special care when performing photometry on sources in the neighbouring detector area.

2.4.6 Imaging Recommended Strategies

In order to obtain the best possible data quality with the MIRI imager, a number of observing strategies are recommended to mitigate instrumental effects. One such strategy is called *Dithering* and describes multiple exposures of the same target, which are all slightly offset with respect to each other. Dithering is particularly important, as it improves the sampling of the point spread function at shorter wavelengths, helps suppress the impact of bad pixels and detector defects, and allows for more reliable background subtraction in the case of compact sources. It also protects against the effects of cosmic ray showers, which can leave extended residuals in the detector. Patterns with relatively large steps between dither positions are most effective, which is why the 4-point `"CYCLING-LARGE"` pattern is now adopted as the standard choice. At least four dither positions are generally advised to ensure sufficient redundancy in mosaics. Persistence effects, which are most relevant at longer wavelengths due to the higher telescope background, can be minimised by ordering filters from short to long wavelengths within a given sequence. Background subtraction strategies depend on the source: while small targets may allow the background to be estimated from the dithered science frames themselves, extended sources typically require separate background observations. In those cases, background fields should be placed close to the science target, dithered to allow contaminating sources to be removed in stacking, and observed with exposure times matched to the science integrations to avoid introducing additional noise. Together, these practices provide an effective means of mitigating the aforementioned artefacts encountered in MIRI imaging and allow for high-quality data reduction. For more detail, see Dicken et al. (2024) and the JWST User Documentation.

Figure 2.10 shows an example observation of the Large Magellanic Cloud in two MIRI filters, showcasing the effectiveness of current mitigation strategies. The left images are produced from "*`cal.fits`" files, at an intermediate stage of the JWST pipeline, and are clearly affected by a variety of image artefacts. Instead, the right-hand side shows the final mosaicked images, where almost no traces of bad pixels are visible and the background emission is significantly reduced in the F560W band.

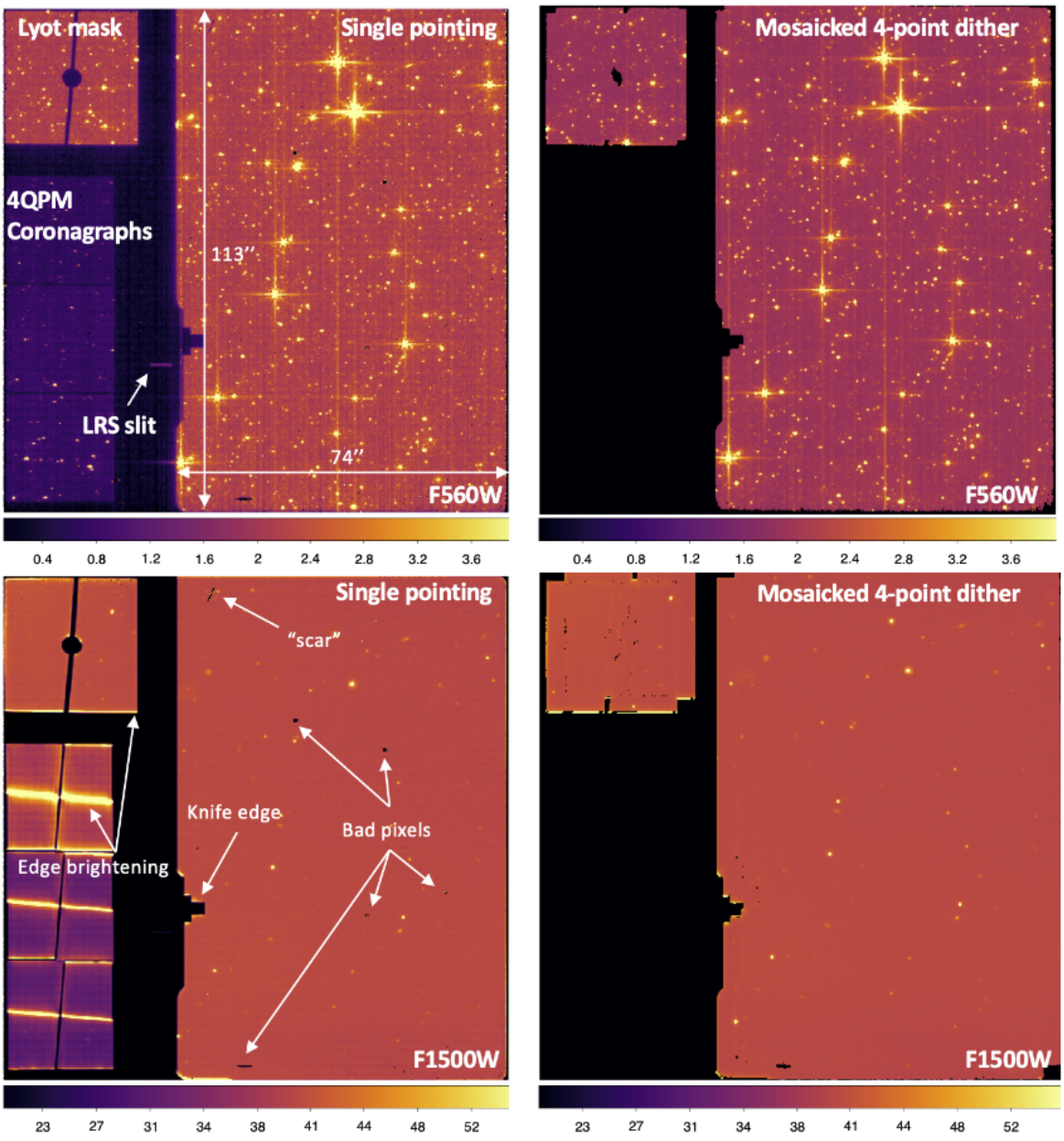

Figure 2.10: MIRI imaging at 5.6 µm (top) and 15.0 µm (bottom) of the Large Magellanic Cloud, obtained from JWST commissioning program 1024 (observations 5 and 9). The left panels show single-exposure, stage-2 calibrated (cal) FITS files, which are unrectified and flat-fielded but not yet combined. The right panels display the corresponding mosaicked images created from four dithered exposures and processed to pipeline level 3a. The colour bars show the surface brightness in units of MJy/sr. Image taken from Dicken et al. (2024).

Chapter 3

Data

This chapter introduces the data used throughout this project and provides the necessary background for the following chapters. I begin by describing the Blue Jay survey and the corresponding sample of galaxies on which this work is based. I then provide an overview of the three large JWST imaging programmes in the COSMOS field (PRIMER, COSMOS-Web, and COSMOS-3D), where the MIRI data are taken from, summarising their scientific aims and observing strategies. The chapter concludes with an introduction to the FITS file format and the World Coordinate System (WCS).

3.1 The Blue Jay Survey

The galaxies studied in this work were taken from the Blue Jay survey (GO 1810; Belli et al., 2025), a medium-sized JWST Cycle 1 programme designed to investigate the interstellar medium and stellar populations of galaxies at cosmic noon. The survey obtained deep multi-object spectroscopy of 153 galaxies with two NIRSpec micro-shutter assembly (MSA) pointings in the COSMOS field. In particular, three medium-resolution NIRSpec gratings (G140M, G235M, G395M) were employed to obtain spectra in the 1-5μm range. Figure 3.1 shows two examples of Blue Jay spectra of a massive quiescent galaxy (ID 9395; red line) and a low-mass star-forming galaxy (ID 11853; blue line) over the full spectral range.

Simultaneous deep NIRCam imaging was carried out for 41 out of the 153 (27%) Blue Jay sources, using seven broad-band filters (F090W, F115W, F150W, F200W, F277W, F356W, and F444W) and are publicly available[1]. These data are supplemented by multi-band NIRCam observations from the PRIMER survey (GO 1837; see below), as well as multi-band HST imaging taken with ACS (F606W and F814W) and WFC3 (F125W, F140W, F160W) in the COSMOS field as part of the CANDELS survey (Grogin et al., 2011; Koekemoer et al., 2011). The resulting Blue Jay data thus includes HST and JWST photometry in 13 bands, covering a wavelength range from 6000 Å to 4.4 μm, which corresponds to a complete coverage from the rest-frame optical/UV to near-IR.

Targets were carefully selected from the 3D-HST photometric catalogue (v4.1.5; Brammer et al., 2012; Momcheva et al., 2016; Skelton et al., 2014) in an effort to achieve

[1] https://archive.stsci.edu/doi/resolve/resolve.html?doi=10.17909/vzzy-4w25

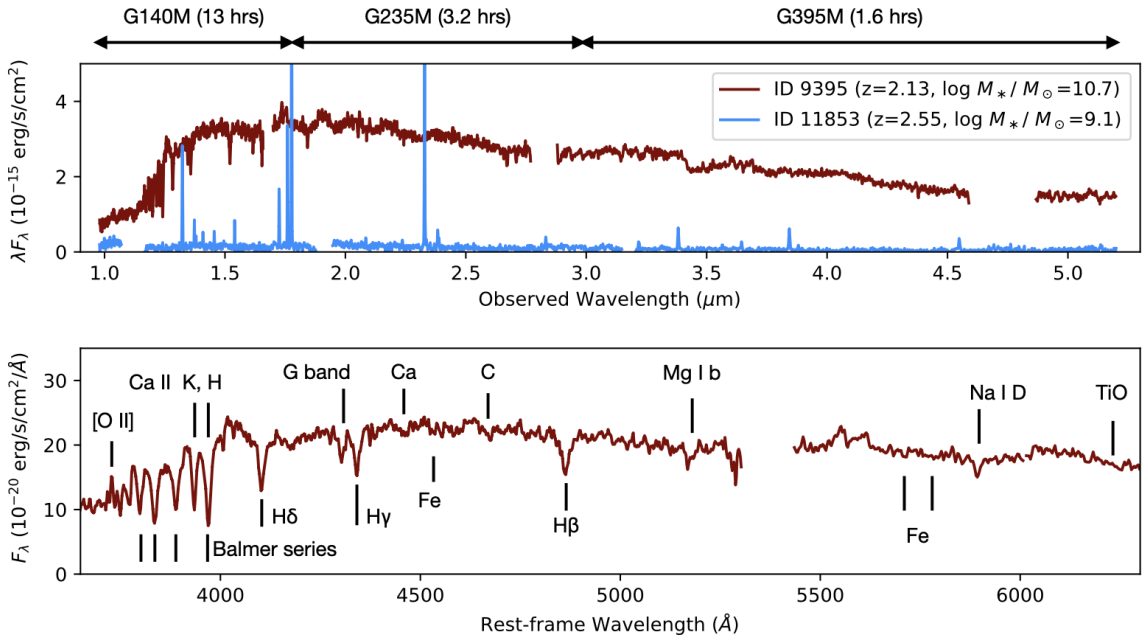

Figure 3.1: Example spectra of the Blue Jay survey for a massive quiescent galaxy (red line) and a low-mass star-forming galaxy (blue line) covering the entire 1-5 µm wavelength range. The wavelength ranges and exposure times of each grating are shown above the top panel. Adapted from Belli et al. (2025).

a uniform distribution in redshifts ($1.7 < z < 3.5$) and stellar masses ($\log(M_*/M_\odot) \gtrsim 9$). This ensures a representative sample of galaxies at cosmic noon, spanning the full z-M_* parameter space without being biased in colour, SFR, or morphology. Figure 3.2 shows the sample on the mass vs. redshift plane, indicating the redshift cutoffs (red dashed lines) and the mass completeness limit (blue solid line). Sources with white circles are lacking spectroscopic redshift measurements.

The complete photometric catalogue is publicly available[2] and its contents are discussed in detail in Belli et al. (2025). In this work, a reduced subset of the 3D-HST parent catalogue, containing the IDs, right ascensions, and declinations of the 153 Blue Jay galaxies, served as a reference for locating objects within the large JWST mosaics and generating cutouts for aperture photometry. The Blue Jay catalogue was used in Chapter 4 to obtain the NIRCam apertures, which were rotated and rescaled to match MIRI images and ensure consistency. Furthermore, Chapters 5 and 6 characterise the properties of the MIRI-imaged Blue Jay sample and use previous Prospector fits to the Blue Jay photometry and spectra to investigate dust energy balance.

3.2 JWST Imaging Surveys

All photometric data used in this work were downloaded from the Mikulski Archive for Space Telescopes (MAST)[3], which provides access to datasets from various telescopes at multiple processing levels. In the following sections, I will provide an overview of the

[2] https://zenodo.org/records/13292819
[3] https://mast.stsci.edu/search/ui/#/jwst

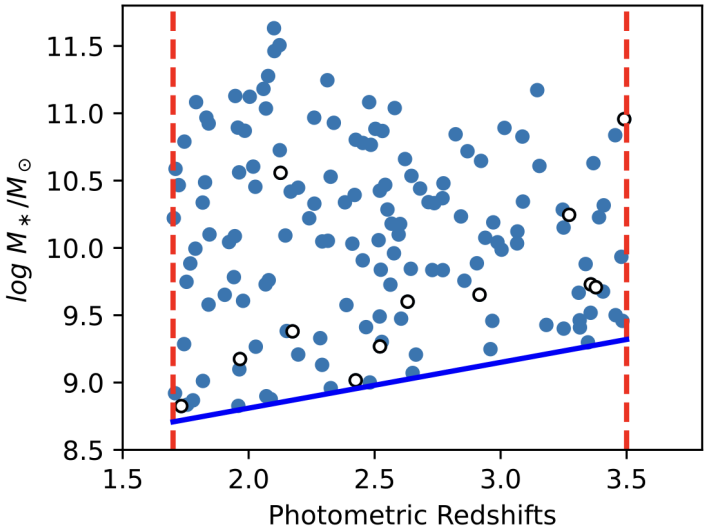

Figure 3.2: Stellar mass vs. redshift for the Blue Jay sample using photometric redshifts. Empty circles represent galaxies without spectroscopic redshift measurements. The limits of the sample selection are indicated by a blue solid line for stellar mass and red dashed lines for redshifts. Taken from Belli et al. (2025).

surveys in the COSMOS field whose MIRI data were processed as part of this project, including their observing strategies and scientific aims.

PRIMER (GO 1837)

The Public Release Imaging for Extragalactic Research (PRIMER; Dunlop et al., 2021) survey is a major JWST Cycle 1 Treasury Programme designed to deliver a large-area, deep, and homogeneous imaging survey using both NIRCam and MIRI. By leveraging JWST's unique near- to mid-infrared capabilities, PRIMER has enabled transformative studies of early galaxy and black hole formation, reaching redshifts up to $z\sim12$, and providing a rich target set for follow-up spectroscopy with instruments such as NIRSpec.

PRIMER targeted the two key equatorial HST CANDELS legacy fields, COSMOS and UDS (Grogin et al., 2011; Koekemoer et al., 2011), which are among the most extensively studied extragalactic deep fields. This choice allows direct comparison with extensive multi-wavelength data, including ALMA observations, enabling comprehensive studies of galaxies across the rest-frame ultraviolet to submillimetre regimes. The survey obtained deep imaging in eight NIRCam (F090W, F115W, F150W, F200W, F277W, F356W, F410M, and F444W) and two MIRI filters (F770W and F1800W), expanding the available high-quality JWST imaging by nearly a factor of 20 relative to other Cycle 1 programmes. Observations were carried out in two epochs, with the telescope rotated 180° between visits, allowing simultaneous use of NIRCam and MIRI to cover different regions of each field (Dunlop et al., 2021). Figure 3.3 shows the layout of the observations with MIRI and NIRCam in the COSMOS field (left) and the UDS field (right).

[4] https://primer-jwst.github.io/observations.html

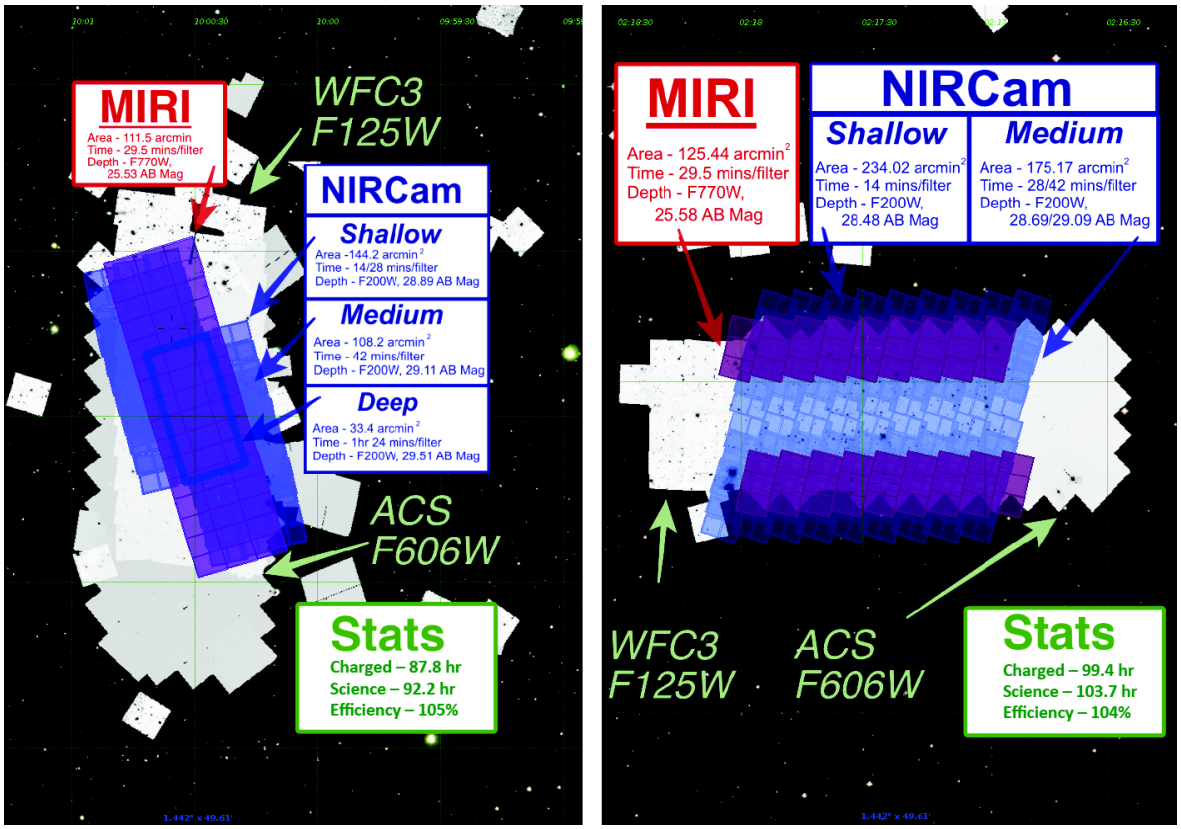

Figure 3.3: Footprint map of the PRIMER observations with MIRI and NIRCam in the COSMOS (left) and the UDS field (right). NIRCam imaging is shown in blue, MIRI coverage in red. Figure taken from the PRIMER home page[4].

COSMOS-Web (GO 1727)

COSMOS-Web (Casey et al., 2023) is a 255-hour wide-field Cycle 1 JWST treasury programme aimed at increasing the large abundance of multiwavelength observations and data products available in the COSMOS field. During the program, a contiguous 0.6 deg^2 area was mapped in four NIRCam filters (F115W, F150W, F277W, and F444W) and a non-contiguous 0.2 deg^2 area was observed with MIRI in parallel, using only the F770W filter. Figure 3.4 shows the pointings of NIRCam and MIRI within the COSMOS field in blue and red, respectively.

The COSMOS-Web survey aimed to provide a comprehensive view of galaxy formation and evolution across cosmic time. Its main scientific goals were to map thousands of galaxies during the epoch of reionisation ($6<z<11$), characterising the UV-luminosity function, stellar mass function, and star-formation histories of galaxies; to trace the assembly of massive galaxies in the first few billion years after the Big Bang, including rare quiescent systems at $z\sim4$; and to link dark matter to visible matter by probing the evolution of the stellar-to-halo mass relation up to $z\sim2.5$, assessing its dependence on galaxy star-formation histories and morphologies through combined NIRCam and MIRI imaging.

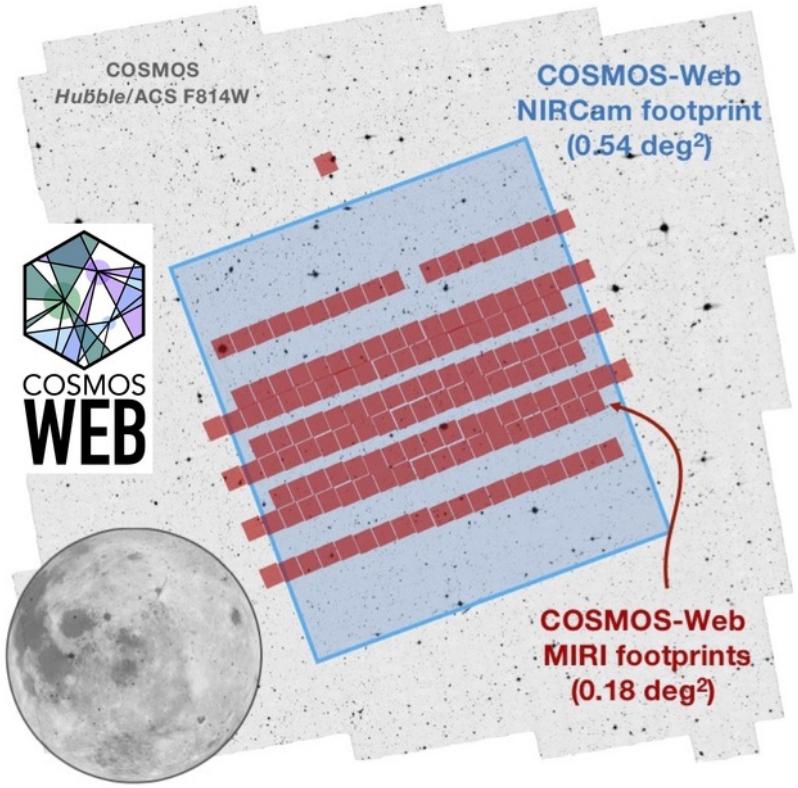

Figure 3.4: Imaging of the COSMOS field during the COSMOS-Web survey. The area mapped by NIRCam is displayed in blue, while MIRI footprints are shown in red. Figure taken from the COSMOS-Web home page[5].

COSMOS-3D (GO 5893)

The COSMOS-3D survey (COSMOS-3D Team, 2023) is a JWST Cycle 3 Large Programme combining NIRCam wide-field slitless spectroscopy (WFSS) in F444W over 0.33 deg^2 with deep parallel MIRI imaging ($\sim$500 arcmin^2). The survey aimed to obtain redshifts for $\sim$20,000 galaxies and $\sim$5,000 AGN, including $>$4,000 galaxies and up to 500 AGN at z$>$5. NIRCam/WFSS observations are complemented by NIRCam imaging in F115W, F200W, and F356W, thus extending the coverage provided by the COSMOS-Web survey. In addition to NIRCam, the programme obtained 484 square arcmin of simultaneous MIRI imaging in F1000W and F2100W, once again complementing the MIRI imaging coverage of the COSMOS-Web and PRIMER survey using F770W and F1800W.

The programme's main scientific goals are to study the emergence of massive galaxies and early supermassive black holes, trace the cosmic web and sources of reionization, and explore the connections between galaxies and the intergalactic medium from reionisation to cosmic noon. The dataset will enable a wide range of extragalactic science, including high-redshift galaxy luminosity functions, dusty galaxy populations, and time-domain studies of supernovae and AGN, with fully reduced spectra and value-added catalogues provided to the community.

[5] https://cosmos.astro.caltech.edu/page/cosmosweb

3.3 FITS Format and World Coordinate System

Astronomical data are commonly stored in Flexible Image Transport System (FITS) files, the standard format endorsed by the International Astronomical Union for storing, archiving, and transmitting scientific data. The system is designed to accommodate both image data and metadata, with a structure composed of a series of Header/Data Units (HDUs). Each HDU contains a human-readable ASCII header and an associated data block, which may be an image, table, or another binary format. The headers provide metadata that allows for the description of the content, structure, and associated physical context of the data. A comprehensive documentation of the FITS file format is provided by the FITS Support Office at NASA/GSFC[6].

In addition to storing image data, FITS also supports the description of world coordinates (Greisen & Calabretta, 2002), physical coordinates that associate each pixel in an N-dimensional array with a point in a physical or abstract parameter space. These coordinates may describe observable quantities like frequency, wavelength, or sky position (e.g., right ascension and declination), as well as abstract parameters such as Stokes polarisation components.

To encode this information, a convention was developed to assign coordinate metadata to each axis. This includes the value of the coordinate at a reference pixel (`"CRVALn"`), the location of the pixel referring to that reference point (`"CRPIXn"`), the increment of the coordinate (`"CDELTn"`), the axis type (`"CTYPEn"`), and optionally a rotation parameter (`"CROTAn"`). This approach allows for flexible and precise descriptions of the spatial, spectral, or temporal structure of the data, even in cases where the reference point lies outside the image or does not correspond to an integer pixel. The FITS World Coordinate System (WCS) standard has since evolved to allow more complex and accurate coordinate representations.

The development of the FITS World Coordinate System (WCS) standard has been incremental. The original FITS specification by D. C. Wells and Greisen (1979) defined a simple coordinate labelling system using the now-familiar keywords `CRPIXn`, `CRVALn`, `CDELTn`, `CROTAn`, and `CTYPEn`. This framework was significantly expanded in the first dedicated WCS paper by Greisen and Calabretta (2002), which formalised the interpretation of these keywords and introduced new ones to more completely describe coordinate transformations. A companion paper by Calabretta and Greisen (2002) addressed spherical projections, providing a rigorous treatment of celestial coordinate mapping. Later, Thompson (2006) extended the WCS system for use with solar images and incorporated keywords to encode ephemeris information. Together, these developments established the flexible system that underpins virtually all astronomical imaging today.

The FITS Standard[7] defines the full set of required header keywords, the formats of extensions, rules for image and table structures, and the WCS conventions employed in modern astronomical data.

[6] https://fits.gsfc.nasa.gov/fits_home.html
[7] https://fits.gsfc.nasa.gov/standard40/fits_standard40aa-le.pdf

The conversion from pixel to world coordinates is performed in multiple steps, which are outlined in Figure 3.5. First, a linear transformation is applied via matrix multiplication of the pixel coordinate vector (`PCi_j` or `CDi_j`), followed by an optional scaling step depending on the chosen formalism. Finally, a non-linear transformation produces the world coordinates. A more detailed treatment of this procedure is provided in Section 4.2.3, where the rotation of individual cutouts is discussed.

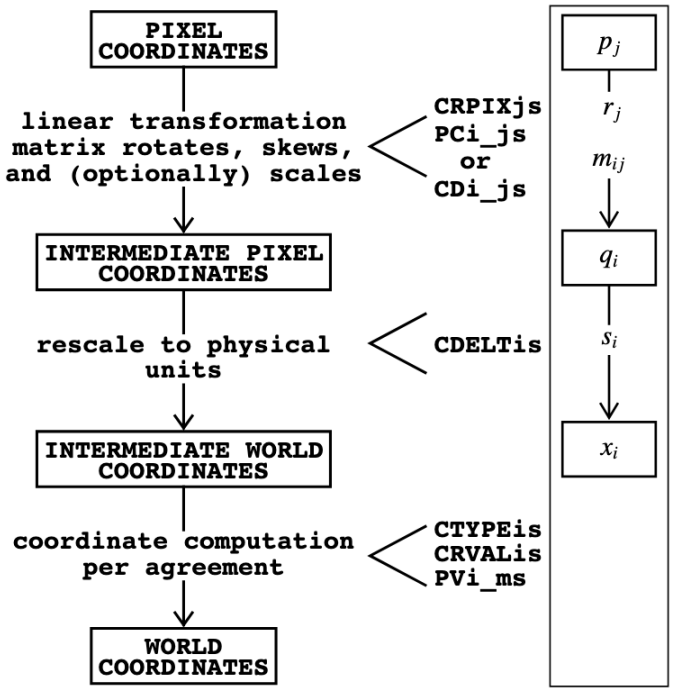

Figure 3.5: Schematic overview of the conversion between pixel and world coordinates as a multi-step process. Adapted from Greisen and Calabretta (2002).

3.4 JWST Calibration Pipeline Products

All JWST observations are processed through a unified JWST Calibration Pipeline (Bushouse et al., 2025), which ensures consistent treatment of data across all instruments and observing modes. Unlike previous missions such as HST, which maintained multiple instrument-specific pipelines, JWST employs a modular system where common steps (e.g., detector-level corrections) are applied in the same way across instruments, while specialised routines handle differences between imaging and spectroscopy. The pipeline relies on a library of calibration reference files maintained through the Calibration Reference Data System (CRDS; Greenfield and Miller (2016)), which is updated regularly; whenever new pipeline builds or reference files are released, the entire archive is reprocessed to guarantee uniformity.

The pipeline is organised into three main stages: In Stage 1, raw detector readouts ("*`uncal.fits`") are corrected for instrumental signatures such as dark current, bad pixels, cosmic-ray hits, and detector non-linearity, producing count-rate images. Stage

2 applies photometric and astrometric calibrations, flat-field corrections, and wavelength solutions, resulting in calibrated exposure-level products ("*`cal.fits`") still on the detector's native pixel grid. Finally, Stage 3 combines multiple calibrated exposures into science-ready data products: mosaicked images for imaging modes ("*`i2d.fits`"), resampled IFU data cubes for integral field spectroscopy, and extracted one-dimensional spectra for slit and multi-object spectroscopy. Specialised stage 3 pipelines also exist for coronagraphy, aperture masking interferometry, and time-series observations. Table 3.1 contains a summary of the different product levels available at different stages of the pipeline. For more detail, see the JWST User Documentation[8].

Product Level	Description
1b	Uncalibrated raw data in FITS format
2a	Countrate exposure
2b	Calibrated exposure (flux calibration, instrumental corrections)
2c	Calibrated exposure with cosmic ray flags applied
3	Combined data products (e.g., mosaics or co-added exposures)

Table 3.1: Summary of JWST data product levels and their content.

In this thesis, I exclusively worked with level-3 data products in the calibrated mosaic format "*`i2d.fits`". As outlined in Pence et al. (2010), astronomical FITS files are composed of multiple Header and Data Units (HDUs), each serving a specific role in declaring and storing the data. The `"PRIMARY"` HDU begins with the first FITS block of the file. Its header contains global information about the file contents, key metadata from the observation, and the World Coordinate System (WCS). Although the `"PRIMARY"` unit can also store a data array, it is often left empty.

The most relevant extensions for this analysis are the `"SCI"` (Science Image) and `"ERR"` (Error Image) arrays. The `"SCI"` extension contains the fully calibrated science data, typically expressed in surface brightness units (e.g., MJy/sr) or flux density in JWST products. These level-3 mosaics result from multiple calibration steps, including flat-fielding, dark-current subtraction, and cosmic-ray rejection. The `"ERR"` extension stores the 1σ uncertainty for each pixel in the `"SCI"` image, combining contributions from photon noise, detector readout noise, and other systematic calibration uncertainties. This uncertainty budget is essential for propagating errors in flux measurements and background estimates.

For resampled two-dimensional products, JWST employs a standardised FITS structure that extends beyond these two core arrays. The three-dimensional context image (`"CON"`) encodes which input exposures contributed to each output pixel, while the weight map (`"WHT"`) encodes their relative importance. Variance extensions propagate different noise sources through the resampling: `"VAR_POISSON"` (photon statistics), `"VAR_RNOISE"` (detector read-out noise), and `"VAR_FLAT"` (flat-fielding uncertainties). When multiple exposures are combined, the `"HDRTAB"` table records metadata from all inputs to ensure reproducibility, and the `"ASDF"` extension stores the pipeline's internal

[8] https://jwst-docs.stsci.edu/jwst-science-calibration-pipeline

data model. Together, these extensions provide a complete description of the resampled data, its noise budget, and the provenance of the final mosaic. An example layout of a PRIMER FITS file is shown in Table 3.2.

#	Name	Ver	Type	Dimensions	Format
0	PRIMARY	1	PrimaryHDU	()	–
1	SCI	1	ImageHDU	(5728, 5111)	float32
2	ERR	1	ImageHDU	(5728, 5111)	float32
3	CON	1	ImageHDU	(5728, 5111, 4)	int32
4	WHT	1	ImageHDU	(5728, 5111)	float32
5	VAR_POISSON	1	ImageHDU	(5728, 5111)	float32
6	VAR_RNOISE	1	ImageHDU	(5728, 5111)	float32
7	VAR_FLAT	1	ImageHDU	(5728, 5111)	float32
8	HDRTAB	1	BinTableHDU	96 rows × 244 cols	mixed
9	ASDF	1	BinTableHDU	1 row × 1 col	[28330B]

Table 3.2: List of FITS file extensions and their properties of an example file of the PRIMER survey.

Chapter 4

Photometric Measurements with MIRI

This section discusses the photometric workflow implemented to obtain precision photometry with MIRI. It describes the individual steps of the pipeline in great detail, starting from astrometric alignment, to the creation of RGB composite images, background modelling and aperture photometry, and finally the creation of the final photometric table. All of these steps were carried out using a custom-built Python package called `miri_utils`, which was developed during the course of this work and is publicly available as part of the `red_cardinal` repository on GitHub[1]. A description of the library is provided in Section 4.7.

4.1 Data Preparation

4.1.1 Production of the Cutouts

The first step after downloading the data is to produce square-shaped cutouts centred on galaxies of interest using functions native to `cutout_tools.py`. To extract individual galaxies from the tiles, I used the reduced parent catalogue of the Blue Jay sample described in 3.1 to loop through all Blue Jay galaxy IDs and obtain their Right Ascensions (RA) and Declinations (Dec) in the COSMOS field. The function then inspects all available mosaic images from the PRIMER, COSMOS-Web and COSMOS-3D surveys to find observations of the galaxy. Since MIRI pixels are about 3.5 times as big as NIRCam pixels, a large cutout size of approximately 8×8 arcseconds was chosen to ensure proper statistics of the background fluxes in each frame. A cutout was produced for a galaxy if at least 60% of the cutout consisted of valid data, so that cutouts where more NaN values were present were immediately discarded. The remaining cutouts were stored in the original FITS format preserving all HDU extensions of the original mosaic file, together with a PNG file for preliminary visual inspection.

[1] https://github.com/benjaminpcollins/red_cardinal/tree/main/miri_utils

4.1.2 Astrometric Alignment

Upon initial creation of the cutouts, galaxies generally appear slightly offset from the centre of the images. This offset arises from discrepancies in the reference pixels of the World Coordinate System (WCS) in the original FITS files due to imperfect astrometric calibration among instruments on the ISIM. To ensure consistent measurements between the two instruments it is therefore necessary to correct the MIRI cutouts for this spurious shift in sky positions.

We determine the astrometric offsets by looping through each galaxy ID and loading the MIRI cutout in the bluest band available (typically F770W), together with the corresponding NIRCam/F444W cutout. For each galaxy, we compute the centroids of the NIRCam and MIRI cutouts by fitting a 2D quadratic polynomial to the data using the `centroid_quadratic` function from the `photutils` library. The centroid coordinates are then mapped to celestial sky positions using the respective WCS pixel-to-world transformations of each cutout. Lastly, the astrometric offset is computed as the difference between the two points in the sky.

As already mentioned in Section 3.2, the second observing run of each survey is usually carried out with a rotation of the instrument by 180°. To take care of the different orientations of the resulting FITS files, the PRIMER dataset was split into PRIMER 003 and PRIMER 004, according to the observation numbers within the survey, while COSMOS-Web and COSMOS-3D were each divided into subsets 1 and 2. In this way, the astrometric offset can be computed more easily by just taking into account images with the same orientation on the sky.

An example of a centroid computation is shown in Figure 4.1. A clear misalignment can be seen between the red cross, which marks the central position of the source in the NIRCam F444W frame, and the red dot showing the position of the galaxy in the MIRI F770W cutout. Notice also the rotation between the two images, as can be seen in the second source, which is not at the same position in both cutouts. Indeed, this was a major motivation behind first mapping the pixels to sky coordinates and then calculating the offset, instead of using the inverse approach. Sky coordinates are physical positions in the sky and are not influenced by the orientation of our instruments; hence, this order allowed a robust offset calculation without having to consider the rotation angle of all FITS files at each centroid computation.

Astrometric offsets were calculated using those MIRI bands closest in wavelength to the NIRCam F444W filter. This approach minimises additional uncertainties in the centroid computation due to the much larger point spread function (PSF) at longer wavelengths. However, tests were carried out to ensure that the misalignments obtained with other MIRI filters yield consistent results. Furthermore, all cutouts were visually inspected to ensure that the centroid locations are correct and to discard data from cutouts in which the galaxy was not detected, and hence the algorithm produced inconsistent results. After the mosaics are shifted into place, the cutout routine is applied again, this time yielding cutouts where galaxies are centred.

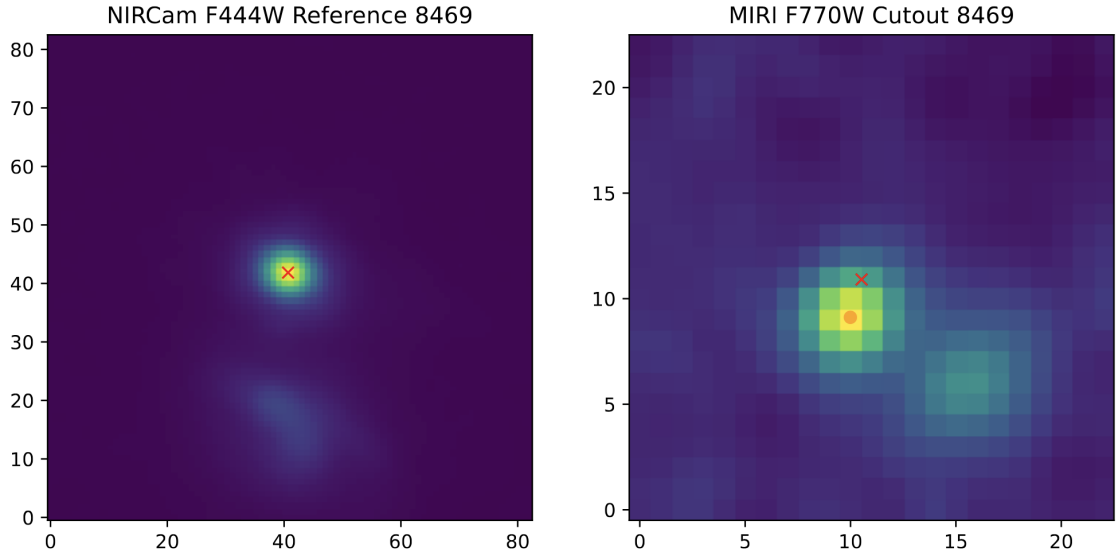

Figure 4.1: Example of the centroid computation in the NIRCam F444W cutout (left) and the MIRI F770W cutout (right) of galaxy 8469. The red cross marks the position of the brightest pixel in the NIRCam image and is superimposed on the MIRI frame on the right.

Figure 4.2 shows the final astrometric offsets as measured for sources mapped in different pointings among the surveys analysed in this work. The circles indicate offset measurements between the NIRCam/F444W and MIRI/F770W filters, whereas the squares correspond to NIRCam/F444W and MIRI/F1000W bands. The systematic clustering of offsets by survey pointing demonstrates the coherent nature of the astrometric differences, with PRIMER 003, COSMOS-Web 2, and COSMOS-3D 1 showing offsets toward the upper-left quadrant (∼225°), PRIMER 004, COSMOS-Web 1, and COSMOS-3D 2 toward the right (∼0°). This coherence in the data is explained by the two major observing windows of the COSMOS field, which are spaced roughly six months apart. Since the orientation of JWST and its instruments is constrained by its position with respect to the sun (see Section 2.2.2), surveys observing in the same annual window tend to show similar offsets. Additionally, we carry out astrometric offset computations using the F1800W and F2100W bands showing close agreement with the bluer filters, thus ensuring consistency among all bands. The final astrometric offsets used to shift the mosaics are displayed in Table 4.1.

4.2 Image Products and Visualisation

4.2.1 Motivation

When analysing large imaging programmes, as is the case for the observations discussed in this thesis, the cutout production routine can yield hundreds of single-filter images of galaxies. A convenient way to combine these data for a first visual inspection is to create RGB-composite images. Since each filter probes a different wavelength range, it is sensitive to a different feature of the infrared emission of the galaxy. Depending on the redshift, the shorter wavelength filters generally probe the stellar continuum, whilst longer wavelengths are increasingly sensitive to the emission of dust and polycyclic

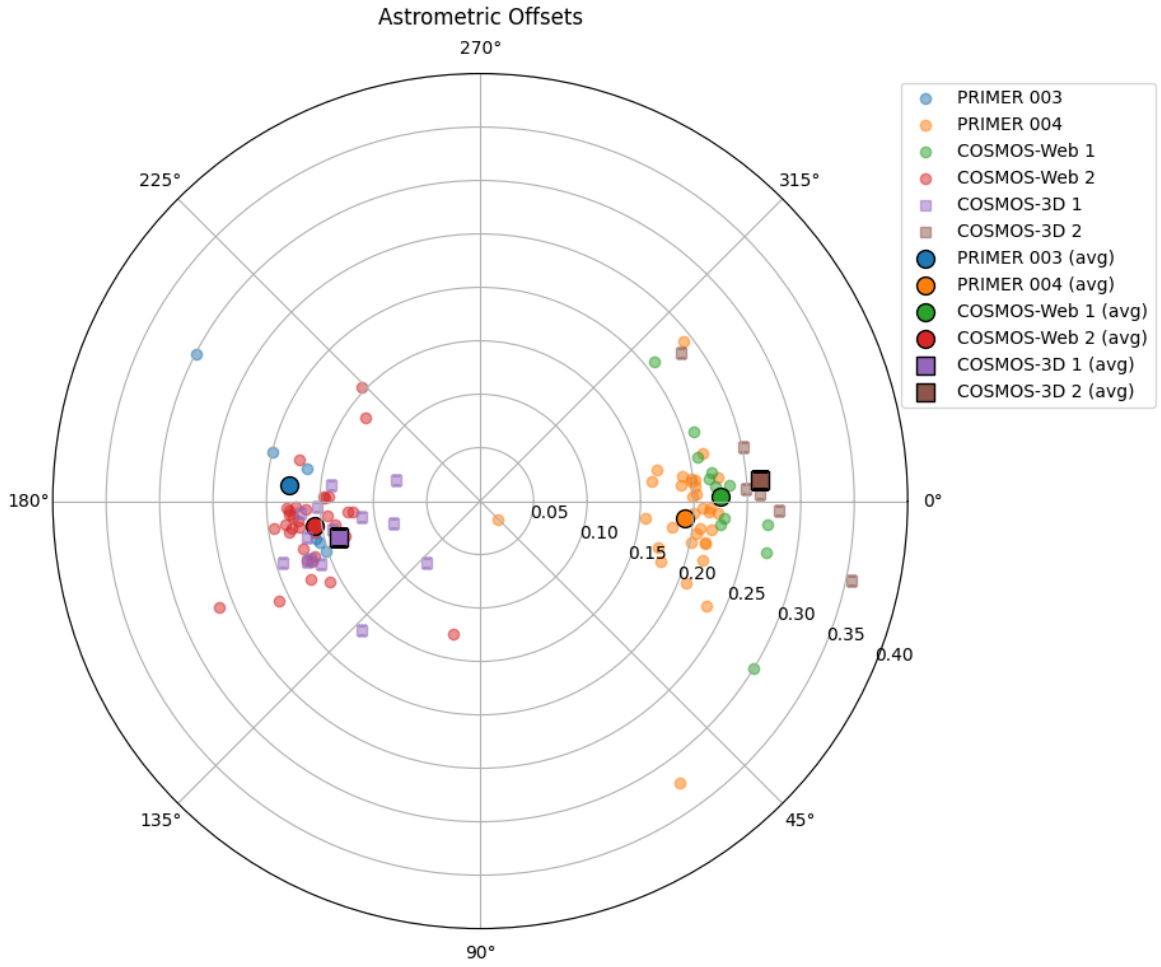

Figure 4.2: Polar representation of astrometric offsets between NIRCam F444W and MIRI filters across different survey pointings. Each point represents the measured offset for an individual galaxy, with the radial distance indicating the offset magnitude (in arcseconds) and the angular position showing the direction of the MIRI centroid relative to the NIRCam centroid in RA (offset to the right) and Dec (towards the top). Circles denote F444W–F770W comparisons, while squares represent F444W–F1000W comparisons.

aromatic hydrocarbons (PAHs). Thus, a multi-wavelength visualisation can provide useful information about the galaxy morphology and the presence of dust and even show traces of star-forming activity. Additionally, RGB composites are also valuable for quality control, as they help to identify potential issues such as misalignments or inconsistencies in the data reduction process that may not be apparent in individual filter images.

4.2.2 Filter-Chanel Mapping

RGB images are constructed by combining three images of a galaxy that were taken at different wavelengths and overlaying them on top of each other. By mapping each band to one of the three colour channels, a composite colour image is obtained from the originally monochromatic filter images. A common approach is to assign the shortest

Survey	**Filter**	**Pointing**	$\langle\Delta\alpha\rangle$ [arcsec]	$\sigma_{\Delta\alpha}$ [arcsec]	$\langle\Delta\delta\rangle$ [arcsec]	$\sigma_{\Delta\delta}$ [arcsec]
PRIMER	F770W	003	−0.178	0.046	−0.015	0.071
	F770W	004	+0.191	0.036	+0.015	0.062
	F1800W	003	−0.161	0.023	+0.019	0.043
	F1800W	004	+0.192	0.037	+0.012	0.033
COSMOS-Web	F770W	1	+0.225	0.030	−0.004	0.069
	F770W	2	−0.155	0.036	+0.023	0.044
COSMOS-3D	F1000W	1	−0.132	0.040	+0.034	0.037
	F1000W	2	+0.262	0.047	−0.020	0.065
	F2100W	1	−0.090	0.039	+0.052	0.022
	F2100W	2	+0.221	0.010	+0.002	0.041

Table 4.1: Astrometric offsets between NIRCam F444W and MIRI filters organized by survey. Mean offsets in $\langle\Delta\alpha\rangle$ (RA) and $\langle\Delta\delta\rangle$ (Dec), together with the corresponding standard deviations ($\sigma_{\Delta\alpha}$, $\sigma_{\Delta\delta}$) are shown for each survey pointing. Note the systematic pattern (shaded and unshaded rows), where pairs within each survey show consistency in their offsets due to the similar instrument alignment during observations.

wavelength to the blue channel, an intermediate wavelength to green, and the longest wavelength to red. In practice, however, this mapping is not always straightforward, as there may not always be three filters available. Indeed, many of the galaxies studied in this work were only imaged in one or two MIRI bands, compared to others that were observed in up to four filters (see Figure 5.3 in Section 5.2). In these cases, we fall back on previous NIRCam observations (Belli et al., 2025), particularly those taken in the F444W band, which lie closest to the wavelength range covered by MIRI. This comes with a few caveats, however. In order to produce RGB composite images, each filter does not only have to be astrometrically aligned, but also corrected for rotation among different instruments (MIRI vs. NIRCam) so that they can be properly overlaid. Furthermore, pixel sizes need to be consistent among all colour channels, which requires resampling of the NIRCam images to match the coarser MIRI pixels, which is a rather straightforward process. Compensating for the different angles of rotation between cutouts, however, proved a more complex task and required its own algorithm, which will be described in some more technical detail in the following paragraph.

4.2.3 Cutout Rotation and Alignment

In general, there are two main strategies to achieve rotated image cutouts from astrometrically aligned FITS files: One can take the large image mosaics of the surveys, obtain the global rotation angle, and rotate the entire file. Of course, this requires a careful adjustment of the WCS, since the rotated file is then used to look up galaxies from the catalogue using RA and Dec, which need to point to precisely the same location in the mosaic.

A second, and less complicated, approach is to directly take the 8"×8" cutouts used for photometry and rotate each of the images individually. After rotation, the image axes are resampled to match the sky coordinate system and cropped to 3"×3", without loss of data at the corners, regardless of the angle of rotation. This implementation comes with the important benefit that the rotation parameters of the WCS only need to be read and updated once. By not having to deal with the correct mapping of the reference pixels to the celestial coordinates, a major source of potential errors is eliminated. Furthermore, we do not need to store copies of large mosaic files and produce new cutouts from scratch.

Adopting the second strategy, the angle of rotation between the WCS pixel axes and the celestial coordinate system is extracted from the metadata stored in the FITS header of each 8"×8" cutout. In our case, the angle of rotation was derived from the elements of the PC matrix, with `"PC1_1"` representing the cosine of the angle and `"PC2_1"` encoding the sine. Since cosine is symmetric, the sign of `"PC2_1"` is used to resolve the quadrant ambiguity. Next, the original location of the reference pixel must be stored in both pixel coordinates (`"CRPIXi"`) and in sky coordinates (`"CRVALi"`) as they will be used to update the header after rotation. A standard rotation matrix is built for the determined rotation angle of the FITS file and multiplied by the PC-matrix, resulting in an updated PC-matrix. The new entries of this matrix are then written to the FITS header, and the pixel scale (`"CDELTi"`) is updated to match the original MIRI pixel scale. Because the reference sky coordinate no longer aligns with the same pixel after rotation, `"CRPIXi"` must also be adjusted accordingly. Finally, the image data is rotated using the `scipy.ndimage.rotate` function and cropped to a size of 3"×3", to match the format of the NIRCam RGB images available for the Blue Jay survey.

Figure 4.3 shows two examples of RGB images created in this way. Notice that the Figure 4.3a uses a resampled NIRCam image in the F444W filter for its blue channel to compensate for a missing third MIRI image. In both figures, there are regular patterns visible in the background, which appear as an artefact from the resampling procedure after rotating the cutout. Though this striped pattern is apparent in the complete RGB image, it is more clearly visible when inspecting the black and white cutouts used to create it. Notice also that these artefacts strongly depend on the brightness of the background and are not present in the NIRCam F444W image (the left-most cutout in the top panel of Figure 4.3a) since it was not rotated.

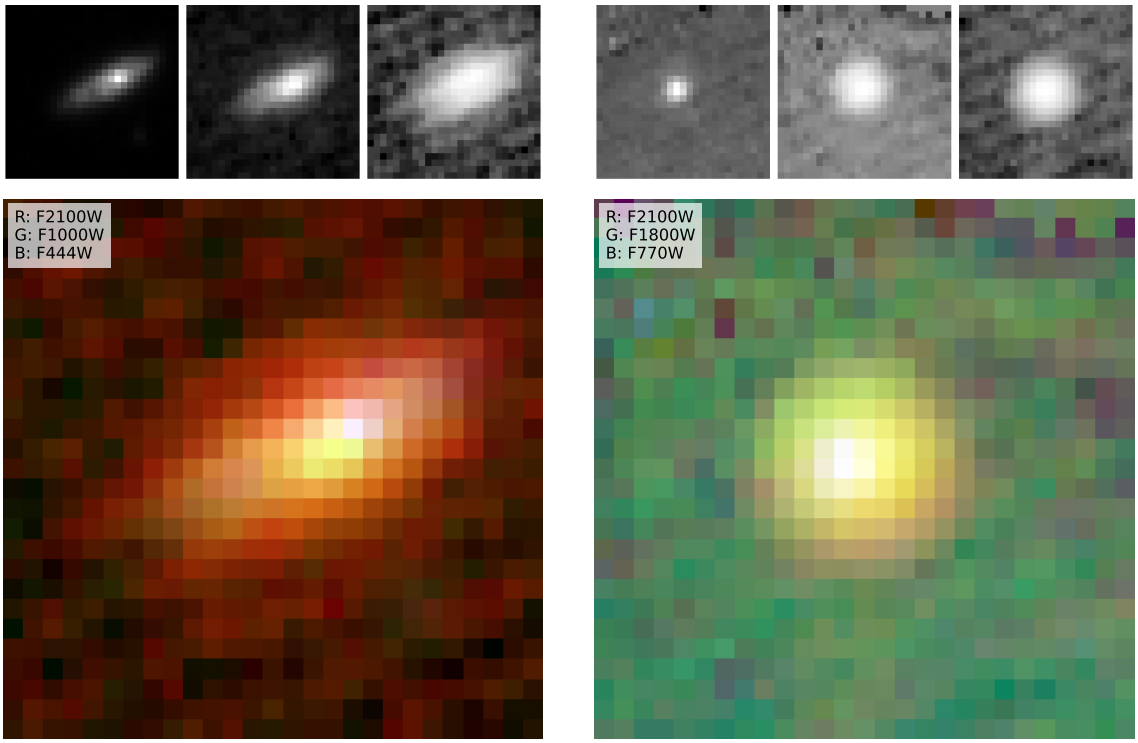

(a) (b)

Figure 4.3: RGB colour images of (a) object 13174 and (b) object 12282. The panel in the top left corner of each RGB image shows which filters were used for the red, green, and blue colour channels. The individual cutouts are displayed in the top panel, starting with the shortest wavelength band on the left. Notice that NIRCam F444W is used as the bluest filter in the left panel, since only two MIRI bands were available.

4.3 Aperture Definition and Optimisation

Aperture photometry is performed on the astrometrically corrected, but non-rotated MIRI images to avoid corruption of the data by spurious artefacts of the resampling process. We measure the MIRI photometry using modified NIRCam apertures used in the Blue Jay survey to ensure consistency with the rest of the sample. In a previous work (Park et al., 2024), elliptical apertures were defined using segmentation maps to determine the spatial extent of each galaxy in the NIRCam/F444W filter. The choice of this particular band was motivated by the fact that sources appear more extended at longer wavelengths due to the larger PSF and thus the aperture would be sufficiently large to capture the whole light emitted by the galaxy in all NIRCam and HST bands.

To apply the same apertures to the MIRI cutouts, they first need to be rotated to match the orientation of each MIRI cutout. However, upon visual inspection, it was found that many of the brighter galaxies imaged by MIRI extended significantly beyond the NIRCam/F444W apertures. As a consequence, the MIRI apertures were rescaled to twice the size of the original NIRCam apertures, with individual adjustments applied in a few cases where nearby sources could become blended due to the increased PSF extent. Since an aperture correction is applied to all measured fluxes, the choice of aperture size should not strongly influence the final photometry if the

model PSF accurately represents the detector response. To verify this, photometry was performed using both the original and the rescaled apertures across all four MIRI filters (F770W, F1000W, F1800W, F2100W), comparing small and large apertures to ensure that corrected fluxes converge and that residual differences due to aperture size do not dominate over typical photometric uncertainties. The findings of this analysis are presented in Section 4.5. Figure 4.4 illustrates the original (red) and adjusted MIRI apertures (blue, dashed).

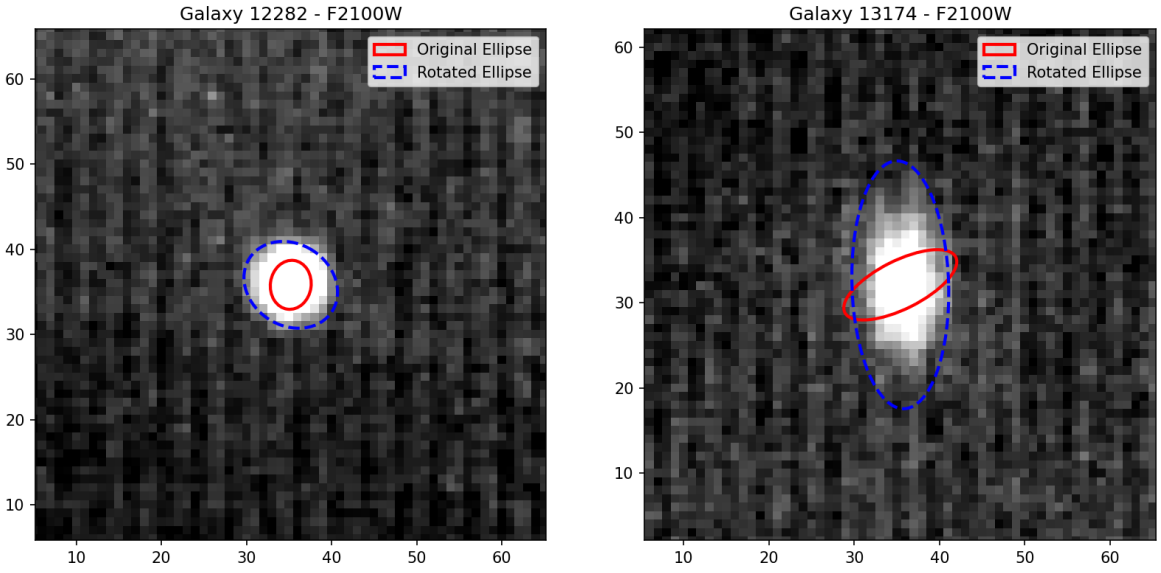

(a) (b)

Figure 4.4: Example of cutouts taken in the F2100W filter of objects with IDs 12282 (a) and 13174 (b). Displayed is a direct comparison between the adjusted aperture (blue dashed line) to the unmodified aperture based on the NIRCam F444W filter (red solid line).

4.4 Background Estimation and Photometric Measurements

4.4.1 Background Modelling Approach

As already mentioned in Section 2.4.4, the depths reached in MIRI images are limited by the background emission within each frame. Hence, accurate modelling of background noise is paramount for obtaining reliable science data, especially at longer wavelengths, where the thermal emission of the telescope adds significantly to the background (Dicken et al., 2024). There are a multitude of approaches to model and subtract the background, some of which include custom processing pipelines that were adapted from the official JWST science calibration pipeline (Alberts et al., 2024; Harish et al., 2025). In this work, a different approach was chosen. For each cutout taken from the fully calibrated mosaics (Level 3), we mask all invalid pixels or those that lie within the elliptical aperture obtained through the steps described in Section 4.3. In the next step, preliminary background statistics are obtained by calculating the median and standard deviation of the remaining pixels in the cutout using the `astropy`

function `sigma_clipped_stats` with a value of $\sigma = 2.5$. Based on these values, a threshold is defined as the median background noise plus twice the standard deviation. This number is then passed as parameters to the `detect_sources` function, which is part of the `photutils` package, together with the prior source mask. Furthermore, we require a minimum size of five pixels for each detected source to avoid masking of separate bright pixels as contaminating sources. The function returns a segmentation mask, which reliably hides all sources present in the image, thus allowing for robust modelling of the remaining background noise.

After processing the initial cutout data and identifying all sources, a 2-dimensional plane fit is applied to the remaining data using a least-squares estimation. This step aims to approximate the background noise gradient visible in many filters. In the majority of cases, a subtraction of the 2D plane from the science data yields a uniform, smooth background. This is not true when strong detector artefacts are present or the data contains gaps, which are often accompanied by several pixels with unphysical flux values around the perimeter. Fortunately, these cases are limited in number, which allows individual treatment upon visual inspection of the fitting process.

Figure 4.5 shows an example of the background modelling using a 2D plane fit. The left image shows the original science data with the corresponding plane fit in the middle figure. The right-hand side is obtained by a simple subtraction, as indicated by the '-' and '=' symbols in the figure. A clear difference is visible between the original cutout and the background-subtracted data, which now no longer shows a gradient in the signal. After obtaining a reliable background fit, an elliptical annulus is defined by simply rescaling the aperture used for photometry. An example case of the source masking routine can be seen in Figure 4.6. Notice that all unmasked background pixels are used for the plane fitting, and only afterwards is the annulus overlaid. The final background statistics are then obtained by taking the median and standard deviation of all unmasked residuals within the annulus region.

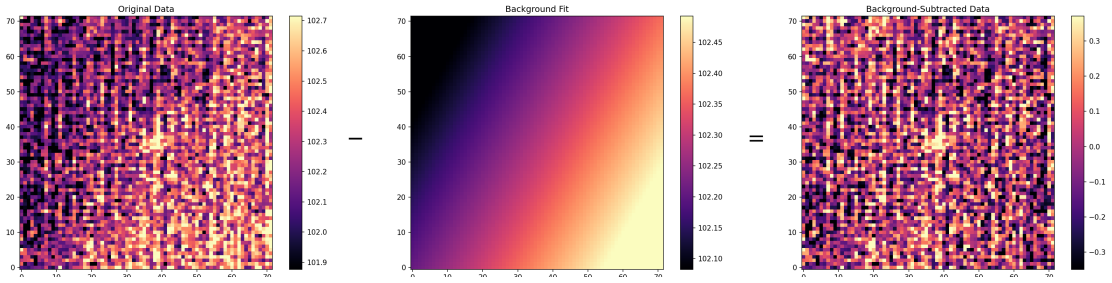

Figure 4.5: Result of the background modelling showing the original data (left), the background model (middle), and the background-subtracted data (right). The images show galaxy 7922 in the F1800W band.

4.4.2 Aperture Photometry

Aperture photometry is performed by taking the background-subtracted data and summing over all the pixels within the aperture. This is done using the built-in function `aperture_photometry` from the `photutils` package, using `method='exact'`, which

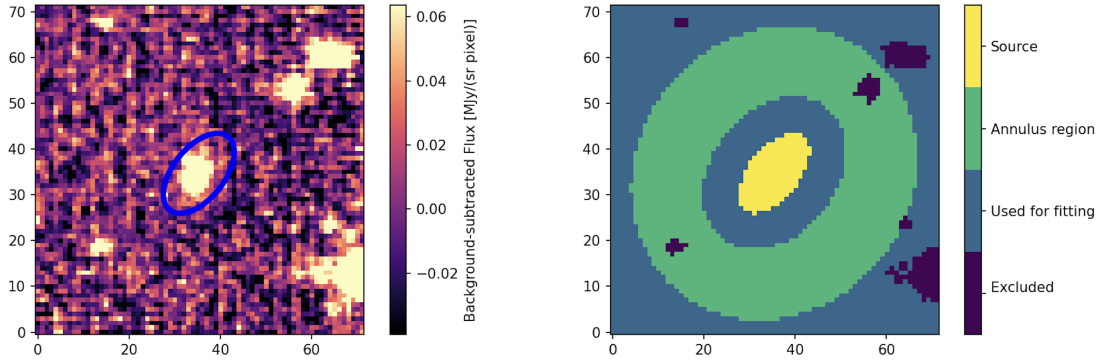

Figure 4.6: Example of the regions used for background modelling and statistical analysis. The left-hand side shows the background-subtracted data of galaxy 21424 in the F770W band. The corresponding regions are displayed on the right-hand side, where a clear distinction is made between the source, the annulus region, and the masked background pixels. All unmasked pixels outside the source region are used for the plane fit, independent of the annulus.

accounts for partial pixels by weighting each pixel according to the fraction that lies inside the aperture. To obtain the total errors on the flux measurement, we consider two main sources of uncertainty: The error obtained during background modelling and the `ERR` extension of the cutout. As described in Section 3.3, the latter stores the 1σ-uncertainty on the flux for every pixel in the `SCI` image.

To estimate the uncertainty on the background contribution within the aperture, we first compute the standard deviation of the residuals in the background annulus (excluding masked pixels):

$$\sigma_{bkg,pixel} = \mathrm{std}(I_{cutout} - I_{bkg,model})|_{\text{annulus region}} \,, \tag{4.1}$$

where only valid pixels not excluded by sigma-clipping are considered, and I_{cutout} and $I_{bkg,model}$ represent the image data and the background model, respectively. The 1-σ uncertainty on the total background flux within the source aperture is then

$$\sigma_{bkg} = \sigma_{bkg,pixel} \cdot \sqrt{N_{pix}^{aper}} \,, \tag{4.2}$$

where N_{pix}^{aper} is the area of the elliptical aperture in units of (fractional) MIRI pixels. To obtain the error contribution of the image errors to the flux measurement, a squared sum is carried out over all aperture pixels, assuming that each pixel value in the `ERR` extension is statistically independent of the others, so that

$$\sigma_{image} = \sqrt{\sum_{i \in \text{aperture}} \sigma_{ERR,i}^2} \,. \tag{4.3}$$

Finally, we estimate the total error on our photometric measurements by taking

$$\sigma_{tot} = \sqrt{\sigma_{image}^2 + \sigma_{bkg}^2} \tag{4.4}$$

4.5 Aperture Correction

4.5.1 Calculation of the Correction Factor

To obtain the final results for the photometric measurements, an aperture correction was applied to account for the lost light which falls outside the apertures due to the point spread function, as briefly mentioned in Section 4.3. These corrections are calculated individually for each band using the `STPSF` library[2] (formerly `WebbPSF`; Perrin et al., 2012). After generating the PSF models for each MIRI filter of interest, the correction factors were determined using the last (`"DET_DIST"`) extension of the PSF model FITS file, which provides a PSF model that is already binned to match the detector sampling pixel scale. This extension also accounts for "real-world" effects such as geometric distortion of the instrument, detector charge transfer, and inter-pixel capacitance. It thus provides the most accurate model of a PSF observed on a real detector. The aperture correction factor was derived from the PSF model by measuring the ratio of the total (normalised) PSF flux to the flux enclosed within the chosen aperture, given by

$$\alpha_{corr} = \frac{f_{total,PSF}}{f_{aperture,PSF}} \,. \tag{4.5}$$

All fluxes and errors were multiplied by this correction factor, calculated for the band in which the data were taken. This properly accounts for the detector response and strongly mitigates biases when comparing flux measurements at different wavelengths. Figure 4.7 shows a comparison of the PSF models generated per filter. As expected, the size of the PSF significantly increases with wavelength, which was the original motivation for upscaling aperture sizes to capture more of the integrated flux, particularly in the longer wavelength filters.

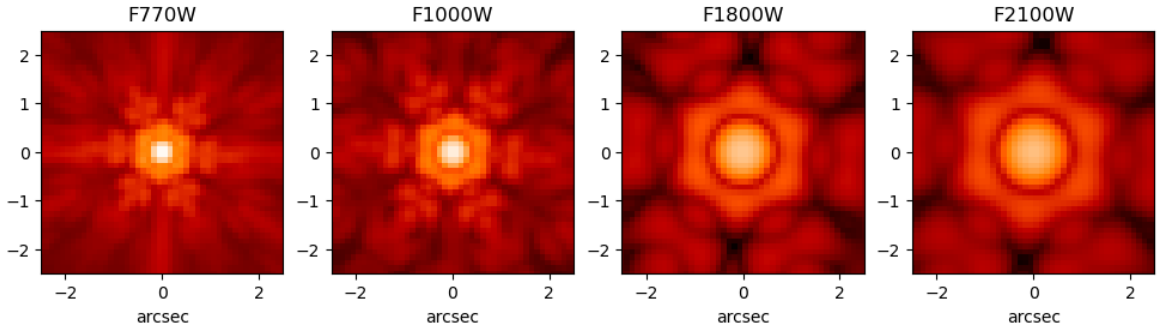

Figure 4.7: Comparison of different theoretical PSF models created with `stpsf` for the bands analysed in this work. All PSFs are sampled to match the pixel size on the MIRI detectors and include "real-world" distortions.

4.5.2 Validation of the Aperture Corrections

As mentioned in Section 4.3, photometry on the MIRI images was performed using larger apertures to account for the extended nature of sources seen in the individual

[2] https://stpsf.readthedocs.io/en/latest/index.html

cutouts due to the larger PSF. To make sure that the photometry is not significantly affected by the aperture rescaling, we perform aperture photometry with both the original (but rotated) NIRCam/F444W apertures and the rescaled MIRI apertures. The aperture correction is individually calculated for each aperture and applied to the measurements. Sources with intermediate-sized apertures, or with a signal-to-noise ratio below three (see Section 5.2) were excluded from the comparison, due to unstable flux ratios when dividing by near-zero values.

Figure 4.9 shows a detailed analysis of the robustness of the `stpsf` aperture corrections applied in this work for all four MIRI bands. The left column provides a comparison of corrected fluxes obtained in the original (small) and the rescaled (large) apertures. The middle column shows the distribution of corrected flux ratios (large/small) and the dependence of this ratio on the source brightness is displayed in the right-hand column.

Initially, a single clear outlier (ID 11451) was visible in the F770W band, with a flux ratio of ~ 3.5, far above the median value. Upon visual inspection of the cutouts shown in Figure 4.8, we find that the unusually large flux ratio comes from an imperfect astrometric alignment. This causes the source to largely fall outside the small aperture, whereas the majority of its emission is captured by the larger aperture. Its high ratio is therefore not attributable to an inconsistency in the applied aperture corrections and it is therefore excluded from the comparison.

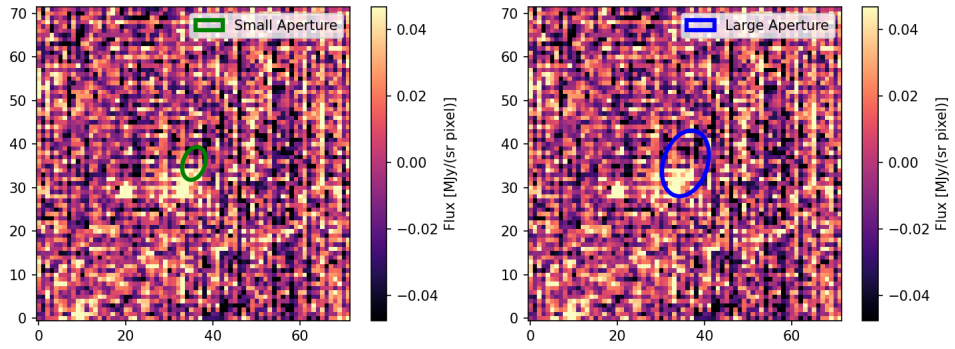

Figure 4.8: Comparison of small and large apertures in object 11451 to investigate the origin of the large flux ratio of ∼3.47.

Investigating Figure 4.9, we find that corrected fluxes lie close to the 1:1 line, with brighter sources clustering more tightly than faint objects - a trend which is also observed in the right-hand column. Furthermore, histograms of the flux ratios (middle column) confirm that the median corrected ratios lie $\sim 25\%$ above unity, with a relatively small scatter ($\sigma \lesssim 0.2$). This excess in flux likely reflects the more extended rest-frame near- and mid-infrared emission of galaxies, which smaller apertures partially miss, but which is captured by the larger apertures (see Section 4.3). Imperfect background subtraction could contribute at the faint end but cannot explain the consistent offset across all bands. In summary, this analysis demonstrates that the `stpsf` aperture corrections effectively compensate for the increased aperture sizes adopted in the photometric workflow presented in this thesis. The results of this analysis are summarised numerically in Table 4.2.

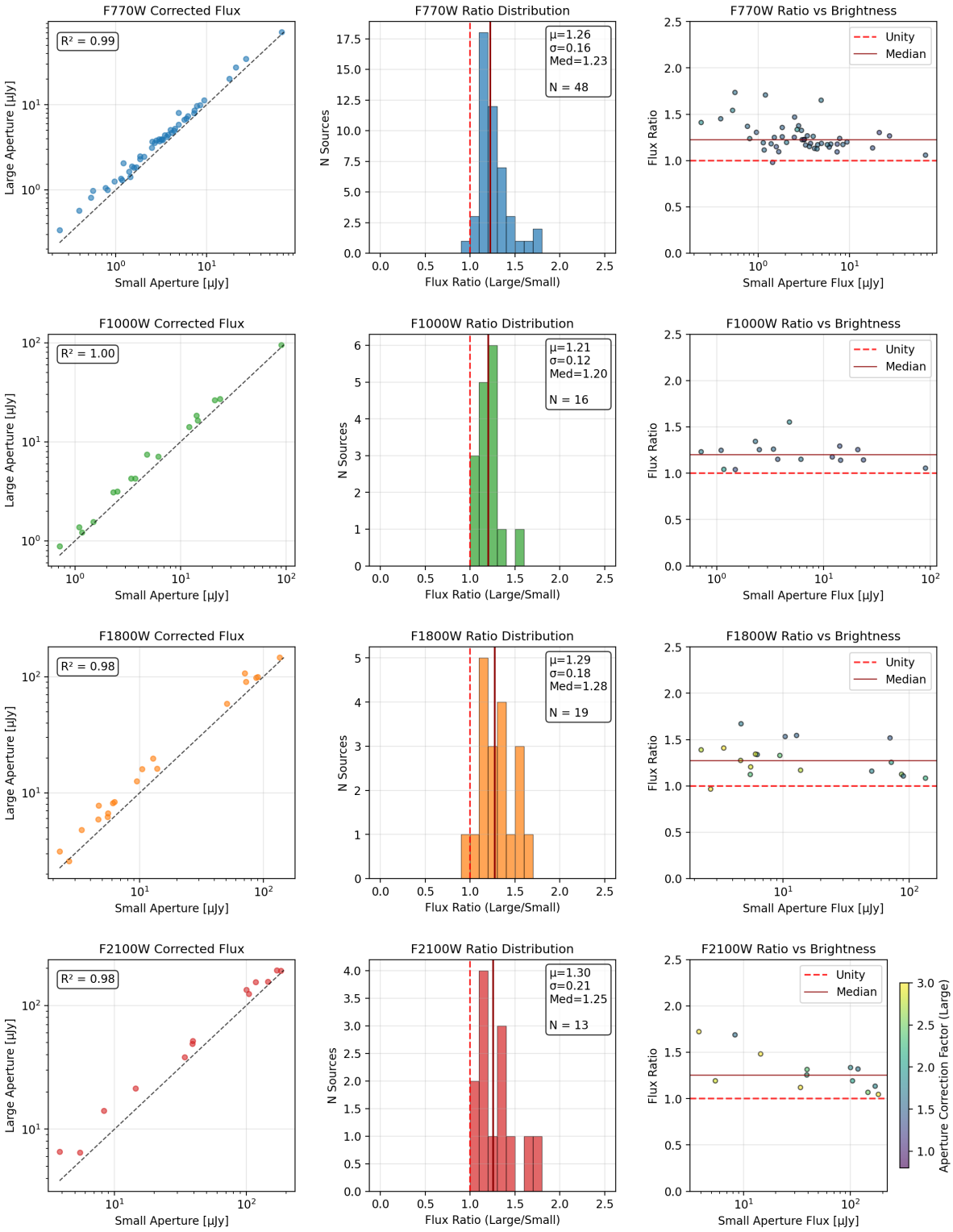

Figure 4.9: Aperture photometry comparison between small and large apertures across all four MIRI bands. Left column: Scatter plots comparing corrected fluxes between small and large apertures, with the 1:1 line (black dashed) and correlation coefficient R^2. Middle column: Distribution of corrected flux ratios (large/small aperture) with key statistics. The red dashed line indicates perfect agreement (ratio = 1.0), while the solid red line shows the median ratio. Right column: Flux ratio as a function of source brightness, coloured by aperture correction factor. The horizontal lines indicate unity and the median ratio. The source with ID 11451 was excluded from this analysis.

Table 4.2: Summary of aperture comparison statistics across all four MIRI filters. The table lists pre- and post-correction systematic biases, correction performance metrics, and uncertainty context. Residual biases of ∼20–30% indicate that the aperture correction successfully mitigates, though does not fully remove, flux discrepancies between small and large apertures.

Parameter	**F770W**	**F1000W**	**F1800W**	**F2100W**
Systematic Bias Assessment				
Initial bias (large/small aperture)	+46.7%	+48.8%	+110.3%	+108.0%
Residual bias after correction	+22.6%	+20.4%	+30.2%	+25.5%
Bias reduction[a]	51.6%	58.2%	72.6%	76.4%
Correction Performance				
Aperture correction factor ratio[b]	0.81	0.81	0.58	0.56
Median flux offset [μJy][c]	0.68 ± 1.41	0.91 ± 1.74	3.12 ± 8.33	9.84 ± 11.18
Sources with expected behaviour[d]	98.0%	100.0%	95.0%	100.0%
Uncertainty				
Median photometric error [μJy]	0.09	0.18	0.89	1.36
Median propagated error [μJy]	0.49	0.85	4.96	32.98
Offset significance[e]	7.6σ	5.1σ	3.5σ	2.8σ
Total sources analysed: 91				

[a] Percentage reduction in systematic bias: 100 × (raw bias − corrected bias)/raw bias.
[b] Ratio of large to small aperture correction factors.
[c] Median residual flux difference between corrected large and small aperture photometry ± standard deviation.
[d] Percentage of sources showing higher flux in large aperture after correction.
[e] Ratio of median flux offset to median photometric uncertainty, indicating statistical significance of residual bias.

4.6 Overview of the Catalogue

The final photometric catalogue was produced in FITS binary table format, containing both scalar and array columns for each galaxy. Scalar quantities, such as galaxy IDs, aperture sizes, position angles, and contamination flags, are stored alongside array-valued measurements including fluxes, associated errors, and AB magnitudes across all available filters. The filters for each galaxy are recorded as a comma-separated string, ensuring an unambiguous mapping between array entries and their corresponding bands. This table structure was chosen to balance compactness and clarity. It allows for efficient programmatic access for downstream analyses while providing a comprehensive overview of all measurements, uncertainties, and relevant quality flags such as detector artefacts or the presence of companions. Furthermore, this particular layout can be easily extended should more MIRI bands be added in the future, without having to restructure the catalogue. Columns containing potentially undefined or non-physical values (e.g., negative fluxes leading to invalid magnitudes) are masked using `astropy`'s `MaskedColumn` functionality.

The full photometric catalogue produced in this work will be made publicly available in a future release. Its structure is shown in Table 4.3 and a detailed description of its individual columns is provided in Appendix A.

Column Name	**Type**	**Units**	**Description**
`ID`	scalar	-	Unique galaxy identifier
`Flux`	array	µJy	Background-subtracted flux per filter
`Flux_Err`	array	µJy	Total uncertainty (noise + background)
`Image_Err`	array	µJy	Pixel uncertainty (ERR extension)
`Flux_BKG`	array	µJy	Background flux in the aperture
`Flux_BKG_Err`	array	µJy	Background uncertainty
`AB_Mag`	array	mag	AB magnitude per filter (masked if flux ≤ 0)
`Apr_Corr`	array	-	Aperture correction factor per filter
`Apr_Xcenter`	array	pixels	Aperture X-centre in MIRI pixels
`Apr_Ycenter`	array	pixels	Aperture Y-centre in MIRI pixels
`Apr_Theta`	array	degrees	Aperture orientation (East of North)
`Flag_Art`	array	-	True if detector artefacts present in filter
`Apr_A`	scalar	pixels	Semi-major axis of aperture in MIRI pixels
`Apr_B`	scalar	pixels	Semi-minor axis of aperture in MIRI pixels
`N_PIX`	scalar	pixels	Number of pixels in aperture
`Flag_Com`	scalar	-	Flag indicating nearby companion
`Filters`	scalar	-	List of available filters, comma-separated

Table 4.3: Description of the columns in the final photometric FITS catalogue.

4.7 The `miri_utils` Library

The entire photometric pipeline is summarised in Figure 4.10. Each step of the workflow was implemented using a custom-built Python library, `miri_utils`[3]. The library, publicly available as part of the `red_cardinal` repository on GitHub, provides all helper functions required for data analysis and visualisation, along with adaptable Jupyter notebooks designed to accommodate future MIRI observations.

While the JWST pipeline delivers well-calibrated mosaics at product Level 3, it lacks tools for generating galaxy-specific cutouts or performing consistent aperture photometry across multiple filters. Manual approaches are not only inefficient but can also introduce inconsistencies when handling large datasets with varying astrometry and signal-to-noise ratios. The `miri_utils` library addresses these limitations by providing a modular and reproducible framework for extracting, aligning, and performing aperture photometry on small cutouts centred on galaxies observed in different surveys. Its functions are fully modular and can be adapted to the structure of different catalogues. In addition, it includes flexible visualisation routines for inspecting astrometric offsets, background estimation, source masking, and summary statistics of the data.

The library also contains the `prospector_utils` package dedicated to loading and analysing outputs from Prospector. This module is used in Chapters 5 and 6 but is not discussed in detail here. Further information on the `red_cardinal` repository and guidelines for its use are provided in the accompanying `README.md` file. A schematic overview of the directory tree is shown in Figure 4.11, and the individual Python files are described below.

Module: `astrometry_utils.py`

Purpose This module provides functions for computing and visualising astrometric offsets between NIRCam and MIRI cutouts, together with a correction routine.

Key Functions Contains functions to load cutout data and compute the pixel coordinates of the centroids. Uses the WCS transform to calculate the astrometric offsets in terms of RA and Dec. Produces summary statistics and figures, which serve as a useful tool for the user to validate the offset computation.

Requires `astropy`, `matplotlib`, `photutils`.

Module: `cutout_tools.py`

Purpose This module stores all functionalities related to the creation and manipulation of small FITS cutouts that are used throughout the workflow.

Key Functions Loops through a catalogue and extracts regions of user-determined size around the specified coordinates, preserving all FITS extensions. Calculates rotation angles between the Y-pixel axis of each cutout and celestial North. Generates preview PNG images and provides useful tools for rotation, cropping, and resampling of cutouts, which are used to produce RGB-composite images.

[3] https://github.com/benjaminpcollins/red_cardinal/tree/main/miri_utils

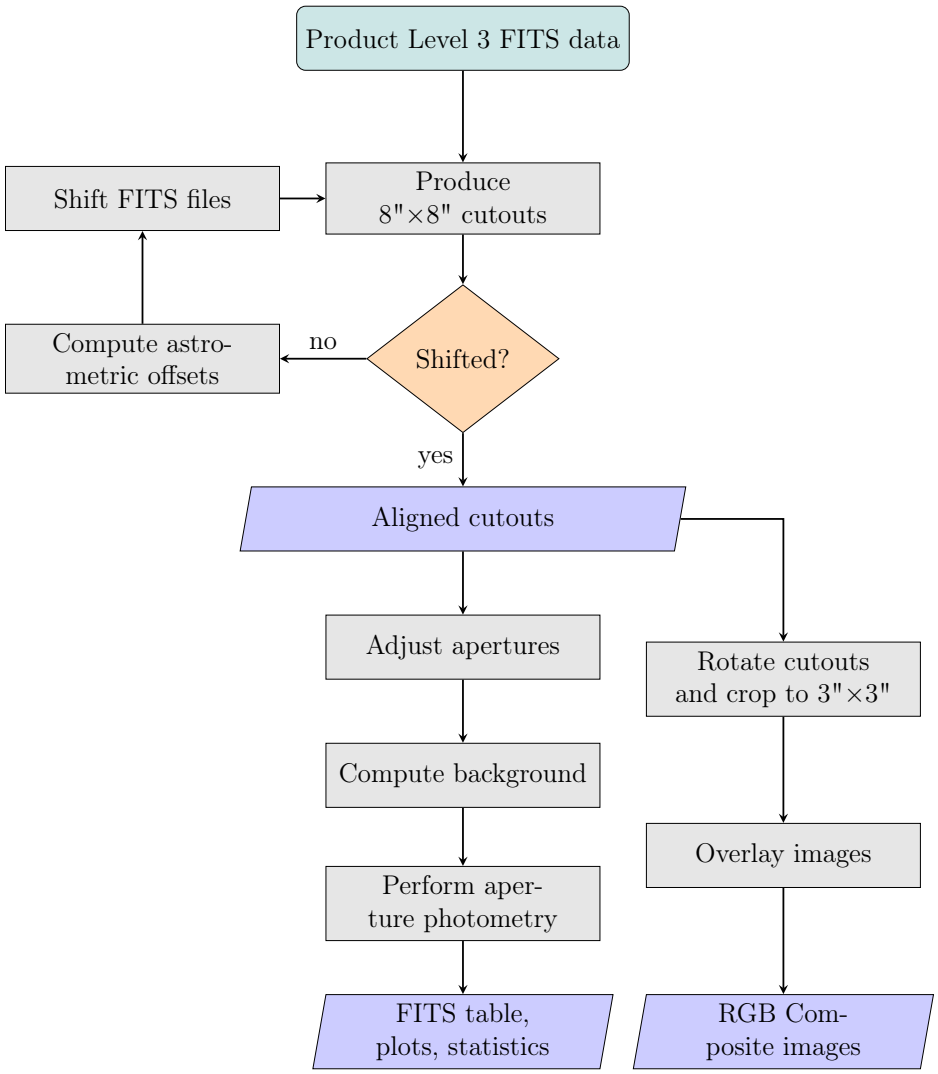

Figure 4.10: Workflow of the photometric pipeline implemented in the `miri_utils` package.

Requires `numpy`, `astropy`, `matplotlib` and `scipy.ndimage`.

Module: `photometry_tools.py`

Purpose This module contains all functions used in the photometric pipeline and produces photometric catalogues that can be used for scientific analysis.

Key Functions Includes an algorithm for rotating and rescaling existing apertures and a sophisticated background modelling and source masking routine. Uses an elliptical annulus to obtain statistics of the background-subtracted data. Performs aperture photometry using the adjusted apertures and immediately applies aperture corrections to the fluxes and errors. Contains plotting functions to visualise statistics of galaxy imaging and detections, as well as validations of aperture corrections and comparisons with other photometric catalogues. Produces a comprehensive photometry table in the FITS binary table format.

Requires `pandas`, `numpy`, `h5py`, `json`, `astropy`, `matplotlib`, `photutils`, and `collections`

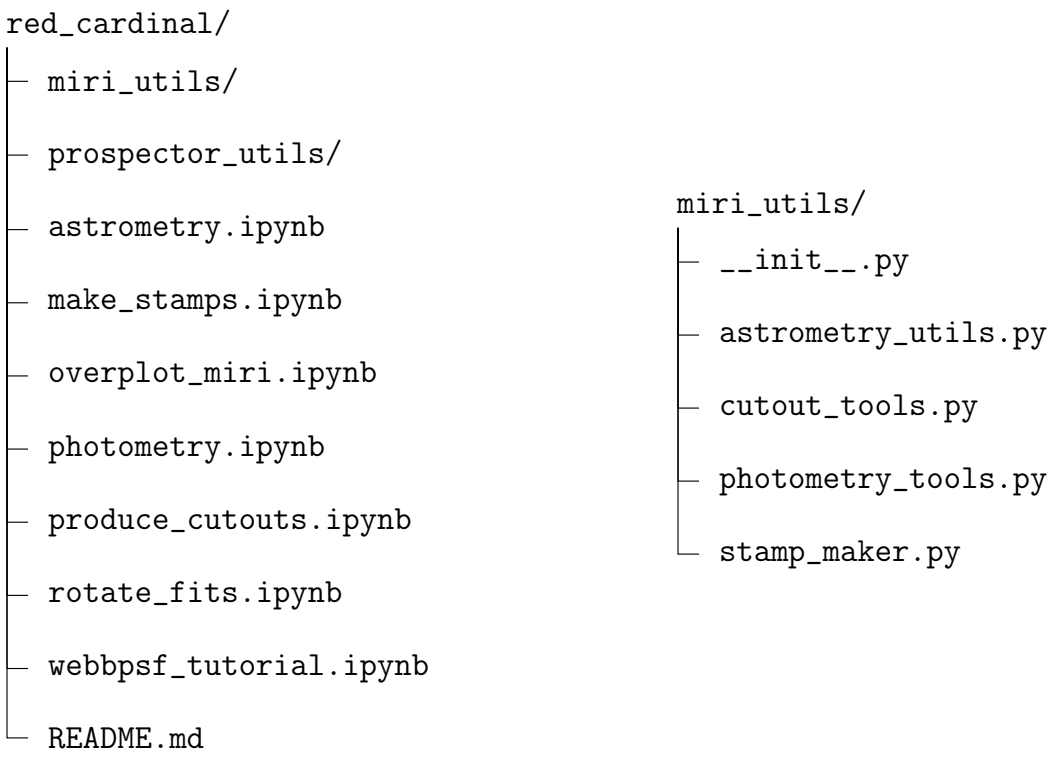

Figure 4.11: Directory tree of the `red_cardinal` repository and the `miri_utils` package.

Module: `stamp_maker.py`

Purpose This module provides the utilities necessary for creating colour-composite images from FITS data obtained from the JWST MIRI and NIRCam instruments.

Key Functions Consists functions that preprocess the separate cutouts and rescale their data to ensure proper relative strengths between different colour channels. Takes rotated, resampled, and cropped 3×3 arcseconds^2 cutouts as input and alignes them with NIRCam if necessary to create RGB composite images.

Requires `numpy`, `astropy`, `matplotlib` and `collections`.

Chapter 5

Catalogue Validation and Sample Characterisation

5.1 Validation of Photometric Measurements

To verify the validity and robustness of the photometric pipeline implemented for this work, we compare our photometric catalogue to the COSMOS2025 catalogue (Shuntov et al., 2025). It was published in the COSMOS-Web Public Data Release 1 (DR1) and represents the flagship data release of the survey (see Section 3.2). Overall, it provides photometry, morphology, photometric redshifts, and a variety of physical parameters for over 700,000 galaxies in the COSMOS field. Source detection was performed using a combined NIRCam image and a hot–cold technique to identify both bright and faint objects. Photometry was extracted through two complementary methods: fixed-aperture measurements on the space-based bands (HST/ACS, NIRCam, MIRI) and total fluxes derived from profile-fitting (SE++) across all 37 available bands, spanning 0.3–8 µm. Morphological parameters were obtained via both parametric profile fitting and machine-learning classification. Photometric redshifts and galaxy properties, including non-parametric star formation histories, were derived through SED fitting. The catalogue achieves high photometric redshift accuracy ($\sigma_{MAD} \leq 0.03$) and improved completeness relative to its predecessor, COSMOS2020 (Weaver et al., 2023), providing reliable measurements to $\log(M_*/M_\odot) \sim 9$ at $z \sim 10$.

Since the COSMOS2025 catalogue only contains MIRI photometry in the F770W filter, we restrict our comparison to one band to serve as an important validation of the photometric measurements performed in this thesis. To compare the data, the full photometric catalogue was downloaded from the official COSMOS-Web DR1 website[1]. All photometric measurements are stored in extension 1 of the catalogue, containing 287 columns in total. For this comparison, sources are identified by their sky coordinates using the columns `"ra"` and `"dec"` rather than by catalogue identifiers, since different surveys often employ their own naming conventions. To match the sources of the COSMOS2025 catalogue to those analysed in this thesis, we use the `match_to_catalog_sky` function of the `astropy` package. A maximum uncertainty of 0.3 arcseconds was imposed to account for minor discrepancies in the reported positions. The final sample of

[1] https://cosmos2025.iap.fr

matched galaxies consists of 56 objects - a number that drops to 48 if the separation constraint is tightened to 0.2 arcseconds.

As mentioned above, we restrict the flux comparison to the F770W band, since it was the only filter used for observations in the COSMOS-Web survey. We use the columns "`flux_auto_f770w`" and "`flux_err_auto_f770w`" to obtain the aperture corrected fluxes and corresponding measurement errors from the COSMOS2025 catalogue in µJy. The results of the comparison are displayed in Figure 5.1, which presents both a flux comparison with error bars (left) and the fractional flux difference between the catalogues (right), calculated by

$$\Delta f = \frac{f_{\text{Cosmos}} - f_{\text{Blue Jay}}}{f_{\text{Blue Jay}}} \,. \tag{5.1}$$

Figure 5.1 shows a clear trend, with measurements converging towards the brighter end of the sample, resulting in a median fractional flux difference of only 0.018 µJy. However, the faint end of the sample exhibits a significant scatter. In general, the larger error bars obtained in this work appear consistent with the discrepancy between the catalogues and are likely a result of the different approaches in background estimation and subtraction.

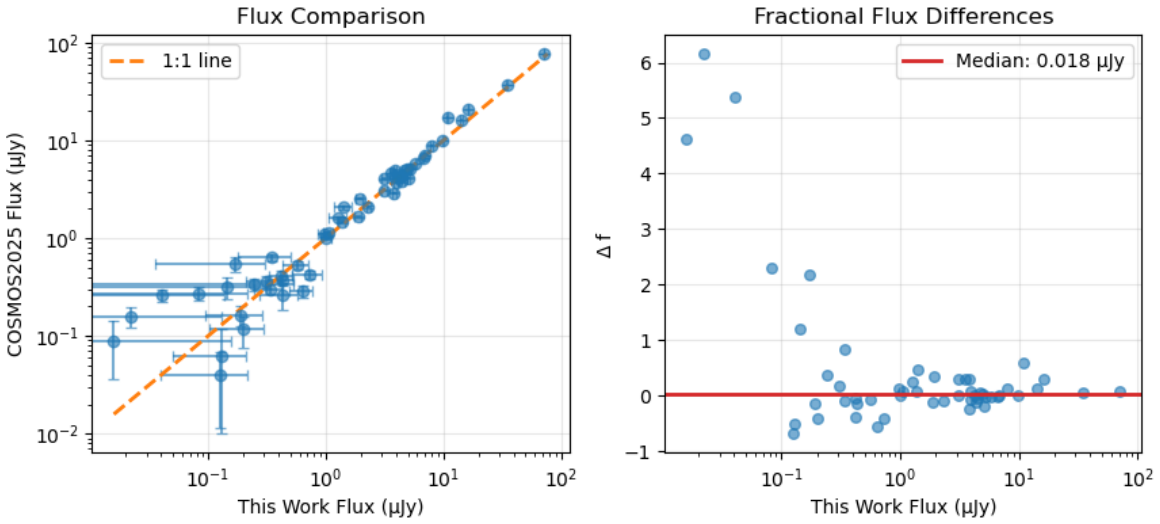

Figure 5.1: Comparison of our photometric table to the COSMOS2025 catalogue, showing a flux comparison with error bars (left) and fractional flux differences (right). A clear convergence of measurements is visible for brighter sources, with a median fractional flux difference of 0.018 µJy.

A comparison of the photometric errors and the distribution of fluxes is shown in Figure 5.2. As mentioned above, the errors obtained in this work are generally larger than those reported in COSMOS2025, and show little correlation. This once again highlights the critical role of background modelling and subtraction when performing photometry with MIRI, as different approaches can lead to very different results, especially for faint sources. The right-hand side of Figure 5.2 shows a clear alignment between the two catalogues, albeit with small differences towards the fainter end.

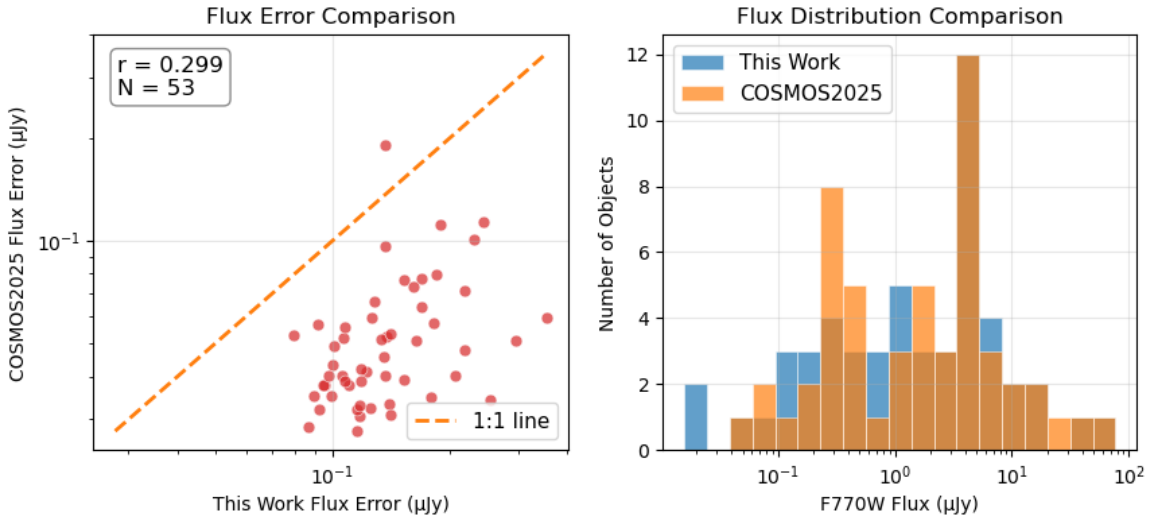

Figure 5.2: Comparison of photometric errors (left) and the distribution of measured MIRI fluxes (right) between this work and the COSMOS2025 photometric catalogue.

In summary, the consistency with COSMOS2025 strongly suggests that our measurements are physically plausible and robust. This serves as a valuable proof of concept for the custom background modelling and photometric measurement routines developed in this work, while also confirming the consistency of the adopted units.

5.2 MIRI Detection Statistics

Overall, 102 out of the 153 Blue Jay galaxies have at least one valid MIRI observation; in this section, we aim to identify detections within those images. Initially, MIRI detections were determined through visual inspection of the individual cutouts, which were rescaled to minimise contamination from bright background sources. This preliminary assessment was subsequently refined with an automated signal-to-noise (S/N)–based flagging routine, providing a more robust and quantitative classification of non-detections. The algorithm used flux measurements and their associated errors from the photometric catalogue to identify all sources with S/N<3.

For objects with inconsistent classifications (manual vs. automatic), we estimate an empirical aperture RMS. This is done by placing 200 random apertures on the masked cutout, excluding the original aperture region and bright sources, and deriving an empirical S/N. The aperture dimensions matched those of the original photometry to ensure consistency. This method reduces the influence of correlated noise between source and background on the S/N estimate. Ultimately, we adopt galaxies as non-detections if they were flagged by either of the automatic routines. This procedure replaced manual visual inspection with a reproducible and objective method for assigning detection statistics of the sample.

Figure 5.3 provides a visual representation of these statistics in the form of a heat map for easier comparison between imaged sources and confirmed detections. Each column corresponds to a MIRI band and each row marks a galaxy. Galaxy IDs that are trailed by an asterisk (*) indicate the presence of a companion in at least one filter, and darker tiles mark detector artefacts or bad pixels in the cutout.

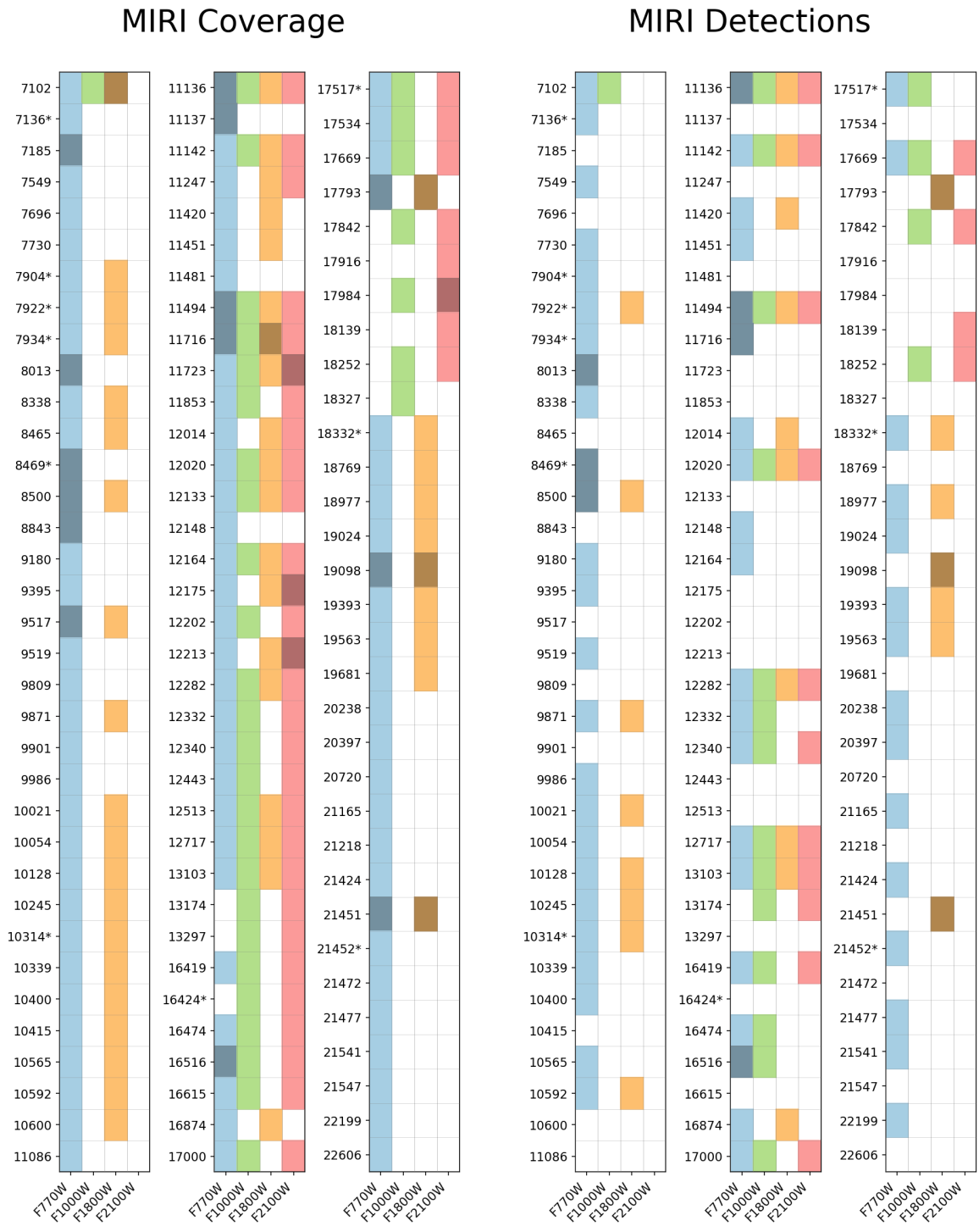

Figure 5.3: Heat map showing (a) all filters available for each galaxy ID and (b) whether the galaxy is detected or not. All patches coloured in a darker shading represent image data that is affected by detector artefacts (e.g., regular noise patterns, bad pixels), whereas all galaxy IDs marked with an asterisk represent galaxies with a companion.

5.3 Construction and Properties of the Final Sample

To obtain the final sample, we load all available Prospector outputs and cross-match them with the galaxies in the MIRI sample. Out of the 102 galaxies observed with MIRI, six (IDs 7136, 7696, 9517, 11247, 11420, and 19681) lack PROSPECTOR fitting data, while a further seven (IDs 7102, 11723, 12282, 12513, 18769, 18977, and 21472) were excluded due to unreliable fits (see Figures B.1 and B.2 in Appendix B).

Hereafter, we refer to the *MIRI sample* as all observed galaxies (N = 102) and to the *final sample* as the subset used for the analysis with PROSPECTOR (N = 89). The numbers of available and detected MIRI galaxies in each sample is given in Table 5.1. The left-hand columns correspond to the MIRI sample (102 galaxies), while the right-hand columns show the subset for which PROSPECTOR fits are available. In the following paragraphs, we will investigate the properties of objects in both samples to understand the underlying galaxy population and identify possible detection biases.

Band	**MIRI sample (N = 102)**		**Final sample (N = 89)**	
	Observed	**Detected**	**Observed**	**Detected**
F770W	93	60	80	55
F1000W	33	19	29	17
F1800W	49	25	39	22
F2100W	37	15	33	14

Table 5.1: Availability and detections within the MIRI (102 galaxies) and the final sample (89 galaxies). The table lists the number of galaxies observed and detected in each MIRI band.

Figure 5.4 shows the MIRI sample with respect to stellar masses and redshifts of the individual galaxies, colour-coded by their absolute a and relative b number of MIRI bands in which they were detected. A clear trend is visible, with most non-detections (marked as yellow or white dots) clustering on the bottom third of the diagram. The emerging cut-off suggests a mass-complete sample for $\log(M_*/M_\odot) \gtrsim 10$. Within the final sample, 62 out of 89 galaxies (69.6%) are detected in at least one band.

In Figure 5.5 we display the MIRI sample for each band and colour the individual galaxies by their observed flux. The F770W band mainly probes the rest-frame near-IR emission of the galaxies, where the light emitted by the galaxy is still strongly affected by the stellar continuum of old stellar populations. As a consequence, massive quiescent galaxies are more easily captured in this band, leading to a large number of detections. However, the longer-wavelength bands increasingly probe the emission of heated dust grains in the ISM and are thus more sensitive to light coming from dusty star-forming galaxies, which typically do not occupy the high-mass end of the population.

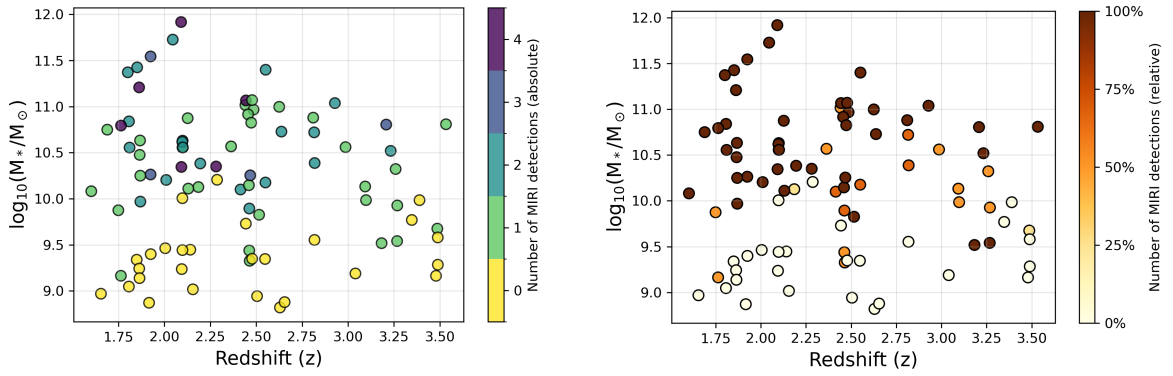

(a) (b)

Figure 5.4: Masses and redshifts of the MIRI sample, colour-coded by the absolute (a) and relative (b) number of detected MIRI bands.

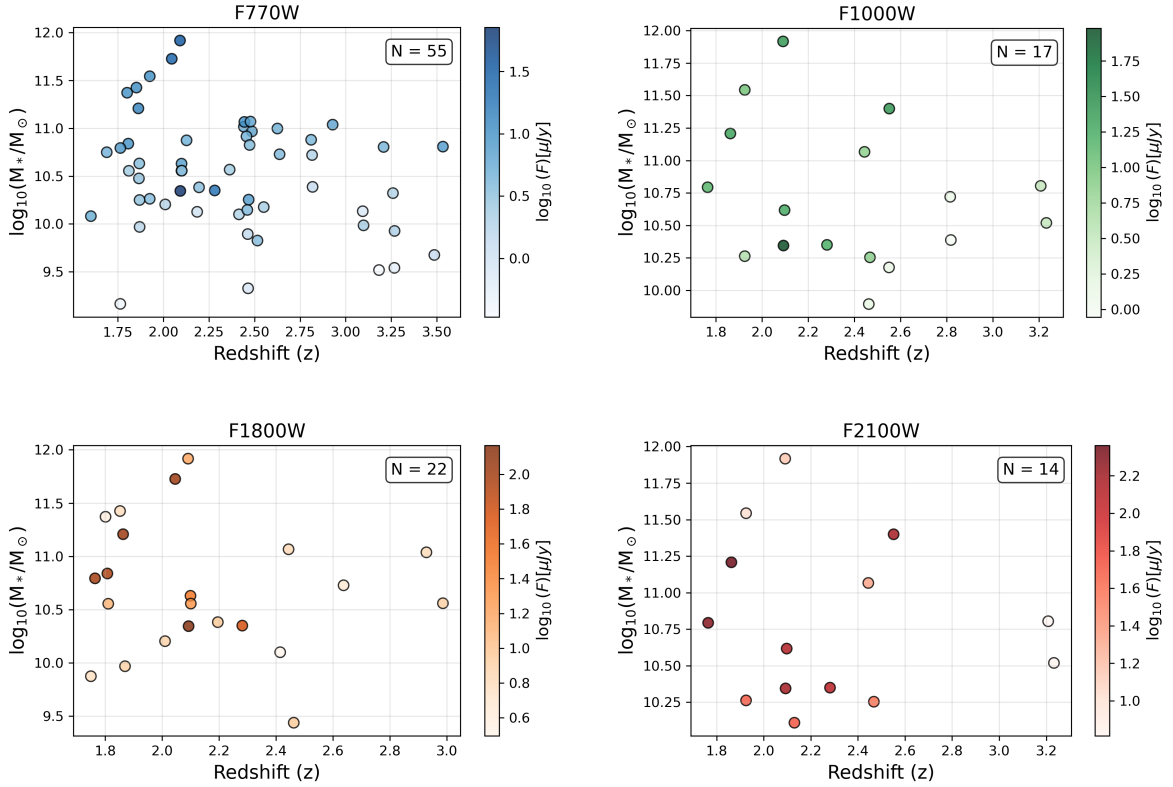

Figure 5.5: Stellar masses and redshifts of detected galaxies within the final sample, colour-coded by the measured flux in each band (F770W, F1000W, F1800W, and F2100W).

Next, we focus on identifying the different galaxy populations within the final sample. As discussed in Section 1.1, galaxies can roughly be classified as star-forming or quiescent by looking at their position with respect to the star-forming main sequence (SFMS). For this purpose, we reconstruct the star-formation rates (SFRs) of the galaxies from the Prospector outputs, which contain the non-parametric star-formation histories (SFHs) inferred during spectral fitting. This is done by first computing the age of the Universe at each galaxy's redshift and dividing it into a series of user-specified age bins. During spectral fitting, Prospector records the fractional stellar mass

formed in each age bin by accounting for all stellar populations in the model. For more detail, see Leja et al. (2019).

Finally, we can reconstruct the star formation rates by comparing the star-forming ratios to the total mass of the galaxy. Since the position and spacing of the age bins depend on the galaxy's redshift, we estimate the average SFR over the last 100 Myr, thus ensuring a consistent measure of recent star formation.

For the star-forming main sequence, we adopt the parametrisation found in Leja et al. (2022), which was measured for $z \sim 0.2$ up to $z \sim 3$ using Prospector and thus provides a reference that is consistent with our sample. We compare our sample to the SFMS evaluated at the median sample redshift $z_{MS} \sim 2.43$ for a representative comparison and display the results in Figure 5.6. Again, we colour objects in the sample by their relative number of detected bands.

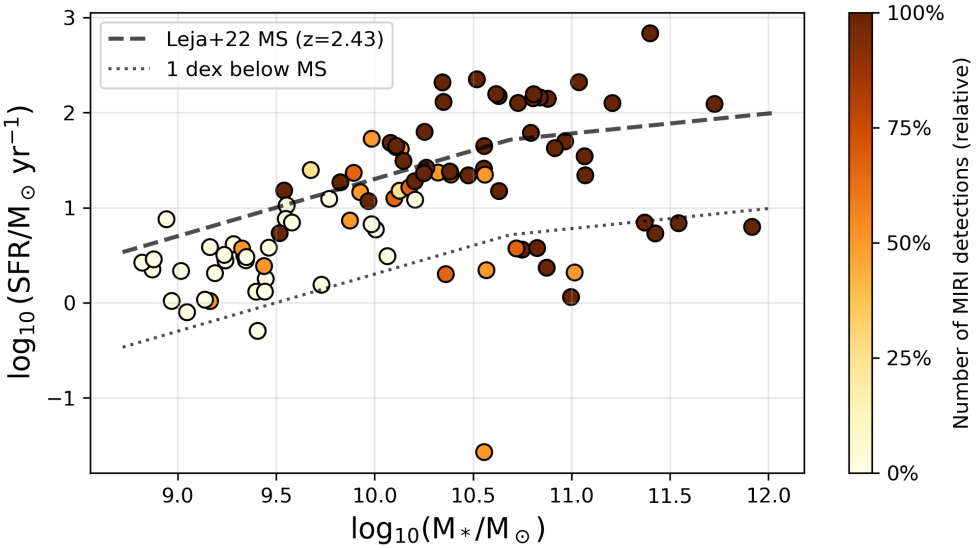

Figure 5.6: Star-formation rate with respect to stellar mass of the final sample, colour-coded by the relative number of detected MIRI bands. The dashed line marks the star-forming main sequence from Speagle et al. (2014) at the median sample redshift ($z \sim 2.43$). The thin dashed line shows the -1 dex limit.

We classify galaxies as quiescent when their specific star formation rate falls more than ∼1 dex below the star-forming main sequence. In total, 13 galaxies meet this criterion (see Chapter 6). Furthermore, Figure 5.6 confirms that we reliably detect both quiescent and star-forming systems above a stellar mass of $\log(M_*/M_\odot) \gtrsim 10$.

Chapter 6

Investigating Dust Energy Balance

6.1 Preparation of the Data

To test dust energy balance, we compare the MIRI data to the best-fit model spectra derived from HST and NIRCam photometry and NIRSpec spectroscopy from the Blue Jay survey (Belli et al., 2025). Since no MIRI data were available when the Prospector fits were computed for the Blue Jay sample, the resulting fits relied on the assumption of dust energy balance to model extrapolate the infrared emission of galaxies. As discussed in Section 1.3.2, this is a key feature of many modern stellar population inference codes, which requires that all energy absorbed by dust grains in the optical and UV regime is re-emitted in the infrared. In this section, we investigate the validity of this assumption by directly comparing the measured MIRI photometry to the predicted infrared emission.

The observed photometry cannot be directly compared to the model spectrum. Instead, we need to compare it to the model photometry, which is the convolution of the model spectrum with the filter transmission curves of the instrument. Prospector automatically returns the model photometry for the bands used for SED fitting. However, since the MIRI data were not used for the original fits, we manually compute the expected fluxes using the `getSED` function from the `sedpy` Python package. To obtain the error bars, we compute 200 spectra by sampling from the posterior distribution of the fit parameters, weighted by their respective probabilities. We compute the model photometry for the 16th- and 84th-percentile spectra, and use the difference as the 1σ-uncertainty. Figure 6.1 shows the reconstructed fit for ID 11142, a post-starburst galaxy analysed in Belli et al. (2024), for which the Prospector fit is remarkably successful in predicting MIRI fluxes in all four bands.

6.2 Analysing the Fit Quality

To estimate the accuracy of the predicted fluxes in the i-th band, we compute the difference between the observed photometry $f_{obs,i}$ and the model prediction $f_{model,i}$ given by

$$\Delta f_i = f_{obs,i} - f_{model,i} \,. \tag{6.1}$$

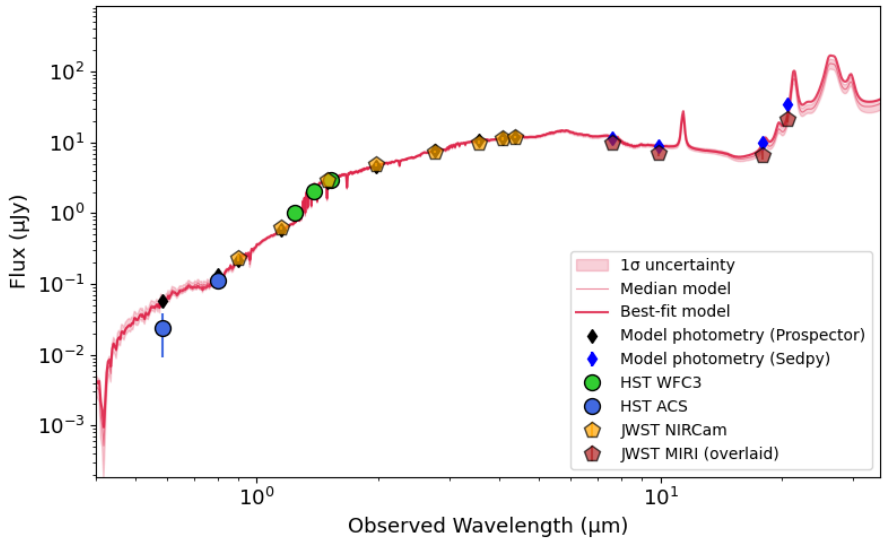

Figure 6.1: Example of the reconstructed best-fit model for the object with 3D-HST ID 11142. The median spectrum and the 1σ uncertainty envelope are also displayed. The green and blue circles, as well as the orange pentagons, correspond to HST/WFC3, ACS, and JWST/NIRCam bands, respectively, all of which were used to produce the fit. Instead, the red pentagons represent the MIRI measurements discussed in this work. Black diamonds denote Prospector model photometry, while the blue diamonds were obtained *a posteriori* using `sedpy`.

We can then express this discrepancy in terms of the number of standard deviations in the i-th band, $N_{\sigma,i}$, by taking the ratio of the flux differences over the squared sum of the errors

$$N_{\sigma,i} = \frac{\Delta f_i}{\sqrt{\sigma^2_{obs,i} + \sigma^2_{model,i}}}\,, \tag{6.2}$$

where $\sigma_{obs,i}$ and $\sigma_{model,i}$ are the total photometric error and the model uncertainty, respectively. If the model is consistent with the data and under the assumption of Gaussian errors, the resulting distribution of N_σ values in each band should approximate a normalised Gaussian curve $\mathcal{N}(0,1)$. The results of the analysis are shown in Figure 6.2, which displays the distribution of N_σ values for each band. Text boxes in the top right corner of each panel show the mean, standard deviation, median, and sample size in each panel. The Gaussian approximation of the distribution (colourful line) and the reference $\mathcal{N}(0,1)$ distribution (grey line) are overlaid.

A clear trend emerges in Figure 6.2. The centre of each N_σ distribution shifts progressively towards negative values with increasing wavelength, while the overall scatter remains roughly constant. Recalling the definition of Δf_i in Equation (6.1), this implies that Prospector systematically overpredicts fluxes in the mid-infrared, with the bias becoming more pronounced at longer wavelengths.

In the F770W band (top left panel in Figure 6.2), the predicted fluxes agree well with the measured values, though with noticeable scatter. This is expected, as this band lies closest to the wavelength range directly constrained by the fitted data, where the contribution of the stellar continuum to the measured light is still significant. At

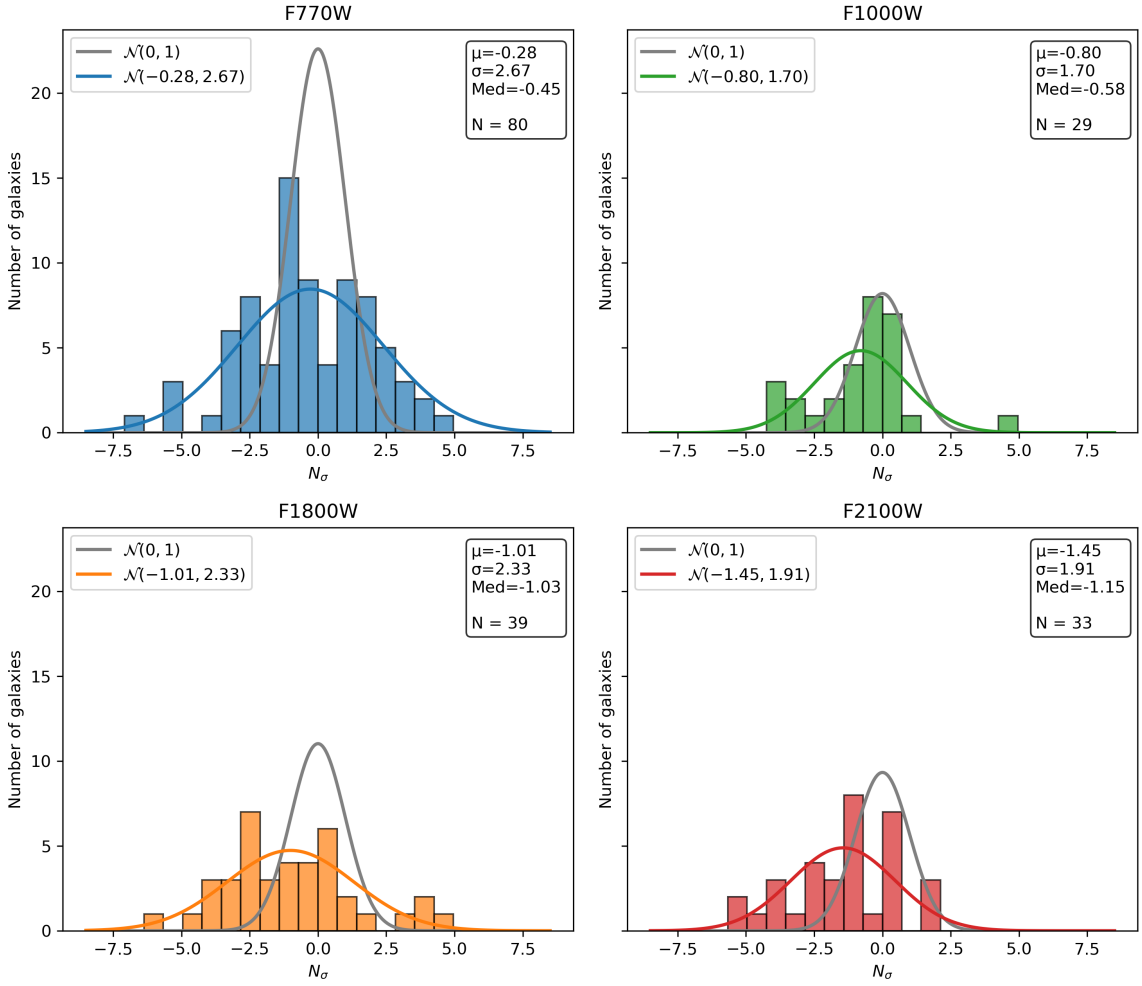

Figure 6.2: Statistical distribution of N_σ values in each of the four MIRI bands. The mean, standard deviation, median, and the number of galaxies in each band are displayed in the top right corner of each panel. The reference Gaussian distribution $\mathcal{N}(0, 1)$ is shown as a grey line. All distributions are scaled to the same number counts for better comparability.

longer wavelengths, however, the bands probe spectral regions increasingly distant from the fitted data, requiring the SED model to rely more heavily on dust energy balance to reproduce the observed IR emission. In particular, Prospector calculates the attenuation of stellar light based on the photometry and spectra available to it, and is then faced with the task of redistributing all this energy towards the infrared. The resulting bias towards larger IR fluxes likely reflects limitations in our current understanding of the physical processes governing dust reprocessing in the ISM. This trend is illustrated in Figure 6.3, which shows six representative cases where the SED models overpredict the infrared emission.

Despite the systematic bias, the scatter remains consistent across all bands ($2.06 < \sigma < 3.56$), with almost identical values in the F770W and F2100W filters. This indicates that while Prospector slightly overestimates mid-IR fluxes, it does so with a stable degree of precision. In other words, the model's internal assumptions about the shape of the IR emission appear to be robust, suggesting that the model is not merely

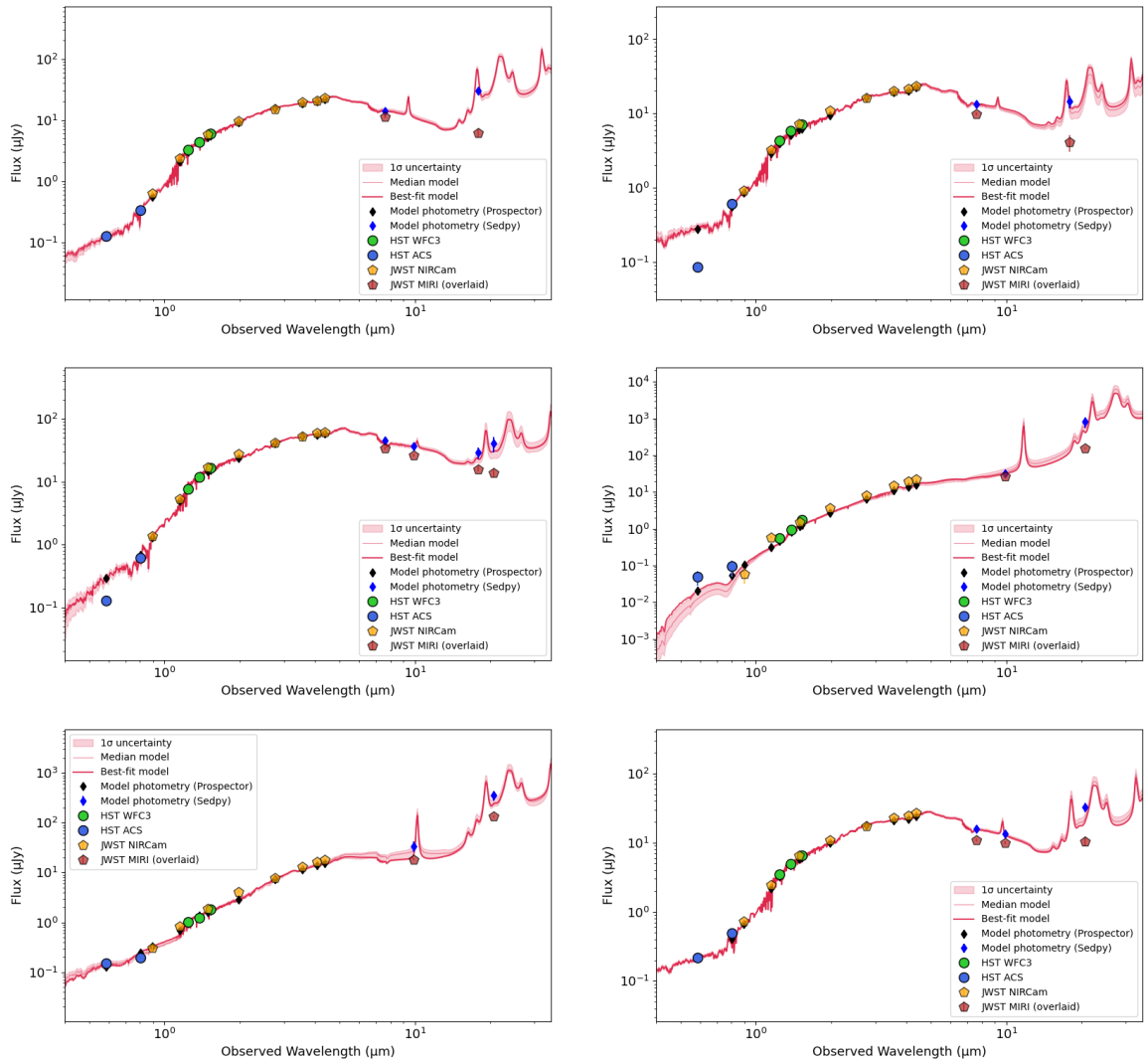

Figure 6.3: Examples of Prospector fits, where observed MIRI fluxes are overpredicted. The coloured dots and the orange hexagons represent the HST and JWST/NIRCam photometry used to obtain the best fit model (red line), while the MIRI photometry (red hexagons) is overlaid a posteriori. The blue diamonds represent the model photometry as predicted by `sedpy`, which should be observed by MIRI given the model SED.

"guessing" the shape of the SED at these wavelengths, but is instead redistributing the absorbed energy in a physically consistent, albeit imperfect, manner.

Figure 6.4 shows the distribution of the same galaxies with respect to masses and redshifts in each MIRI band and coloured by N_σ. Prospector seems to most accurately model galaxies at intermediate masses, and tends to overestimate (underestimate) the IR-emission in more (less) massive systems, which also tend to be the dustiest.

Next, we quantify the discrepancy between the model and the observed data in the i-th band by calculating the logarithmic flux ratio

$$R_i = \log\left(\frac{f_{obs_i}}{f_{model,i}}\right). \tag{6.3}$$

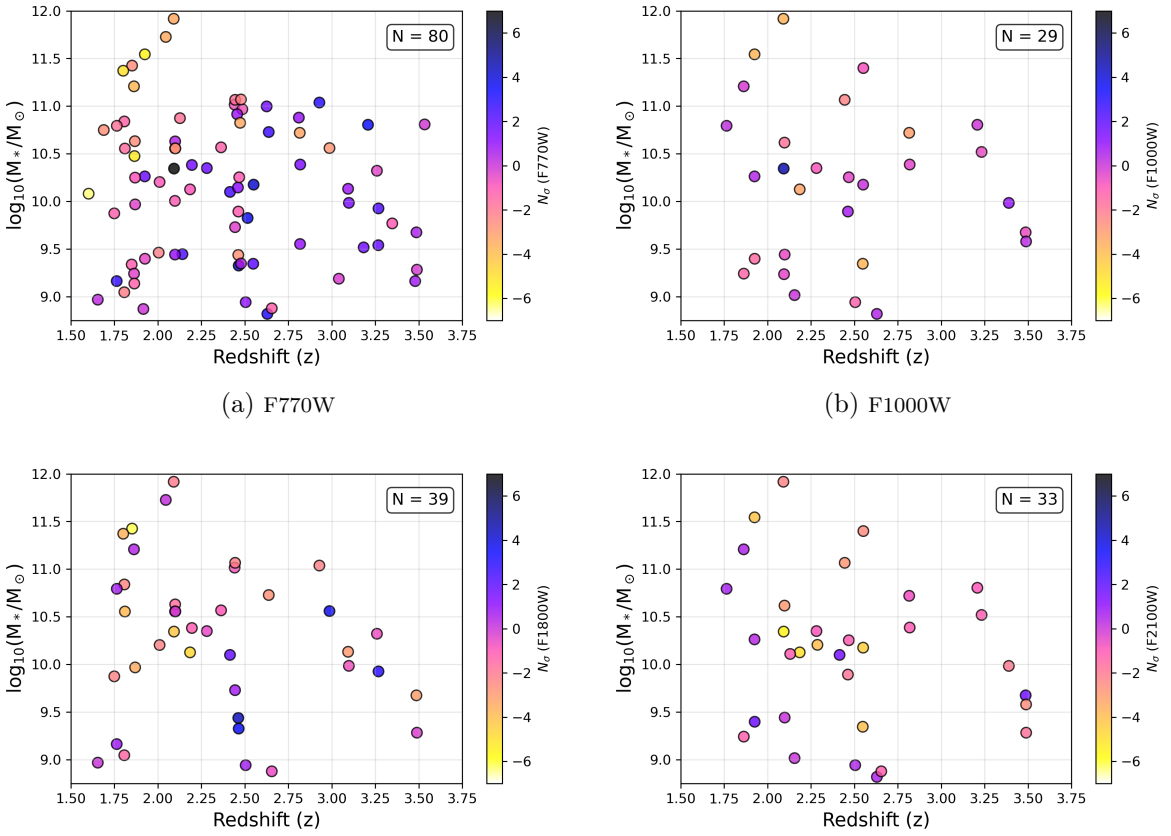

(a) F770W (b) F1000W

(c) F1800W (d) F2100W

Figure 6.4: Stellar masses and redshifts of the MIRI sample, colourised by N_σ in the (a) F770W, (b) F1000W, (c) F1800W, and (d) F2100W bands, calculated according to Equation (6.2).

Analysing the distribution of R values in each band allows us to quantify existing biases and the overall scatter in relative terms. For this part of the analysis, we restrict the data to reliable detections only, since non-detected sources can drastically influence the shape of the distributions if photometric errors are not accounted for. The results are presented in Figure 6.5 together with a statistical summary in each panel, stating the mean, standard deviation, median, and the sample size.

As in Figure 6.2, a trend is visible towards more negative values of R with increasing wavelength. Across the shorter-wavelength MIRI bands (F770W and F1000W), the uncertainty between model predictions and observed photometry remains within 0.2 dex, suggesting that Prospector recovers fluxes in these bands rather consistently. Mean differences lie between $-0.02 > R > -0.06$, corresponding to a less than 15% overprediction of fluxes. In contrast, the longer-wavelength bands (F1800W and F2100W) show larger discrepancies ($0.27 < \sigma < 0.56$), indicating that Prospector produces far-infrared fluxes which are roughly a factor of two to three larger than observed. Furthermore, these results are biased by the exclusion of non-detections, which could decrease R further if considered.

Finally, we compute the reduced χ^2 statistic for each galaxy, which is a common measure to estimate the fit quality. It is defined as

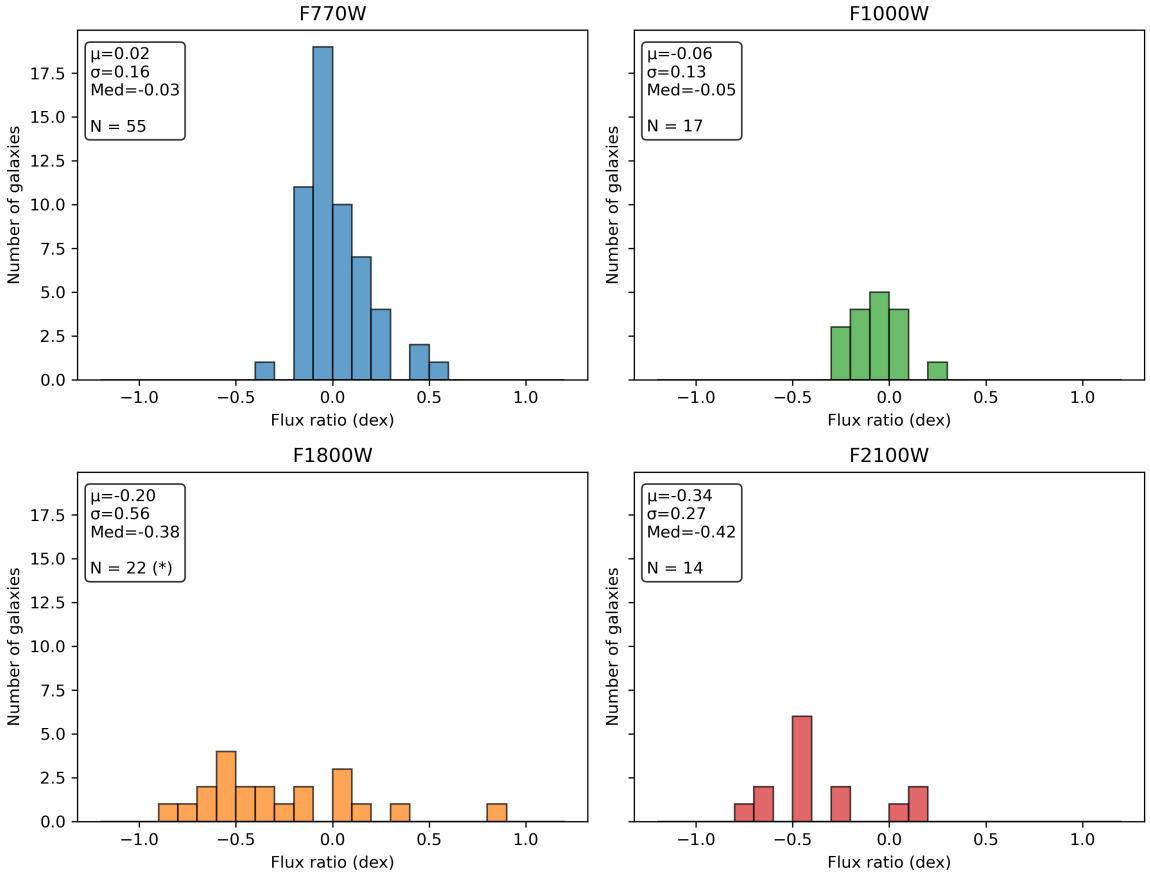

Figure 6.5: Distribution of the logarithmic flux ratio R in each filter. Text boxes in the top left corner of each panel show corresponding statistics such as the mean, standard deviation, median, and the number of objects. One galaxy with a ratio of 1.6 was omitted from the F1800W panel for display purposes, indicated by an asterisk (*) next to the number of galaxies.

$$\chi^2_{\text{red}} = \frac{1}{N} \sum_{i=1}^{N} N^2_{\sigma,i} \,, \tag{6.4}$$

where N is the number of bands available for each galaxy. Figure 6.6 shows the distribution of χ^2 values for the final sample, together with the dependence of χ^2_{red} on the number of bands available for each galaxy. In cases where the data are used to fit the model, a reduced χ^2 close to unity indicates optimal agreement. In our case, Prospector is *not* fitting the MIRI data, but is predicting them based on observations at shorter wavelengths, achieving a median value of ∼3.3, which is quite remarkable.

Lastly, we investigate how dust attenuation and star formation rate influence the accuracy of Prospector in the infrared regime. For this part of the analysis, we exclude 14 quiescent galaxies (IDs 7549, 8013, 8469, 9395, 10128, 10339, 10400, 10565, 10592, 11142, 11494, 16419, 18668, 21477) found in Bugiani et al. (2025), as well as ID 12332, which lies below 1 dex of the star-forming main sequence shown in Figure 5.6.

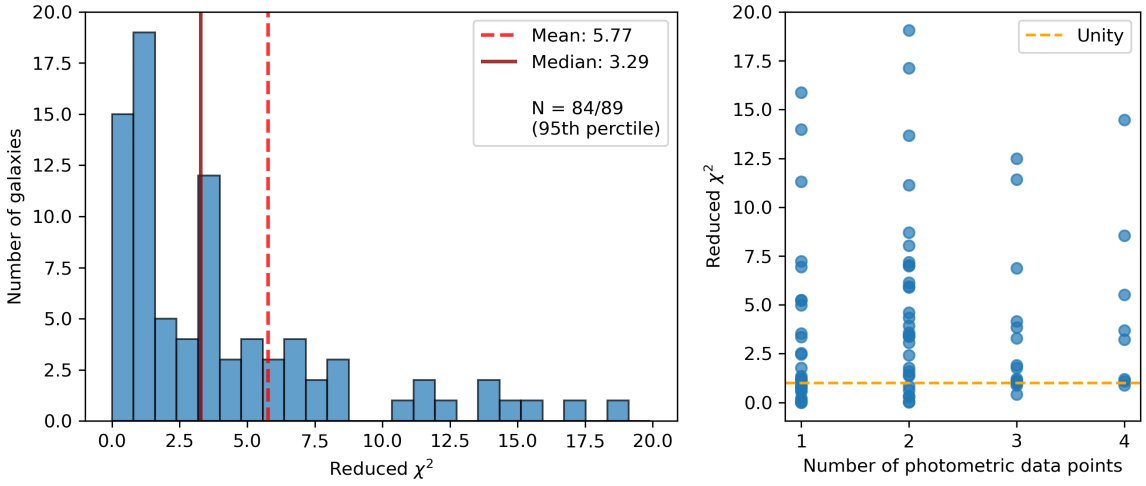

Figure 6.6: Distribution of reduced χ^2-values of the final sample (left) and its dependence on the number of photometric bands available (right). For better visibility, only sources below the 95th percentile of the χ^2_ν distribution are shown (84 out of 89 sources). Vertical lines for the mean and median are overlaid.

Focusing on the two reddest filters, F1800W and F2100W, we calculate the specific star formation rate (sSFR = SFR/M_*) and extract the best-fit dust attenuation parameter A_V for each galaxy. The results are displayed in Figure 6.7 with respect to N_σ. The colour scaling represents the inferred dust attenuation (left) and the sSFR (right).

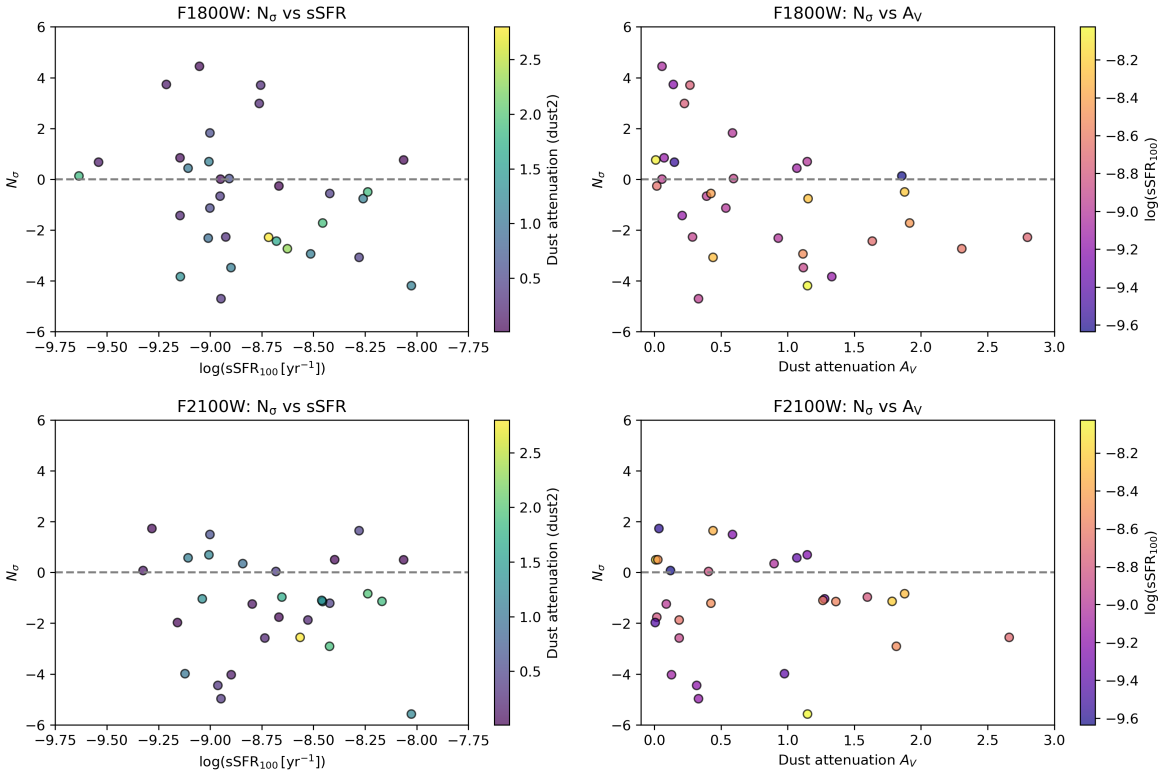

Figure 6.7: Distribution of N_σ values with respect to specific star formation rate (sSFR) and dust attenuation A_V in the F1800W and F2100W bands.

Focusing on the left-hand side, the fit quality does not appear to strongly correlate with the sSFR of star-forming galaxies in the F2100W band, showing no clear trends of N_σ values over the whole range. In F1800W, on the other hand, the distribution tends to shift towards smaller values of N_σ with stronger star formation, which could be explained by the increasingly dusty nature of star-forming galaxies at cosmic noon, which leads the model to predict stronger dust emission. The right-hand side of Figure 6.7 shows a clear trend. Dust attenuation does indeed significantly influence the quality of the fits, with the majority of galaxies with $A_V > 1$ exhibiting less flux in the infrared than predicted. Positive values of N_σ (corresponding to underpredictions of the model) are clustered exclusively around the least dusty end of the sample, where the assumption of dust energy balance becomes less important for the resulting shape of the SED.

Chapter 7

Conclusion and Outlook

In this chapter, I present a summary of my work, discuss the main findings, and set them into a scientific context. I conclude this thesis by giving an outlook on possible future surveys that could be undertaken to build upon this work.

7.1 Summary of this Work

In this thesis, I performed photometry on a sub-sample of the Blue Jay survey, a medium-sized JWST Cycle 1 programme which obtained deep spectroscopy in the near-IR for 153 galaxies in the COSMOS field between redshifts $1.7 < z < 3.5$. Using observations from the PRIMER, COSMOS-Web, and COSMOS-3D surveys obtained with the Mid-Infrared Instrument (MIRI) onboard JWST, I implemented a custom photometric pipeline to obtain reliable photometry across four MIRI bands (F770W, F1000W, F1800W, and F2100W), which is used to test the assumption of dust energy balance.

The first step of the photometric workflow consists of locating galaxies on large mosaic files via their right ascensions (RA) and declinations (Dec), and producing square-shaped cutouts. Next, the data are corrected for astrometric offsets with respect to the available NIRCam photometry of the Blue Jay catalogue. RGB-composite images are produced by assigning each MIRI band to a colour channel and overlaying individual cutouts. In cases where fewer than three MIRI bands are available, NIRCam cutouts are used for the bluest channel. In addition to astrometric alignment, the production of colour images required rotating individual cutouts to compensate for the orientation of the telescope during different observing runs, resampling of the pixels, and rescaling the data to ensure similar flux levels in all bands.

For consistency, MIRI photometry was performed using the same apertures as those employed for HST and NIRCam measurements in the Blue Jay catalogue. Besides being rotated to match the orientation of the MIRI images, aperture sizes were increased by a factor of two to account for the larger point spread function (PSF) and potential extended emission in the mid-infrared. A detailed comparison between the fluxes measured in the big and small apertures showed that aperture-corrected fluxes were

$\sim$ 25% higher across all bands when the big apertures were used. We conclude that the `stpsf` aperture corrections properly compensate for the larger apertures, and we attribute the consistent surplus in fluxes to the extended emission in the near- and mid-infrared, which is not captured by the smaller apertures.

Special care was given to accurately model the local background and the mask contaminating bright sources and bad pixels in each MIRI cutout. To mitigate the presence of local noise gradients, a 2D plane is fit to the background and subtracted from the data. Next, we estimate the contribution of the background flux within the aperture by computing the median background value within an elliptical annulus surrounding the source aperture, together with the root-mean-squared background error. Finally, aperture photometry is performed on the plane-subtracted data. All fluxes and errors are aperture-corrected and dynamically stored in a photometric table in the FITS format, together with the aperture parameters and individual flags. The final catalogue uses scalar and array columns for easy access and data handling and will be made publicly available in a future publication.

The measured F770W photometry is compared to the COSMOS2025 catalogue from the public Data Release 1 (DR1) of the COSMOS-Web survey. While this catalogue only contains data for the F770W band, this comparison serves as a validation of the photometric measurements and adopted units across all MIRI bands analysed in this work.

The full photometric pipeline implemented in this work is collected into a custom Python package `miri_utils`, which is publicly available on GitHub[1] and discussed in detail in Section 4.7. The `red_cardinal` repository includes all helper functions and notebooks used for data analysis and visualisation, enabling reproducibility and transparency of the measurement process. The library will undergo further refinement upon completion of this work, and I am confident that it will prove useful for future studies with MIRI.

In this work, I investigated the validity of dust energy balance. In contrast to traditional SED models, which depend on solving the radiative transfer equation for individual galaxies, many modern SED fitting codes rely on dust energy balance to compute the infrared emission of galaxies. This approach assumes that all the energy absorbed by dust grains in the optical-UV is re-emitted in the infrared regime. This rather simple yet physically motivated assumption enables SED fitting for large samples of galaxies to determine stellar populations and chemical abundances. However, few tests have been carried out assessing its predictive power when high-quality mid-infrared photometry or strong priors in the infrared are unavailable.

To test this assumption, we compare the newly measured MIRI photometry to existing best-fit model spectra, which were derived using only photometry from HST and NIRCam and spectroscopy from NIRSpec taken during the Blue Jay survey, but no MIRI data. I performed a variety of statistical analyses to identify possible biases and quantify the discrepancy between the model predictions and the observed MIRI photometry and presented the results in Chapter 6.

[1] https://github.com/benjaminpcollins/red_cardinal

7.2 Discussion of the Results

The statistical analyses discussed in Chapter 6 show that, to first order, PROSPECTOR is capable of predicting the shape of the infrared SED of galaxies to a reasonable degree. However, when looking more closely, a trend emerges towards overestimating the infrared luminosity of galaxies in the final sample. This bias becomes more pronounced at longer wavelengths, where high-quality photometry and spectra are not available to guide the shape of the SED, and the code thus relies on the inferred dust absorption to determine how much energy should be redistributed towards the infrared regime. Overall, no significant increase in uncertainty is observed at longer wavelengths, indicating that the model is indeed physically motivated and not randomly "guessing" the shape of the SED.

Besides identifying general biases of the model, we also quantify the offsets between the model and the observations in each band, as shown in Figure 6.5. We find modest offsets in the F770W and F1000W bands, with predicted values typically lying within 0.2 dex from the actual photometry, indicating a discrepancy of less than 50% of the measured flux in each band. In the F1800W and F2100W bands, however, the model tends to overpredict fluxes by around $\sim$0.5 dex, equalling approximately three times the measured MIRI flux. This is a solid result, especially given the simplicity of dust energy balance compared to traditional radiative transfer models.

To understand the origin of the observed discrepancy, we consider several possible explanations, ranging from limitations in the adopted dust templates to orientation effects and the assumption of dust energy balance. Indeed, the offset between the model and the data could be explained by the way we model certain components of the dust emission (e.g., PAH emission), particularly if the priors given to the model are incorrect and do not fully capture the underlying physics behind dust emission. However, the spectral features inferred by PROSPECTOR are frequently observed in the spectra of dusty, star-forming galaxies, suggesting that the problem likely does not lie in the template spectra themselves.

To estimate the fit quality, we initially express the offsets between the model and the observed fluxes in terms of standard deviations N_σ, as indicated in Equation (6.2). In this context, negative (positive) values of N_σ correspond to overpredicted (underpredicted) model fluxes. Figure 6.7 in Chapter 6 shows how the fit quality varies with dust attenuation (A_V) and specific star formation rate (sSFR). In Figure 7.1, we zoom in on the top right panel of that figure to discuss the trend in detail.

For dusty galaxies ($A_V \gtrsim 1$), the model consistently overpredicts infrared emission. This trend vanishes when moving towards galaxies with very low dust emission ($A_V \lesssim 0.25$). Here, IR fluxes are underestimated by the model. Overall, this indicates that for galaxies with small amounts of dust, the model does not have enough absorbed energy to redistribute towards the infrared and reach the higher fluxes observed. Likewise, PROSPECTOR overestimates the infrared emission for galaxies with strong dust attenuation.

A possible explanation involves the relative orientation of the galaxy with respect

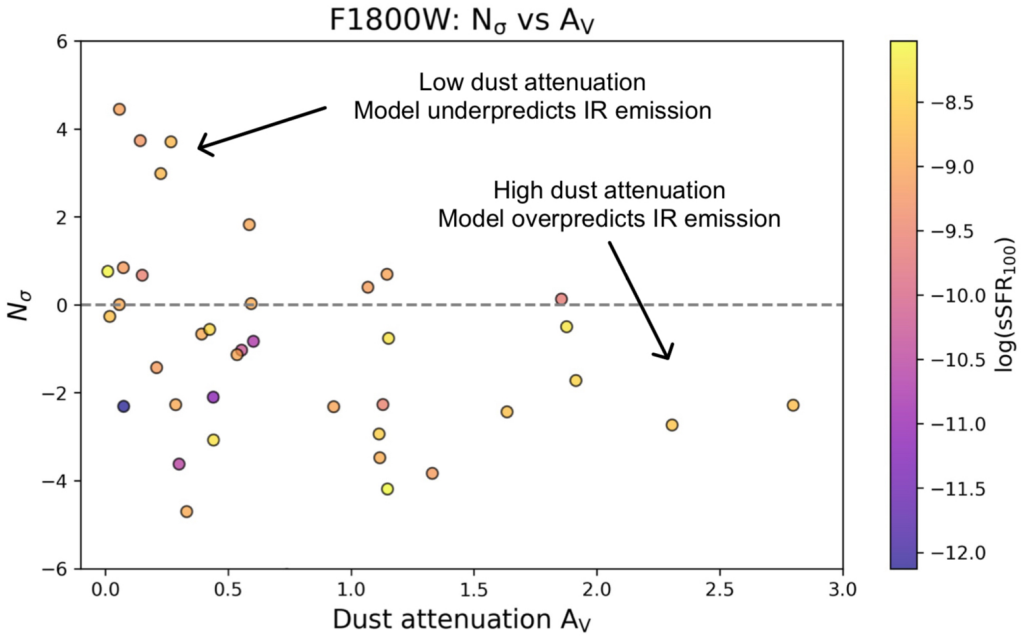

Figure 7.1: N_σ vs. dust attenuation A_V, coloured by sSFR. For dusty galaxies (large A_V), Prospector tends to overpredict the infrared emission, whereas the opposite trend is observed at the low-dust end of the sample.

to the line of sight. Figure 7.2 illustrates a simple *Gedankenexperiment* in which two observers view the same galaxy from different angles. When observing a spiral galaxy edge-on (observer 1), stellar light is heavily absorbed by dust lanes within the spiral arms, and Prospector infers strong dust attenuation. Now, suppose that the galaxy is viewed face-on (observer 2). In this case, stellar light is observed with little absorption as it passes through the thinner disk. However, the infrared emission from heated dust grains is isotropic, so that both observers will measure the same total infrared flux. The key difference lies in the inferred SED shape: if both observers allow the SED fitting code to extrapolate the infrared spectrum from rest-frame optical and UV data under the assumption of dust energy balance, observer 1 will predict a higher far-infrared flux than observer 2. However, the strength of this effect should be investigated further through detailed morphological classifications of the galaxies analysed in this work (see Section 7.3).

We also find no evidence for hidden dust clumps in the ISM of galaxies, as there is no significant bias towards underestimating FIR fluxes. This is a rather surprising result since smaller clumps of dust would be impossible to see in the rest-frame optical and UV due to the strong absorption of stellar light. This absorbed radiation would add to the total infrared luminosity of the galaxy and cause additional dust emission, which was not observed in this work.

Overall, we conclude that the observed bias towards overpredicting infrared fluxes can most likely be traced to Prospector's assumption of dust energy balance, which may not fully capture the complex physical processes underlying the re-processing of stellar light by dust grains.

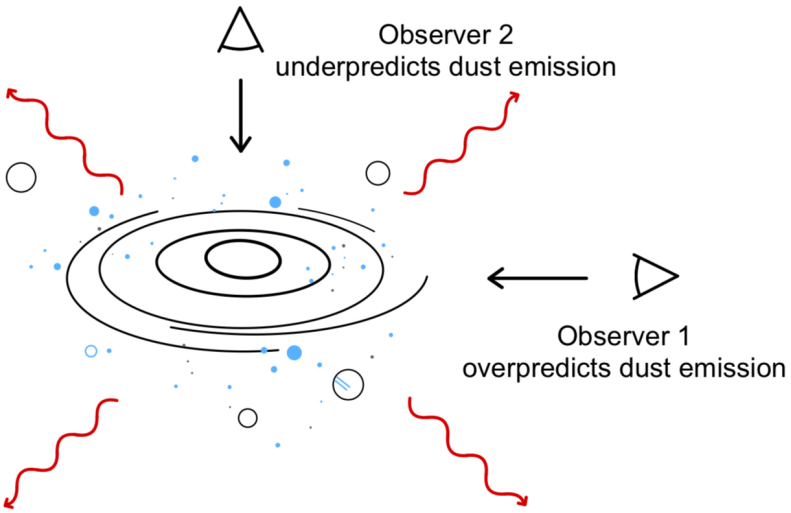

Figure 7.2: Dependence of the predicted dust emission on the line of sight. Observer 1 views the galaxy edge-on and measures a higher dust attenuation than observer 2, who views it from above, thus leading him to predict stronger dust emission. However, the infrared emission is isotropic, meaning that both observers will measure the same infrared flux, regardless of the viewing angle.

7.3 Outlook and Future Projects

Building on the results of this work, we identify two major directions for future studies. A natural next step will be to run new Prospector fits to the multi-band Blue Jay data, including also the MIRI photometry. Including the MIRI data will significantly improve our estimates of dust-obscured star formation and provide tight constraints on dust emission parameters. Ideally, these parameters will be used to update our prior knowledge of the dust absorption and emission properties of galaxies at cosmic noon. Given the much larger field of view of NIRCam compared to MIRI, there are always going to be more NIRCam observations available. Incorporating accurate priors on the shape of the infrared SED is an important step in inferring the complex baryonic processes underlying galaxy formation and evolution in the early universe.

Another important avenue is to investigate the potential impact of disc alignment on the inferred dust emission. This could be explored by examining high-resolution NIRCam imaging across the final galaxy catalogue to study the morphological properties of the sources. Analysing the orientation and structure of galactic discs will allow us to test whether variations in dust emission are correlated with viewing angle or internal geometry. However, this analysis may not be as straightforward as it seems. As discussed in the previous section, the presence of dust lanes along the line of sight can lead to a more complicated geometry than a simple disc - an effect that needs to be carefully accounted for.

Together, these future studies will help advance our understanding of the dust emission properties of galaxies, identify potential observational biases, and pave the way for more physically consistent models of galaxy evolution in the first few billion years of cosmic history.

Bibliography

Albert, L., Lafrenière, D., Doyon, R., Artigau, É., Volk, K., Goudfrooij, P., Martel, A. R., Radica, M., Rowe, J., Espinoza, N., et al. (2023). The near infrared imager and slitless spectrograph for the james webb space telescope. iii. single object slitless spectroscopy. *Publications of the Astronomical Society of the Pacific*, *135*(1049), 075001.

Alberts, S., et al. (2024). Smiles initial data release: Unveiling the obscured universe with miri multi-band imaging [arXiv:2405.15972v1].

Baes, M., Fritz, J., Gadotti, D. A., Smith, D. J., Dunne, L., Da Cunha, E., Amblard, A., Auld, R., Bendo, G. J., Bonfield, D., et al. (2010). Herschel-atlas: The dust energy balance in the edge-on spiral galaxy ugc 4754. *Astronomy & Astrophysics*, *518*, L39.

Belli, S., Park, M., Davies, R. L., Mendel, J. T., Johnson, B. D., Conroy, C., Benton, C., Bugiani, L., Emami, R., Leja, J., et al. (2024). Star formation shut down by multiphase gas outflow in a galaxy at a redshift of 2.45. *Nature*, *630*(8015), 54–58.

Belli, S., Bugiani, L., Park, M., Mendel, J. T., Davies, R. L., Khoram, A. H., Johnson, B. D., Leja, J., Tacchella, S., Brown, V., Conroy, C., Emami, R., Li, Y., Liboni, C., Maheson, G., Mathews, E. P., Naidu, R. P., Nelson, E. J., Terrazas, B. A., & Weinberger, R. (2025). The blue jay survey: Deep jwst spectroscopy for a representative sample of galaxies at cosmic noon. https://arxiv.org/abs/2510.11775

Bianchi, S., Davies, J. I., & Alton, P. B. (2000). Monte carlo predictions of far-infrared emission from spiral galaxies. https://arxiv.org/abs/astro-ph/0005103

Birkmann, S., Ferruit, P., Giardino, G., Nielsen, L., Muñoz, A. G., Kendrew, S., Rauscher, B., Beck, T., Keyes, C., Valenti, J., et al. (2022). The near-infrared spectrograph (nirspec) on the james webb space telescope-iv. capabilities and predicted performance for exoplanet characterization. *Astronomy & Astrophysics*, *661*, A83.

Boccaletti, A., Lagage, P.-O., Baudoz, P., Beichman, C., Bouchet, P., Cavarroc, C., Dubreuil, D., Glasse, A., Glauser, A., Hines, D., et al. (2015). The mid-infrared

instrument for the james webb space telescope, v: Predicted performance of the miri coronagraphs. *Publications of the Astronomical Society of the Pacific*, *127*(953), 633.

Böker, T., Arribas, S., Lützgendorf, N., de Oliveira, C. A., Beck, T., Birkmann, S., Bunker, A., Charlot, S., De Marchi, G., Ferruit, P., et al. (2022). The near-infrared spectrograph (nirspec) on the james webb space telescope-iii. integral-field spectroscopy. *Astronomy & Astrophysics*, *661*, A82.

Böker, T., Beck, T., Birkmann, S., Giardino, G., Keyes, C., Kumari, N., Muzerolle, J., Rawle, T., Zeidler, P., Abul-Huda, Y., et al. (2023). In-orbit performance of the near-infrared spectrograph nirspec on the james webb space telescope. *Publications of the Astronomical Society of the Pacific*, *135*(1045), 038001.

Brammer, G. B., Van Dokkum, P. G., Franx, M., Fumagalli, M., Patel, S., Rix, H.-W., Skelton, R. E., Kriek, M., Nelson, E., Schmidt, K. B., et al. (2012). 3d-hst: A wide-field grism spectroscopic survey with the hubble space telescope. *The Astrophysical Journal Supplement Series*, *200*(2), 13.

Brinchmann, J., Charlot, S., White, S. D., Tremonti, C., Kauffmann, G., Heckman, T., & Brinkmann, J. (2004). The physical properties of star-forming galaxies in the low-redshift universe. *Monthly notices of the royal astronomical society*, *351*(4), 1151–1179.

Bruzual, G. (1983). Subject headings: Galaxies: Evolution–galaxies: Photometry–galaxies: Stellar content–ultraviolet: Spectra–stars: Formation. *The Astrophysical Journal*, *273*, 105–127.

Bruzual, G., & Charlot, S. (2003). Stellar population synthesis at the resolution of 2003. *Monthly Notices of the Royal Astronomical Society*, *344*(4), 1000–1028.

Bugiani, L., Belli, S., Park, M., Davies, R. L., Mendel, J. T., Johnson, B. D., Khoram, A. H., Benton, C., Cimatti, A., Conroy, C., et al. (2025). Active galactic nucleus feedback in quiescent galaxies at cosmic noon traced by ionized gas emission. *The Astrophysical Journal*, *981*(1), 25.

Bundy, K., Ellis, R. S., & Conselice, C. J. (2005). The mass assembly histories of galaxies of various morphologies in the goods fields. *The Astrophysical Journal*, *625*(2), 621.

Bushouse, H., Eisenhamer, J., Dencheva, N., Davies, J., Greenfield, P., Morrison, J., Hodge, P., Simon, B., Grumm, D., Droettboom, M., Slavich, E., Sosey, M., Pauly, T., Miller, T., Jedrzejewski, R., Hack, W., Davis, D., Crawford, S., Law, D., ... Filippazzo, J. (2025, July). *Jwst calibration pipeline* (Version 1.19.1). Zenodo. https://doi.org/10.5281/zenodo.16280965

Calabretta, M. R., & Greisen, E. W. (2002). Representations of celestial coordinates in fits. *Astronomy & Astrophysics*, *395*(3), 1077–1122.

Calzetti, D., Armus, L., Bohlin, R. C., Kinney, A. L., Koornneef, J., & Storchi-Bergmann, T. (2000). The dust content and opacity of activelystar-forming galaxies. *The Astrophysical Journal*, *533*(2), 682.

Cardelli, J. A., Clayton, G. C., & Mathis, J. S. (1989). The relationship between infrared, optical, and ultraviolet extinction. *Astrophysical Journal, Part 1 (ISSN 0004-637X), vol. 345, Oct. 1, 1989, p. 245-256.*, *345*, 245–256.

Carnall, A., McLure, R., Dunlop, J., & Davé, R. (2018). Inferring the star formation histories of massive quiescent galaxies with bagpipes: Evidence for multiple quenching mechanisms. *Monthly Notices of the Royal Astronomical Society*, *480*(4), 4379–4401.

Carnall, A. C., Leja, J., Johnson, B. D., McLure, R. J., Dunlop, J. S., & Conroy, C. (2019). How to measure galaxy star formation histories. i. parametric models. *The Astrophysical Journal*, *873*(1), 44. https://doi.org/10.3847/1538-4357/ab04a2

Casey, C. M., Kartaltepe, J. S., Drakos, N. E., Franco, M., Harish, S., Paquereau, L., Ilbert, O., Rose, C., Cox, I. G., Nightingale, J. W., Robertson, B. E., Silverman, J. D., Koekemoer, A. M., Massey, R., McCracken, H. J., Rhodes, J., Akins, H. B., Allen, N., Amvrosiadis, A., ... Zavala, J. A. (2023). Cosmos-web: An overview of the jwst cosmic origins survey. *The Astrophysical Journal*, *954*(1), 31. https://doi.org/10.3847/1538-4357/acc2bc

Conroy, C. (2013). Modeling the panchromatic spectral energy distributions of galaxies. *Annual Review of Astronomy and Astrophysics*, *51*, 393–455.

Conroy, C., Gunn, J. E., & White, M. (2009). The propagation of uncertainties in stellar population synthesis modeling. i. the relevance of uncertain aspects of stellar evolution and the initial mass function to the derived physical properties of galaxies. *The Astrophysical Journal*, *699*(1), 486.

Conselice, C. J., Blackburne, J. A., & Papovich, C. (2005). The luminosity, stellar mass, and number density evolution of field galaxies of known morphology from z= 0.5 to 3. *The Astrophysical Journal*, *620*(2), 564.

COSMOS-3D Team. (2023). Cosmos-3d: A legacy spectroscopic/imaging survey of the early universe [Unpublished proposal].

Cui, Y., Xiang, Y., Rong, K., Feris, R., & Cao, L. (2014). A spatial-color layout feature for representing galaxy images, 213–219. https://doi.org/10.1109/WACV.2014.6836098

Da Cunha, E., Charlot, S., & Elbaz, D. (2008). A simple model to interpret the ultraviolet, optical and infrared emission from galaxies. *Monthly Notices of the Royal Astronomical Society*, *388*(4), 1595–1617. https://doi.org/10.1111/j.1365-2966.2008.13535.x

Daddi, E., Dickinson, M., Morrison, G., Chary, R., Cimatti, A., Elbaz, D., Frayer, D., Renzini, A., Pope, A., Alexander, D., et al. (2007). Multiwavelength study of massive galaxies at z˜ 2. i. star formation and galaxy growth. *The Astrophysical Journal*, *670*(1), 156.

De Vaucouleurs, G. (1959). Classification and morphology of external galaxies. In *Astrophysik iv: Sternsysteme/astrophysics iv: Stellar systems* (pp. 275–310). Springer.

Delgado-Serrano, R., Hammer, F., Yang, Y., Puech, M., Flores, H., & Rodrigues, M. (2010). How was the hubble sequence 6 gyr ago? *Astronomy & Astrophysics*, *509*, A78.

Dicken, D., Marín, M. G., Shivaei, I., Guillard, P., & Libralato. (2024). Jwst miri flight performance: Imaging. *Astronomy & Astrophysics*, *689*, A5. https://doi.org/10.1051/0004-6361/202449451

Doyon, R., Hutchings, J. B., Beaulieu, M., Albert, L., Lafrenière, D., Willott, C., Touahri, D., Rowlands, N., Maszkiewicz, M., Fullerton, A. W., et al. (2012). The jwst fine guidance sensor (fgs) and near-infrared imager and slitless spectrograph (niriss). *Space telescopes and instrumentation 2012: Optical, infrared, and millimeter wave*, *8442*, 1005–1017.

Doyon, R., Willott, C. J., Hutchings, J. B., Sivaramakrishnan, A., Albert, L., Lafrenière, D., Rowlands, N., Vila, M. B., Martel, A. R., LaMassa, S., et al. (2023). The near infrared imager and slitless spectrograph for the james webb space telescope. i. instrument overview and in-flight performance. *Publications of the Astronomical Society of the Pacific*, *135*(1051), 098001.

Draine, B. T. (2011). *Physics of the interstellar and intergalactic medium* (Vol. 19). Princeton University Press.

Draine, B. (2003). Interstellar dust grains. *Annual Review of Astronomy and Astrophysics*, *41*(Volume 41, 2003), 241–289. https://doi.org/https://doi.org/10.1146/annurev.astro.41.011802.094840

Dunlop, J. S., Abraham, R. G., Ashby, M. L., Bagley, M., Best, P. N., Bongiorno, A., Bouwens, R., Bowler, R. A., Brammer, G., Bremer, M., et al. (2021). Primer: Public release imaging for extragalactic research. *JWST Proposal. Cycle 1*, 1837.

Eldridge, J. J., Stanway, E. R., Xiao, L., McClelland, L. A. S., Taylor, G., Ng, M., Greis, S. M. L., & Bray, J. C. (2017). Binary population and spectral synthesis version

2.1: Construction, observational verification, and new results. *Publications of the Astronomical Society of Australia*, *34*, e058. https://doi.org/10.1017/pasa.2017.51

Ferreira, L., Adams, N., Conselice, C. J., Sazonova, E., Austin, D., Caruana, J., Ferrari, F., Verma, A., Trussler, J., Broadhurst, T., Diego, J., Frye, B. L., Pascale, M., Wilkins, S. M., Windhorst, R. A., & Zitrin, A. (2022). Panic! at the disks: First rest-frame optical observations of galaxy structure at z gt; 3 with jwst in the smacs 0723 field. *The Astrophysical Journal Letters*, *938*(1), L2. https://doi.org/10.3847/2041-8213/ac947c

Ferruit, P., Jakobsen, P., Giardino, G., Rawle, T., de Oliveira, C. A., Arribas, S., Beck, T., Birkmann, S., Böker, T., Bunker, A., et al. (2022). The near-infrared spectrograph (nirspec) on the james webb space telescope-ii. multi-object spectroscopy (mos). *Astronomy & Astrophysics*, *661*, A81.

Foreman-Mackey, D., Hogg, D. W., Lang, D., & Goodman, J. (2013). Emcee: The mcmc hammer. *Publications of the Astronomical Society of the Pacific*, *125*(925), 306.

Gallagher III, J. S., Hunter, D. A., & Tutukov, A. V. (1984). Star formation histories of irregular galaxies. *Astrophysical Journal, Part 1 (ISSN 0004-637X), vol. 284, Sept. 15, 1984, p. 544-556.*, *284*, 544–556.

Gardner, J. P. (2005). Science with the james webb space telescope. *Proceedings of the International Astronomical Union*, *1*(S232), 87–98. https://doi.org/10.1017/S1743921306000317

Gardner, J. P., Mather, J. C., Clampin, M., Doyon, R., Greenhouse, M. A., Hammel, H. B., Hutchings, J. B., Jakobsen, P., Lilly, S. J., Long, K. S., Lunine, J. I., Mccaughrean, M. J., Mountain, M., Nella, J., Rieke, G. H., Rieke, M. J., Rix, H.-W., Smith, E. P., Sonneborn, G., ... Wright, G. S. (2006). The james webb space telescope. *Space Science Reviews*, *123*(4), 485–606. https://doi.org/10.1007/s11214-006-8315-7

Gardner, J. P., Mather, J. C., Abbott, R., Abell, J. S., Abernathy, M., Abney, F. E., Abraham, J. G., Abraham, R., Abul-Huda, Y. M., Acton, S., et al. (2023). The james webb space telescope mission. *Publications of the Astronomical Society of the Pacific*, *135*(1048), 068001. https://doi.org/10.1088/1538-3873/acd1b5

Glasse, A., Rieke, G., Bauwens, E., García-Marín, M., Ressler, M., Rost, S., Tikkanen, T. V., Vandenbussche, B., & Wright, G. (2015). The mid-infrared instrument for the james webb space telescope, ix: Predicted sensitivity. *Publications of the Astronomical Society of the Pacific*, *127*(953), 686.

Goodman, J., & Weare, J. (2010). Ensemble samplers with affine invariance. *Communications in applied mathematics and computational science*, *5*(1), 65–80.

Gordon, K. D., Misselt, K., Witt, A. N., & Clayton, G. C. (2001). The dirty model. i. monte carlo radiative transfer throughdust. *The Astrophysical Journal*, *551*(1), 269.

Greenfield, P., & Miller, T. (2016). The calibration reference data system. *Astronomy and Computing*, *16*, 41–53. https://doi.org/https://doi.org/10.1016/j.ascom.2016.04.001

Greisen, E. W., & Calabretta, M. R. (2002). Representations of world coordinates in FITS., *395*, 1061–1075. https://doi.org/10.1051/0004-6361:20021326

Grogin, N. A., Kocevski, D. D., Faber, S. M., Ferguson, H. C., Koekemoer, A. M., Riess, A. G., Acquaviva, V., Alexander, D. M., Almaini, O., Ashby, M. L. N., Barden, M., Bell, E. F., Bournaud, F., Brown, T. M., Caputi, K. I., Casertano, S., Cassata, P., Castellano, M., Challis, P., ... Yun, M. S. (2011). Candels: The cosmic assembly near-infrared deep extragalactic legacy survey. *The Astrophysical Journal Supplement Series*, *197*(2), 35. https://doi.org/10.1088/0067-0049/197/2/35

Harish, S., Kartaltepe, J. S., Liu, D., Koekemoer, A. M., Casey, C. M., Franco, M., Akins, H. B., Ilbert, O., Shuntov, M., Drakos, N. E., Engesser, M., Faisst, A. L., Gozaliasl, G., Martin, C. L., Hirschmann, M., Kokorev, V., Lambrides, E., McCracken, H. J., McKinney, J., ... Robertson, B. E. (2025). Cosmos-web: Miri data reduction and number counts at 7.7μm using jwst. https://arxiv.org/abs/2506.03306

Hauser, M. G., & Dwek, E. (2001). The cosmic infrared background: Measurements and implications. *Annual Review of Astronomy and Astrophysics*, *39*(1), 249–307.

Holmberg, E. (1958). A photographic photometry of extragalactic nebulae. *Meddelanden fran Lunds Astronomiska Observatorium Serie II*, *136*, 1.

Hora, J. L., Fazio, G. G., Allen, L. E., Ashby, M. L., Barmby, P., Deutsch, L. K., Huang, J. S., Marengo, M., Megeath, S. T., Melnick, G. J., et al. (2004). In-flight performance and calibration of the infrared array camera (irac) for the spitzer space telescope. *Optical, Infrared, and Millimeter Space Telescopes*, *5487*, 77–92.

Horner, S. D., & Rieke, M. J. (2004). The near-infrared camera (nircam) for the james webb space telescope (jwst). *Optical, infrared, and millimeter space telescopes*, *5487*, 628–634.

Hubble, E. (1927). The classification of spiral nebulae. *The Observatory, Vol. 50, p. 276-281 (1927)*, *50*, 276–281.

Jakobsen, P., Ferruit, P., de Oliveira, C. A., Arribas, S., Bagnasco, G., Barho, R., Beck, T., Birkmann, S., Böker, T., Bunker, A., et al. (2022). The near-infrared

spectrograph (nirspec) on the james webb space telescope-i. overview of the instrument and its capabilities. *Astronomy & Astrophysics*, *661*, A80.

Johnson, B. D., Leja, J., Conroy, C., & Speagle, J. S. (2021). Stellar population inference with prospector. *The Astrophysical Journal Supplement Series*, *254*(2), 22.

Kendrew, S., Scheithauer, S., Bouchet, P., Amiaux, J., Azzollini, R., Bouwman, J., Chen, C., Dubreuil, D., Fischer, S., Glasse, A., et al. (2015). The mid-infrared instrument for the james webb space telescope, iv: The low-resolution spectrometer. *Publications of the Astronomical Society of the Pacific*, *127*(953), 623.

Kennicutt Jr, R. C. (1998). Star formation in galaxies along the hubble sequence. *Annual Review of Astronomy and Astrophysics*, *36*(1), 189–231.

Koekemoer, A. M., Faber, S. M., Ferguson, H. C., Grogin, N. A., Kocevski, D. D., & Koo. (2011). Candels: The cosmic assembly near-infrared deep extragalactic legacy survey—the hubble space telescope observations, imaging data products, and mosaics. *The Astrophysical Journal Supplement Series*, *197*(2), 36. https://doi.org/10.1088/0067-0049/197/2/36

Kriek, M., & Conroy, C. (2013). The dust attenuation law in distant galaxies: Evidence for variation with spectral type. *The Astrophysical Journal Letters*, *775*(1), L16.

Leja, J., Carnall, A. C., Johnson, B. D., Conroy, C., & Speagle, J. S. (2019). How to Measure Galaxy Star Formation Histories. II. Nonparametric Models., *876*(1), Article 3, 3. https://doi.org/10.3847/1538-4357/ab133c

Leja, J., Johnson, B. D., Conroy, C., Dokkum, P. G. v., & Byler, N. (2017). Deriving physical properties from broadband photometry with prospector: Description of the model and a demonstration of its accuracy using 129 galaxies in the local universe. *The Astrophysical Journal*, *837*(2), 170. https://doi.org/10.3847/1538-4357/aa5ffe

Leja, J., Speagle, J. S., Ting, Y.-S., Johnson, B. D., Conroy, C., Whitaker, K. E., Nelson, E. J., Van Dokkum, P., & Franx, M. (2022). A new census of the $0.2 < z < 3.0$ universe. ii. the star-forming sequence. *The Astrophysical Journal*, *936*(2), 165.

Madau, P., & Dickinson, M. (2014). Cosmic star-formation history. *Annual Review of Astronomy and Astrophysics*, *52*(1), 415–486.

Mcdermid, R., Cresci, G., Rigaut, F., Bouret, J.-C., Silva, G., Gullieuszik, M., Magrini, L., Mendel, J., Antoniucci, S., Bono, G., Kamath, D., Monty, S., Baumgardt, H., Cortese, L., Fisher, D., Mannucci, F., Migliorini, A., Sweet, S., Vanzella, E., & Papers, w. (2020, September). *Phase a science case for mavis – the multi-*

conjugate adaptive-optics visible imager-spectrograph for the vlt adaptive optics facility. https://doi.org/10.48550/arXiv.2009.09242

Momcheva, I. G., Brammer, G. B., Van Dokkum, P. G., Skelton, R. E., Whitaker, K. E., Nelson, E. J., Fumagalli, M., Maseda, M. V., Leja, J., Franx, M., et al. (2016). The 3d-hst survey: Hubble space telescope wfc3/g141 grism spectra, redshifts, and emission line measurements for 100,000 galaxies. *The Astrophysical Journal Supplement Series*, *225*(2), 27.

Moresco, M., Pozzetti, L., Cimatti, A., Zamorani, G., Bolzonella, M., Lamareille, F., Mignoli, M., Zucca, E., Lilly, S., Carollo, C. M., et al. (2013). Spot the difference-impact of different selection criteria on observed properties of passive galaxies in zcosmos-20k sample. *Astronomy & Astrophysics*, *558*, A61.

Mortlock, A., Conselice, C. J., Bluck, A. F., Bauer, A. E., Grützbauch, R., Buitrago, F., & Ownsworth, J. (2011). A deep probe of the galaxy stellar mass functions at z 1–3 with the goods nicmos survey. *Monthly Notices of the Royal Astronomical Society*, *413*(4), 2845–2859.

Mortlock, A., Conselice, C. J., Hartley, W. G., Ownsworth, J. R., Lani, C., Bluck, A. F. L., Almaini, O., Duncan, K., Wel, A. v. d., Koekemoer, A. M., Dekel, A., Davé, R., Ferguson, H. C., de Mello, D. F., Newman, J. A., Faber, S. M., Grogin, N. A., Kocevski, D. D., & Lai, K. (2013). The redshift and mass dependence on the formation of the hubble sequence at z > 1 from candels/uds. *Monthly Notices of the Royal Astronomical Society*, *433*(2), 1185–1201. https://doi.org/10.1093/mnras/stt793

Noeske, K., Weiner, B., Faber, S., Papovich, C., Koo, D., Somerville, R., Bundy, K., Conselice, C., Newman, J., Schiminovich, D., et al. (2007). Star formation in aegis field galaxies since z= 1.1: The dominance of gradually declining star formation, and the main sequence of star-forming galaxies. *The Astrophysical Journal*, *660*(1), L43.

Pacifici, C., Kassin, S. A., Weiner, B., Charlot, S., & Gardner, J. P. (2012). The rise and fall of the star formation histories of blue galaxies at redshifts 0.2< z< 1.4. *The Astrophysical Journal Letters*, *762*(1), L15.

Papovich, C., Dickinson, M., & Ferguson, H. C. (2001). The stellar populations and evolution of lyman breakgalaxies. *The Astrophysical Journal*, *559*(2), 620.

Park, M., Belli, S., Conroy, C., Johnson, B. D., Davies, R. L., Leja, J., Tacchella, S., Mendel, J., Benton, C., Bugiani, L., Emami, R., Khoram, A. H., Li, Y., Maheson, G., Mathews, E. P., Naidu, R. P., Nelson, E. J., Terrazas, B. A., & Weinberger, R. (2024). Widespread rapid quenching at cosmic noon revealed by jwst deep spectroscopy. *The Astrophysical Journal*, *976*(1), 72. https://doi.org/10.3847/1538-4357/ad7e15

Pence, W. D., Chiappetti, L., Page, C. G., Shaw, R. A., & Stobie, E. (2010). Definition of the flexible image transport system (fits), version 3.0. *Astronomy & Astrophysics*, *524*, A42.

Perrin, M. D., Soummer, R., Elliott, E. M., Lallo, M. D., & Sivaramakrishnan, A. (2012). Simulating point spread functions for the james webb space telescope with webbpsf. *Space telescopes and instrumentation 2012: optical, infrared, and millimeter wave*, *8442*, 1193–1203.

Popescu, C. C., & Tuffs, R. J. (2002). The percentage of stellar light re-radiated by dust in late-type virgo cluster galaxies. *Monthly Notices of the Royal Astronomical Society*, *335*(2), L41–L44.

Ravindranath, S., Ferguson, H., Conselice, C., Giavalisco, M., Dickinson, M., Chatzichristou, E., De Mello, D., Fall, S., Gardner, J., Grogin, N., et al. (2004). The evolution of disk galaxies in the goods-south field: Number densities and size distribution. *The Astrophysical Journal*, *604*(1), L9.

Ressler, M. E., Sukhatme, K. G., Franklin, B. R., Mahoney, J. C., Thelen, M. P., Bouchet, P., Colbert, J. W., Cracraft, M., Dicken, D., Gastaud, R., Goodson, G. B., Eccleston, P., Moreau, V., Rieke, G. H., & Schneider, A. (2015). The mid-infrared instrument for the james webb space telescope, viii: The miri focal plane system. *Publications of the Astronomical Society of the Pacific*, *127*(953), 675. https://doi.org/10.1086/682258

Rieke, G. H., Wright, G., Böker, T., Bouwman, J., Colina, L., Glasse, A., Gordon, K., Greene, T., Güdel, M., Henning, T., et al. (2015). The mid-infrared instrument for the james webb space telescope, i: Introduction. *Publications of the Astronomical Society of the Pacific*, *127*(953), 584.

Rieke, M. J., Baum, S. A., Beichman, C. A., Crampton, D., Doyon, R., Eisenstein, D., Greene, T. P., Hodapp, K.-W., Horner, S. D., Johnstone, D., et al. (2003). Ngst nircam scientific program and design concept. *IR space telescopes and instruments*, *4850*, 478–485.

Rieke, M. J., Kelly, D. M., Misselt, K., Stansberry, J., Boyer, M., Beatty, T., Egami, E., Florian, M., Greene, T. P., Hainline, K., et al. (2023). Performance of nircam on jwst in flight. *Publications of the Astronomical Society of the Pacific*, *135*(1044), 028001.

Rigby, J., Perrin, M., McElwain, M., Kimble, R., Friedman, S., Lallo, M., Doyon, R., Feinberg, L., Ferruit, P., Glasse, A., Rieke, M., Rieke, G., Wright, G., Willott, C., & Colon. (2023). The science performance of jwst as characterized in commissioning. *Publications of the Astronomical Society of the Pacific*, *135*(1046), 048001. https://doi.org/10.1088/1538-3873/acb293

Rowan-Robinson, M. (1980). Radiative transfer in dust clouds. i-hot-centered clouds associated with regions of massive star formation. *Astrophysical Journal Supplement Series, vol. 44, Nov. 1980, p. 403-426. Science Research Council*, *44*, 403–426.

Rowlands, N., Hutchings, J., Murowinski, R. G., & Alexander, R. (2003). Ngst fine guidance sensor. *IR Space Telescopes and Instruments*, *4850*, 574–585.

Rowlands, N., Evans, C., Greenberg, E., Gregory, P., Scott, A., Thibault, S., Poirier, M., Doyon, R., Hutchings, J. B., & Alexander, R. (2004). Tunable filters for jwst fine guidance sensor. *Optical, Infrared, and Millimeter Space Telescopes*, *5487*, 676–687.

Saftly, W., Baes, M., De Geyter, G., Camps, P., Renaud, F., Guedes, J., & De Looze, I. (2015). Large and small-scale structures and the dust energy balance problem in spiral galaxies. *Astronomy & Astrophysics*, *576*, A31.

Salim, S., Rich, R. M., Charlot, S., Brinchmann, J., Johnson, B. D., Schiminovich, D., Seibert, M., Mallery, R., Heckman, T. M., Forster, K., et al. (2007). Uv star formation rates in the local universe. *The Astrophysical Journal Supplement Series*, *173*(2), 267.

Shapley, A. E. (2011). Physical properties of galaxies from z= 2–4. *Annual Review of Astronomy and Astrophysics*, *49*(1), 525–580.

Shuntov, M., Akins, H. B., Paquereau, L., Casey, C. M., Ilbert, O., Arango-Toro, R. C., McCracken, H. J., Franco, M., Harish, S., Kartaltepe, J. S., Koekemoer, A. M., Yang, L., Huertas-Company, M., Berman, E. M., McCleary, J. E., Toft, S., Gavazzi, R., Achenbach, M. J., Bertin, E., ... Yang, J. (2025). Cosmos2025: The cosmos-web galaxy catalog of photometry, morphology, redshifts, and physical parameters from jwst, hst, and ground-based imaging. https://arxiv.org/abs/2506.03243

Silva, L., Granato, G. L., Bressan, A., & Danese, L. (1998). Modeling the effects of dust on galactic spectral energy distributions from the ultraviolet to the millimeter band. *The Astrophysical Journal*, *509*(1), 103.

Simha, V., Weinberg, D. H., Conroy, C., Dave, R., Fardal, M., Katz, N., & Oppenheimer, B. D. (2014). Parametrising star formation histories. *arXiv preprint arXiv:1404.0402*.

Sivaramakrishnan, A., Lafrenière, D., Ford, K. S., McKernan, B., Cheetham, A., Greenbaum, A. Z., Tuthill, P. G., Lloyd, J. P., Ireland, M. J., Doyon, R., et al. (2012). Non-redundant aperture masking interferometry (ami) and segment phasing with jwst-niriss. *Space Telescopes and Instrumentation 2012: Optical, Infrared, and Millimeter Wave*, *8442*, 1018–1031.

Sivaramakrishnan, A., Tuthill, P., Lloyd, J. P., Greenbaum, A. Z., Thatte, D., Cooper, R. A., Vandal, T., Kammerer, J., Sanchez-Bermudez, J., Pope, B. J., et al. (2023). The near infrared imager and slitless spectrograph for the james webb space telescope. iv. aperture masking interferometry. *Publications of the Astronomical Society of the Pacific*, *135*(1043), 015003.

Skelton, R. E., Whitaker, K. E., Momcheva, I. G., Brammer, G. B., Van Dokkum, P. G., Labbé, I., Franx, M., Van Der Wel, A., Bezanson, R., Da Cunha, E., et al. (2014). 3d-hst wfc3-selected photometric catalogs in the five candels/3d-hst fields: Photometry, photometric redshifts, and stellar masses. *The Astrophysical Journal Supplement Series*, *214*(2), 24.

Skibba, R. A., Engelbracht, C. W., Dale, D., Hinz, J., Zibetti, S., Crocker, A., Groves, B., Hunt, L., Johnson, B. D., Meidt, S., Murphy, E., Appleton, P., Armus, L., Bolatto, A., Brandl, B., Calzetti, D., Croxall, K., Galametz, M., Gordon, K. D., ... Wolfire, M. (2011). The emission by dust and stars of nearby galaxies in the herschel kingfish survey. *The Astrophysical Journal*, *738*(1), 89. https://doi.org/10.1088/0004-637X/738/1/89

Skilling, J. (2004). Nested sampling. *Bayesian inference and maximum entropy methods in science and engineering*, *735*, 395–405.

Soifer, B., & Neugebauer, G. (1991). The properties of infrared galaxies in the local universe. *Astronomical Journal (ISSN 0004-6256), vol. 101, Feb. 1991, p. 354-361. Research supported by NASA.*, *101*, 354–361.

Speagle, J. S., Steinhardt, C. L., Capak, P. L., & Silverman, J. D. (2014). A highly consistent framework for the evolution of the star-forming "main sequence" from z 0–6. *The Astrophysical Journal Supplement Series*, *214*(2), 15. https://doi.org/10.1088/0067-0049/214/2/15

Speagle, J. S. (2020). Dynesty: A dynamic nested sampling package for estimating bayesian posteriors and evidences. *Monthly Notices of the Royal Astronomical Society*, *493*(3), 3132–3158.

Thompson, W. (2006). Coordinate systems for solar image data. *Astronomy & Astrophysics*, *449*(2), 791–803.

Tinsley, B. M. (1980). *Evolution of the stars and gas in galaxies*. Gordon; Breach Science Publishers.

Trumpler, R. J. (1930). Absorption of light in the galactic system. *Publications of the Astronomical Society of the Pacific*, *42*(248), 214–227. Retrieved September 27, 2025, from http://www.jstor.org/stable/40668744

Van Den Bergh, S., Abraham, R. G., Ellis, R. S., Tanvir, N. R., Santiago, B. X., & Glazebrook, K. G. (1996). A morphological catalog of galaxies in the hubble deep field. *Astronomical Journal v. 112, p. 359*, *112*, 359.

Viaene, S., Baes, M., Bendo, G., Boquien, M., Boselli, A., Ciesla, L., Cortese, L., De Looze, I., Eales, S., Fritz, J., et al. (2016). The bolometric and uv attenuation in normal spiral galaxies of the herschel reference survey. *Astronomy & Astrophysics*, *586*, A13.

Walcher, J., Groves, B., Budavári, T., & Dale, D. (2011). Fitting the integrated spectral energy distributions of galaxies. *Astrophysics and Space Science*, *331*(1), 1–51.

Weaver, J., Zalesky, L., Kokorev, V., McPartland, C., Chartab, N., Gould, K., Shuntov, M., Davidzon, I., Faisst, A., Stickley, N., et al. (2023). The farmer: A reproducible profile-fitting photometry package for deep galaxy surveys. *The Astrophysical Journal Supplement Series*, *269*(1), 20.

Weigel, A. K., Schawinski, K., & Bruderer, C. (2016). Stellar mass functions: Methods, systematics and results for the local universe. *Monthly Notices of the Royal Astronomical Society*, *459*(2), 2150–2187.

Wells, D. C., & Greisen, E. W. (1979). Fits-a flexible image transport system. *Image processing in astronomy*, 445.

Wells, M., Pel, J.-W., Glasse, A., Wright, G., Aitink-Kroes, G., Azzollini, R., Beard, S., Brandl, B., Gallie, A., Geers, V., et al. (2015). The mid-infrared instrument for the james webb space telescope, vi: The medium resolution spectrometer. *Publications of the Astronomical Society of the Pacific*, *127*(953), 646.

Willott, C. J., Doyon, R., Albert, L., Brammer, G. B., Dixon, W. V., Muzic, K., Ravindranath, S., Scholz, A., Abraham, R., Artigau, É., et al. (2022). The near-infrared imager and slitless spectrograph for the james webb space telescope. ii. wide field slitless spectroscopy. *Publications of the Astronomical Society of the Pacific*, *134*(1032), 025002.

Witt, A. N., & Gordon, K. D. (2000). Multiple scattering in clumpy media. ii. galactic environments. *The Astrophysical Journal*, *528*(2), 799.

Wright, E. L., Eisenhardt, P. R., Mainzer, A. K., Ressler, M. E., Cutri, R. M., Jarrett, T., Kirkpatrick, J. D., Padgett, D., McMillan, R. S., Skrutskie, M., et al. (2010). The wide-field infrared survey explorer (wise): Mission description and initial on-orbit performance. *The Astronomical Journal*, *140*(6), 1868.

Wright, G. S., Wright, D., Goodson, G., Rieke, G. H., Aitink-Kroes, G., Amiaux, J., Aricha-Yanguas, A., Azzollini, R., Banks, K., Barrado-Navascues, D., et al. (2015). The mid-infrared instrument for the james webb space telescope, ii: De-

sign and build. *Publications of the Astronomical Society of the Pacific*, *127*(953), 595.

Wright, G. S., Rieke, G. H., Glasse, A., Ressler, M., García Marín, M., Aguilar, J., & Alberts. (2023). The mid-infrared instrument for jwst and its in-flight performance. *Publications of the Astronomical Society of the Pacific*, *135*(1046), 048003. https://doi.org/10.1088/1538-3873/acbe66

York, D. G., Adelman, J., Anderson Jr, J. E., Anderson, S. F., Annis, J., Bahcall, N. A., Bakken, J., Barkhouser, R., Bastian, S., Berman, E., et al. (2000). The sloan digital sky survey: Technical summary. *The Astronomical Journal*, *120*(3), 1579.

List of Figures

List of Tables

Appendix A

Description of the Photometric Catalogue

This appendix provides a description of the individual columns and their data types stored in the final photometric table, resulting from the photometric pipeline discussed in Chapter 4. In general, the catalogue is structured in columns containing scalar or array values; Table 4.3 lists each column with its name, data type, units, and a brief description.

Array Columns

Array-type columns store measurements for the MIRI filters analysed in this work, following the ordering:

[F770W, F1000W, F1800W, F2100W]

Each array entry contains between one and four values, depending on the number of available measurements. For arrays with fewer than four values, the corresponding filters can be identified via the "`Filters`" column (see below).

- `Flux` : ndarray (float)
  Background-subtracted aperture fluxes in units of μJy.
- `Flux_Err` : ndarray (float)
  Total photometric uncertainties, computed according to Equation (4.4).
- `Image_Err` : ndarray (float)
  Pixel-level background noise within the aperture, estimated from the error image according to Equation (4.3).
- `Flux_BKG` : ndarray (float)
  Local background flux values measured within the aperture.
- `Flux_BKG_Err` : ndarray (float)
  Uncertainties associated with the background flux estimates, as calculated by Equation (4.2).

- `AB_Mag` : ndarray (float)
  Aperture fluxes converted into AB magnitudes.
- `Apr_Corr` : ndarray (float)
  Aperture correction factors applied to account for flux falling outside the defined aperture.
- `Apr_Xcenter` : ndarray (float)
  x-coordinates of the aperture centre in pixel units.
- `Apr_Ycenter` : ndarray (float)
  y-coordinates of the aperture centre in pixel units.
- `Apr_Theta` : ndarray (float)
  Position angle of the elliptical aperture in degrees, measured counterclockwise from the x-axis.
- `Flag_Art` : ndarray (bool)
  Artefact flag; `True` indicates possible contamination from image artefacts. Defaults to `False`.

Scalar Columns

In contrast to array columns, scalar columns store a single value per galaxy. These values correspond to quantities that are independent of the respective band, such as the unique galaxy ID, aperture size, or the presence of a companion.

- `ID` : int
  The unique 3D-HST galaxy identifier.
- `Apr_A` : float
  Semi-major axis of the elliptical aperture in MIRI pixels.
- `Apr_B` : float
  Semi-minor axis of the elliptical aperture in MIRI pixels.
- `N_PIX` : float
  Number of MIRI pixels within the elliptical aperture.
- `Flag_Com` : bool
  Companion flag; `True` indicates that a companion is visible in at least one band. Defaults to `False`.

Other

The `"Filters"` column represents a special case in the catalogue. Although it is classified as a scalar column, it contains a string listing all bands in which a galaxy was observed. This entry should always be referenced when extracting photometric data from the catalogue to ensure the correct mapping between fluxes and their respective bands.

- `Filters` : string
  Comma-separated string listing the filters in which the galaxy was observed (e.g., "F770W,F1800W"). Always a subset of the ordered list [F770W, F1000W, F1800W, F2100W]. The number of filters corresponds to the length of the array entries in the flux columns.

Appendix B

Unreliable PROSPECTOR Fits

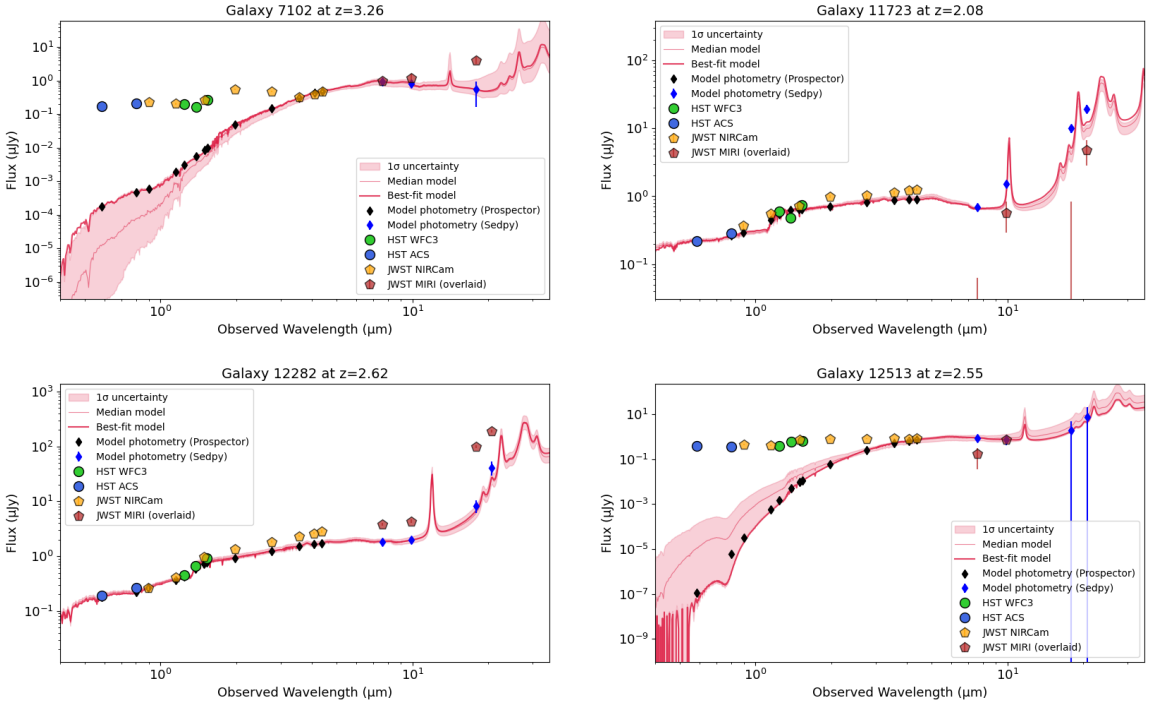

Figure B.1: PROSPECTOR fits excluded from the fit quality analysis discussed in Chapter 6 due to inconsistencies with the observed photometry in the rest-frame optical/UV.

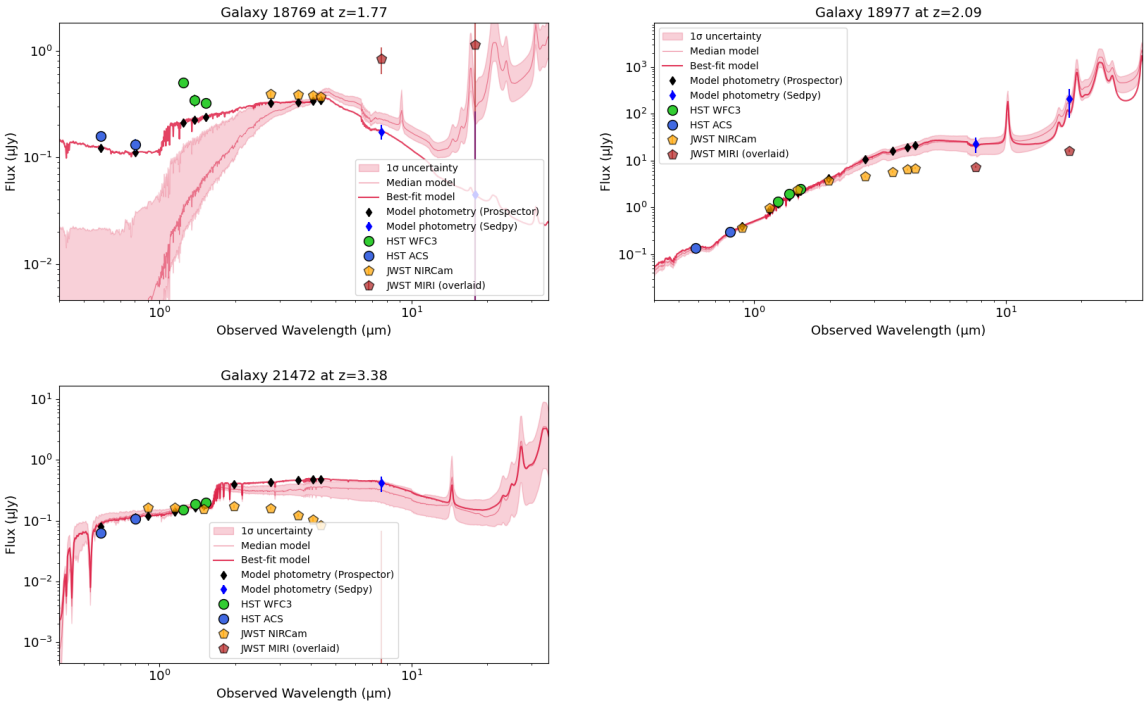

Figure B.2: Continuation of Figure B.1.

Appendix C

Declaration of Usage of Generative Artificial Intelligence

In writing this thesis, I used generative artificial intelligence models such as ChatGPT-4.5 (released in February 2025) and Claude 4 (released in May 2025), as well as newer versions of the same models. These tools were primarily used between March 2025 and September 2025 to support specific aspects of this work, but were never given any creative authorship.

ChatGPT was primarily used for debugging individual code sections and streamlining the logic in the photometric workflow by drawing my attention to existing Python functions and guiding me through the implementation process. It proved especially useful in the creation of large summary statistics and in choosing the right layout to store interim data for further downstream analysis, allowing me to load previous results without re-running the entire script whenever a parameter changed. ChatGPT was also used to improve the flow of specific sections of written text and provided suggestions on the general structure of individual chapters and sections.

Claude was used exclusively for visualisation purposes and for the most detailed refinements of the photometric analysis code, ensuring consistency with other parts of the pipeline. In particular, the layouts of Figure 5.3 or Table 4.2 are owed in part to Claude's suggested improvements.